NAVAL POSTGRADUATE SCHOOL

MONTEREY, CALIFORNIA

THESIS

THERMODYNAMIC AND KINEMATIC FLOW
CHARACTERISTICS OF SOME DEVELOPING AND
NON-DEVELOPING DISTURBANCES IN PREDICT

by

William A. Sauer II

December 2014

Thesis Advisor: Michael T. Montgomery
Second Reader: Qing Wang

Approved for public release; distribution is unlimited

THIS PAGE INTENTIONALLY LEFT BLANK

REPORT DOCUMENTATION PAGE		Form Approved OMB No. 0704–0188

1. AGENCY USE ONLY *(Leave blank)*	2. REPORT DATE December 2014	3. REPORT TYPE AND DATES COVERED Master's Thesis

4. TITLE AND SUBTITLE THERMODYNAMIC AND KINEMATIC FLOW CHARACTERISTICS OF SOME DEVELOPING AND NON-DEVELOPING DISTURBANCES IN PREDICT	5. FUNDING NUMBERS
6. AUTHOR(S) William A. Sauer II	

7. PERFORMING ORGANIZATION NAME(S) AND ADDRESS(ES) Naval Postgraduate School Monterey, CA 93943-5000	8. PERFORMING ORGANIZATION REPORT NUMBER

9. SPONSORING /MONITORING AGENCY NAME(S) AND ADDRESS(ES) N/A	10. SPONSORING/MONITORING AGENCY REPORT NUMBER

11. SUPPLEMENTARY NOTES The views expressed in this thesis are those of the author and do not reflect the official policy or position of the Department of Defense or the U.S. Government. IRB Protocol number ____N/A____.

12a. DISTRIBUTION / AVAILABILITY STATEMENT Approved for public release; distribution is unlimited	12b. DISTRIBUTION CODE A

13. ABSTRACT (maximum 200 words)

The development of tropical disturbances into tropical cyclones is not well understood. The lack of data on developing and non-developing tropical disturbances makes theoretical models difficult to test empirically. This thesis will investigate thermodynamic parameters and kinematic flow structures found in three tropical disturbances investigated in the Pre-Depression Investigation of Cloud-Systems in the Tropics (PREDICT) Experiment. Two of the tropical disturbances did not develop into tropical storms, and one of the tropical disturbances was immediately classified as a tropical storm after the first research flight was conducted on the system.

The presence of significant convective available potential energy (CAPE) and low convective inhibition (CIN) has been universally found in the vicinity of the tropical disturbances studied in this thesis and other recent PREDICT studies, such as "Observations of the Convective Environment in Developing and Non-Developing Tropical Disturbances" by Roger K. Smith and Michael T. Montgomery published in 2012 by the Quarterly Journal of the Royal Meteorological Society. The main difference between developing and non-developing tropical disturbances appears to lie with the kinematic flow boundary structure and thermodynamic properties hypothesized in the marsupial paradigm.

14. SUBJECT TERMS tropical cyclones, marsupial paradigm	15. NUMBER OF PAGES 141
	16. PRICE CODE

17. SECURITY CLASSIFICATION OF REPORT Unclassified	18. SECURITY CLASSIFICATION OF THIS PAGE Unclassified	19. SECURITY CLASSIFICATION OF ABSTRACT Unclassified	20. LIMITATION OF ABSTRACT UU

NSN 7540–01-280-5500

Standard Form 298 (Rev. 2–89)
Prescribed by ANSI Std. 239–18

THIS PAGE INTENTIONALLY LEFT BLANK

THERMODYNAMIC AND KINEMATIC FLOW CHARACTERISTICS OF SOME DEVELOPING AND NON-DEVELOPING DISTURBANCES IN PREDICT

William A. Sauer II
Lieutenant, United States Navy
B.S., Rochester Institute of Technology, 2005

Submitted in partial fulfillment of the
requirements for the degree of

MASTER OF SCIENCE IN METEOROLOGY AND PHYSICAL OCEANOGRAPHY

from the

**NAVAL POSTGRADUATE SCHOOL
December 2014**

Author: William A. Sauer II

Approved by: Michael T. Montgomery
               Thesis Advisor

               Qing Wang
               Second Reader

               Professor Wendell Nuss
               Chair, Department of Meteorology

THIS PAGE INTENTIONALLY LEFT BLANK

ABSTRACT

The development of tropical disturbances into tropical cyclones is not well understood. The lack of data on developing and non-developing tropical disturbances makes theoretical models difficult to test empirically. This thesis will investigate thermodynamic parameters and kinematic flow structures found in three tropical disturbances investigated in the Pre-Depression Investigation of Cloud-Systems in the Tropics (PREDICT) Experiment. Two of the tropical disturbances did not develop into tropical storms, and one of the tropical disturbances was immediately classified as a tropical storm after the first research flight was conducted on the system.

The presence of significant convective available potential energy (CAPE) and low convective inhibition (CIN) has been universally found in the vicinity of the tropical disturbances studied in this thesis and other recent PREDICT studies, such as "Observations of the Convective Environment in Developing and Non-Developing Tropical Disturbances" by Roger K. Smith and Michael T. Montgomery published in 2012 by the *Quarterly Journal of the Royal Meteorological Society*. The main difference between developing and non-developing tropical disturbances appears to lie with the kinematic flow boundary structure and thermodynamic properties hypothesized in the marsupial paradigm.

THIS PAGE INTENTIONALLY LEFT BLANK

TABLE OF CONTENTS

THIS PAGE INTENTIONALLY LEFT BLANK

LIST OF FIGURES

x

xiv

LIST OF TABLES

THIS PAGE INTENTIONALLY LEFT BLANK

LIST OF ACRONYMS AND ABBREVIATIONS

CAPE	convective available potential energy
CIN	convective inhibition
CL	critical latitude
DOD	Department of Defense
ECMWF	European Centre for Medium Range Weather Forecasts
GFS	Global Forecast System
GRIP	genesis and rapid intensification process
GV	Gulfstream V
IFEX	intensify forecasting experiment
JTWC	Joint Typhoon Warning Center
MCS	mesoscale convective system
NHC	National Hurricane Center
NSF	National Science Foundation
OW	Okubo-Weiss
PGI	PREDICT-GRIP-IFEX
PREDICT	Pre-Depression Investigation of Cloud-Systems in the Tropics
RF	research flight
SAL	Saharan air layer
TPW	total precipitable water

THIS PAGE INTENTIONALLY LEFT BLANK

ACKNOWLEDGMENTS

THIS PAGE INTENTIONALLY LEFT BLANK

I.   INTRODUCTION

A.   SYNOPSIS

The development of tropical disturbances into tropical storms has been a topic that many meteorologists have studied. However, due to the scarcity of data and lack of comprehensive theoretical models, it has been challenging to test hypotheses on the key physical processes involved in the development of tropical disturbances into tropical cyclones. To acquire the data necessary to study the development of tropical disturbances, and subsequently create an updated conceptual model on this phenomenon, the Pre-Depression Investigation of Cloud-Systems in the Tropics (PREDICT) Experiment was conducted. The PREDICT Experiment was based primarily on the three main hypotheses described in Dunkerton et al. (2009) and the conceptual model described therein is known popularly as the "marsupial paradigm." The marsupial paradigm's conceptual model for genesis consists of a tropical wave acting as a parent wave sheltering the juvenile proto-vortex until the vortex becomes self-sustaining (Smith and Montgomery 2012). The marsupial paradigm will be explained further in the Methodology Chapter.

In the experiment, data were acquired using dropsondes and flight-level data from aircraft flying at high altitude in both developing and non-developing tropical disturbances. The tropical disturbances observed include PGI27, PGI30, PGI36 (Fiona), PGI38 (ex-Gaston), PGI44 (Karl), PGI46 (Matthew), PGI50 (Nicole), and PGI48. There were a combined total of 25 flights and 561 dropsondes released from the National Science Foundation (NSF) GV aircraft alone (Montgomery et al. 2012).. The amount of data collected is sufficient to conduct a comprehensive study on the thermodynamic and kinematic flow structures that are present in a favorable cyclogenesis environment and that potentially contribute to tropical disturbance development

Among the quantities to be examined in this thesis, convective available potential energy (CAPE) and convective inhibition (CIN) are two thermodynamic

1

parameters that will be evaluated to help characterize the thermodynamic structure of the pouch region of the observed tropical disturbances. CAPE is the maximum amount of kinetic energy a positively buoyant parcel can acquire before it reaches neutral buoyancy. The opposite of CAPE is CIN, which is the amount of energy a particle must overcome to become positively buoyant. In the PREDICT experiment, moderate to high amounts of CAPE and low values of CIN were found by Smith and Montgomery (2012) to be present in the soundings taken in the pouch region of the tropical disturbances. These findings stand in contrast to what was obtained in Xu and Emanuel (1989) and Emanuel et al. (1994) for the large-scale tropical circulation on long time scales. Those authors found that there are only very small amounts of CAPE, which serve only to offset the dissipation in clouds. The discrepancy between these findings is due in part to the different definition of CAPE used by Emanuel and colleagues who assumed reversible ascent, which is strictly valid for non-precipitating convection. Significant CAPE and reasonably small CIN in the pouch region of tropical disturbances implies that some convective organization is possible before the wind-speed dependence in the moisture fluxes becomes important in the surface energetics (Smith and Montgomery 2012). While moderate to strong levels of CAPE and low levels of CIN have been shown to be present in a statistically significant number of soundings analyzed, Smith and Montgomery (2012) found that CAPE and CIN alone are not an indication of the development or non-development of a tropical disturbance.

This thesis will examine thermodynamic quantities such as the presence of CAPE, CIN, and the equivalent potential temperature (θ_e) profiles surveyed in one developing and two non-developing tropical disturbances not analyzed by Smith and Montgomery (2012). The thesis will examine also the kinematic flow structure of the disturbances. The CAPE and CIN values and θ_e profiles in relation to the geographical location of the "sweet spot" serve to further quantify thermodynamic properties of the pouch region of the tropical disturbances. The sweet spot is the location of where the critical latitude and trough axis intersect.

This intersection is a favorable location for the formation of a tropical depression strength vortex. The critical latitude (CL) is the latitude where the intrinsic phase speed between the sheltering wave pouch and proto-vortex goes to zero (Dunkerton et al. 2009). These observations become more relevant when looking at the kinematic flow structure of the disturbances. The parameters used to evaluate the kinematic flow structure boundary surrounding the proto-vortex are: area-averaged vorticity; vertical shear; co-moving wind streamlines; and the Okubo-Weiss parameter. These parameters will be defined in the Methodology Chapter. These parameters will be defined in the Methodology Chapter.

In summary, this thesis will quantify the thermodynamic and kinematic flow structure of the pouch and proto-vortex by studying the CAPE and CIN parameters; the moisture content of the profiles inferred by the maximum and minimum equivalent potential temperatures found from an average of the θ_e profiles; saturated equivalent potential temperature (θ_{es}) profiles; and the area-averaged vorticity, strain, and vertical wind shear in a co-moving framework using the marsupial paradigm. The kinematic metrics listed here will be examined to determine the strength of the kinematic flow structure boundary of the pouch. A relationship will then be established between the strength of the kinematic boundary and the thermodynamic metrics measured in the pouch (Dunkerton et al. 2009).

B.   MOTIVATION

The development of tropical disturbances into tropical storms is one of the greatest impacting meteorological events to the United States Navy. Dunkerton et al. (2009), Montgomery et al. (2012), and Rutherford and Montgomery (2012) provided strong evidence in support of the marsupial paradigm construct. However, a thorough understanding of the key processes associated with how tropical disturbances develop into tropical storms remains incomplete. As a result, the accurate prediction of a tropical disturbance into a tropical storm is rarely greater than 48 hours (Dunkerton et al. 2009). This thesis will attempt to further the research previously cited in this paragraph.

The Joint Typhoon Weather Center (JTWC) reports that there were eight sorties in both the 2013 and 2012 calendar year. Additionally, there were 48, 28, and 15 diverts in the respective calendar years 2013, 2012, and 2011 due to adverse weather (V. Es 2014, personal communication). As the reader can imagine, this can be very costly as a sortie causes all vessels located in a port to leave that port to avoid inclement weather, and a divert causes a vessel to alter its optimal track in order to avoid inclement weather. Figure 1, taken from a Joint Typhoon Warning Center (JTWC) Mission Brief, illustrates how many tropical cyclones the Pacific Forces have to contend with. These sorties and diverts can be very costly to the Navy, and the more advanced warning of inclement weather the warfare commanders have, the more fiscally savvy their decisions will be in routing vessels out of harm's way.
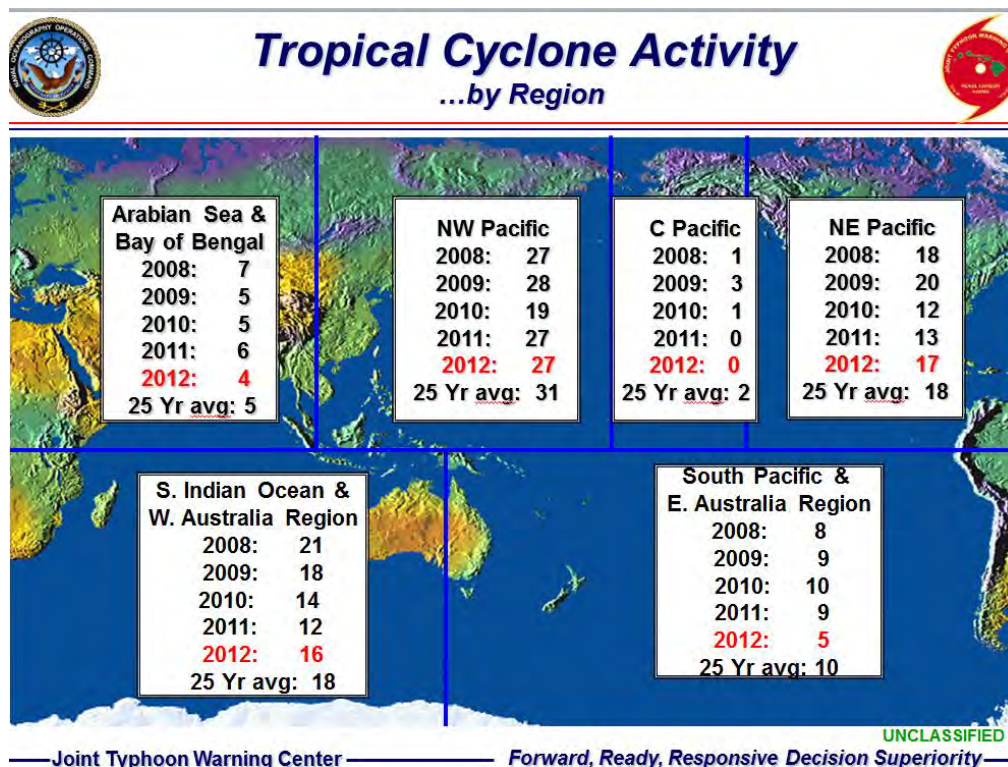
Figure 1.   PowerPoint slide from Joint Typhoon Warning Center's Mission Brief, which outlines the tropical cyclone activity in the Pacific and Indian Ocean (V. Es 2014, personal communication).

The Pre-Depression Investigation of Cloud-Systems in the Tropics (PREDICT) Experiment as described in Montgomery *et al*. (2012) was a dedicated field study that set out to acquire empirical data to quantify thermodynamic and kinematic parameters in developing and non-developing tropical disturbances in the Atlantic Ocean. By studying these parameters, a more thorough understanding of the nature of why tropical disturbances develop or do not develop can be achieved. The importance of this improved understanding is paramount to give Department of Defense (DOD) forecasters more lead time in predicting which tropical disturbances will develop in any basin. Once this is achieved, the overall benefit to the Navy will be great as more lead time will be given to the commanders responsible for routing navy vessels out of the destructive path of tropical storms.

C.   BACKGROUND

This thesis uses data collected from the National Science Foundation sponsored PREDICT experiment conducted from August 15 to September 30 of 2010 in the Caribbean and West Atlantic Ocean. This experiment specifically set out to conduct research missions in tropical disturbances that may or may not develop into a tropical storm. Each research mission was designated as RF (research flight) followed by a number to specify the specific flight for the various tropical disturbances. Table 1 summarizes the flights and named disturbances studied in the PREDICT experiment (Montgomery et al. 2012).

SYSTEM	Description	First identification	First mission	First NHC advisory	Flights (days)	Drops
PGI27	Nondeveloping African wave	8 Aug	17 Aug	None	2 (2)	48
PGI30	Nondeveloping African wave	14 Aug	21 Aug	None	2 (2)	38
PGI36 (Fiona)	Developed African wave	25 Aug	30 Aug	2100 UTC 30 Aug	3 (3)	83
PGI38 (ex-Gaston)	Failed redevelopment of African wave	28 Aug	2 Sep	1500 UTC 1 Sep	5 (5)	109
PGI44 (Karl)	Developing non-African wave	9 Sep	10 Sep	2100 UTC 14 Sep	6 (5)	127
PGI46 (Matthew)	Developing wave of uncertain origin	16 Sep	20 Sep	1800 UTC 23 Sep	4 (4)	83
PGI50 (Nicole)	Developing Caribbean gyre	26 Sep	28 Sep	1500 UTC 28 Sep	2 (2)	47
PGI48	May have become Otto	26 Sep	30 Sep		1 (1)	26

Table 1.   This table displays the disturbances studied in the PREDICT experiment (from Montgomery et al. 2012).

To determine whether an identified tropical disturbance would be suitable for scientific investigations by the Gulfstream V (GV) aircraft, several techniques were relied upon. First, satellite imagery, surface and upper air products, oceanic products, and global numerical model forecasts were examined to determine which tropical disturbances should be evaluated. Further analysis of numerical models, including Global Forecast System (GFS) and European Centre for Medium Range Weather Forecasts (ECMWF), was then conducted to determine how favorable the conditions of the disturbance were to development (Montgomery *et al*. 2012). This thesis is based on the premise tropical cyclogenesis is largely determined by the marsupial paradigm, which will be explained in much more detail under the Methodology Chapter. Once a tropical disturbance was deemed an appropriate candidate for study, pouch products were created that would help develop a suitable flight pattern to sample the tropical disturbance with dropsondes and other flight-level data on board the GV. The first research flight (RF01) was a test flight not examined in this thesis (Montgomery *et al*. 2012).

Pouch products used in this thesis include information such as the Earth relative and co-moving streamlines, and the Okubo-Weiss (OW) parameter of the tropical disturbance, tropical depression, or tropical storm of interest. The GV flight patterns generally sampled an area of 500 sq. km, which was centered on the sweet spot (Montgomery *et al*. 2012). Further details on the parameters of pouch products will be given in the Methodology Chapter.

D.   TROPICAL DISTURBANCES EXAMINED

This thesis will examine data from the first three tropical disturbances observed during the PREDICT experiment. These three tropical disturbances are identified as PGI27, PGI30, and PGI36. The term PGI followed by two numbers is the designator used for each disturbance sampled by the PREDICT experiment. PGI is an abbreviation for the three-agency U.S. Government effort that worked together on this project: PREDICT-GRIP-IFEX. GRIP is an abbreviation for the NASA-supported experiment Genesis and Rapid Intensification Processes, and IFEX is an abbreviation for the National Oceanic and Atmospheric Administration's supported experiment: Intensify Forecasting Experiment. PGI27 and PGI30 did not develop into a tropical storm. PGI36 was immediately upgraded to a tropical storm named Fiona after the first research flight was conducted (Montgomery *et al*. 2012).

For more information on the other research flights in the PREDICT experiment or the logistical aspects of how the experiment was conducted, the reader is referred to the article entitled: "Pre-Depression Investigation of Cloud Systems in the Tropics (PREDICT) Experiment" by Montgomery *et al*. (2012).

1.   PGI27

PGI27 was observed as an easterly wave at the west coast of Africa on 08AUG2010 translating with a speed of 3.2 $m \cdot s^{-1}$ westward. The first and second flights were conducted on 17AUG2010 and 18AUG2010, designated RF02 and RF03, respectively. These flights were executed after convective cells

developed within the identified pouch on 14AUG2010, and organized deep convection with high ice water content was observed on 16AUG2010. During the flights, an area of deep convection was observed. In post analysis, PGI27 was suspected of not developing due to weak circulation and dry air intrusion (Montgomery *et al*. 2012).

An east-to-west lawnmower-like flight pattern using meridional legs was conducted during RF02. Strong convection extended meridionally throughout the flight pattern (Raymond 2010a). Figure 2 shows a visible satellite image with the locations of the deployed dropsondes overlaid on the image.
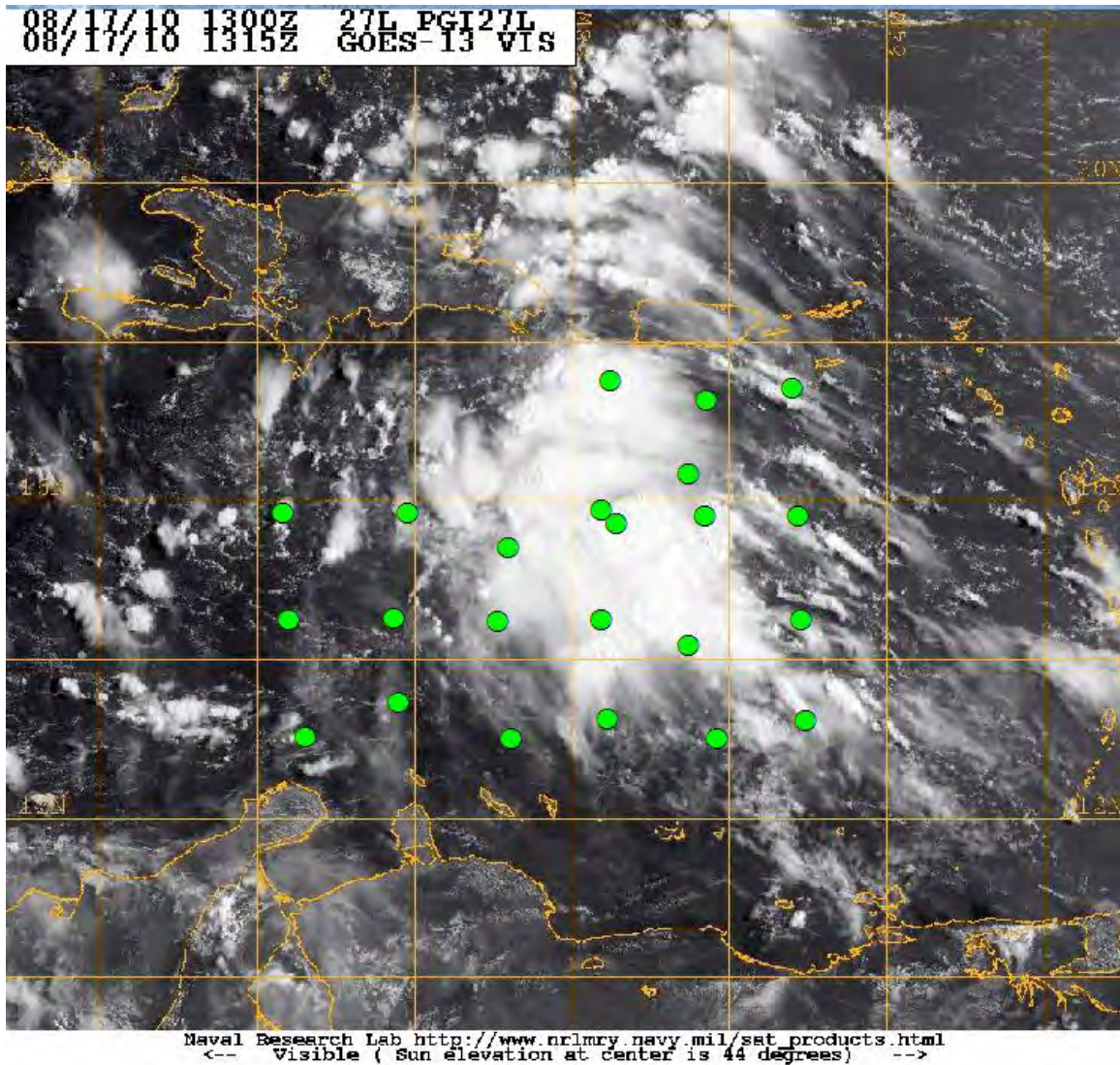
Figure 2.   Visible Satellite image from GOES-13 of RF02 with dropsonde positions overlaid as green circles (original image from Naval Research Laboratory-Monterey at http://www.nrlmry.navy.mil/TC/tc10/ATL).

For RF03, a lawnmower pattern was initially used similar to RF02, and the flight concluded with a box pattern midway through the deployment of dropsondes to improve the spatial resolution of the convective area. This flight pattern was able to sample around a developing mesoscale convective system (MCS) located on the northeastern portion of the pouch. In the PREDICT Science Director Summary for 18AUG2010, Dr. Chris Davis (2010b) writes,

"there was clearly an asymmetry to the circulation with a stronger southerly component on the east side of the pouch than a northerly component on the west side. An exception was observed at the surface, where northeasterly winds were observed on the west side of the pouch," and "an upper-level trough-ridge couplet" created "pronounced drying in the upper and even the middle troposphere." Figures 21 and 22 in the Results Chapter indicate both the possibility of dry air intrusion, and the strength of circulation being greater in the southeastern portion versus the northwestern portion. Figure 3 shows a visible satellite image midway during RF03 with the dropsonde positions overlaid on the image.
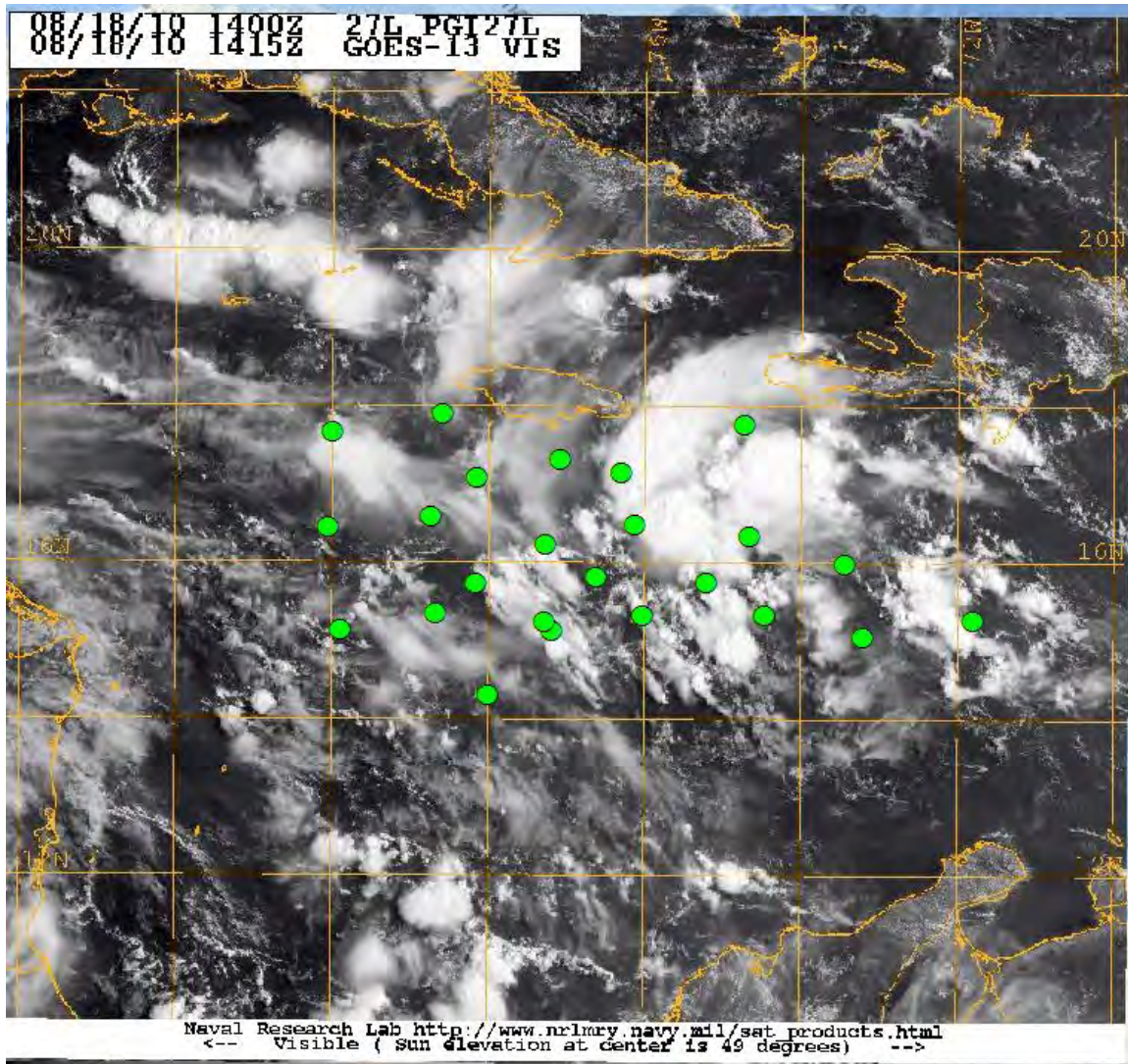
Figure 3.   Visible satellite image from GOES-13 of RF03 with dropsonde positions overlaid as green circles (original image from Naval Research Laboratory-Monterey at http://www.nrlmry.navy.mil/TC/tc10/ATL).

2.   PGI30

By all appraisals from mission scientists, PGI30 was considered a non-developing tropical disturbance located in a weak African easterly wave with dry air on the east and west side of the wave. The PREDICT Science Director Summary by Dr. Montgomery (2010) states, "the `wave-pouch' was bordered on the east side by SAL and the west side by dry tropical air from the subtropics and

middle latitudes." PGI30 had weak circulation strength, but enough observable convection inside the pouch to justify deploying sensors in the pouch. Two scientific missions were flown to study an obvious non-developing wave on 21AUG2010 and 23AUG2010, and these flights were designated as RF04 and RF05, respectively.

During the RF04 mission, the flight crew deviated from a square spiral pattern to an east-to-west lawnmower pattern with meridional legs. There were problems also with some of the dropsondes resulting in some of the dropsonde data being rendered unusable. From Dr. David Raymond's mission summary (2010b), the research flight's dropsondes were deployed in the pouch center. Additionally, Dr. Raymond observed deep, but weak, convection of the disturbance located in the southern portion of the pattern. The latter can be seen in the visible satellite image for RF04 in Figure 4.
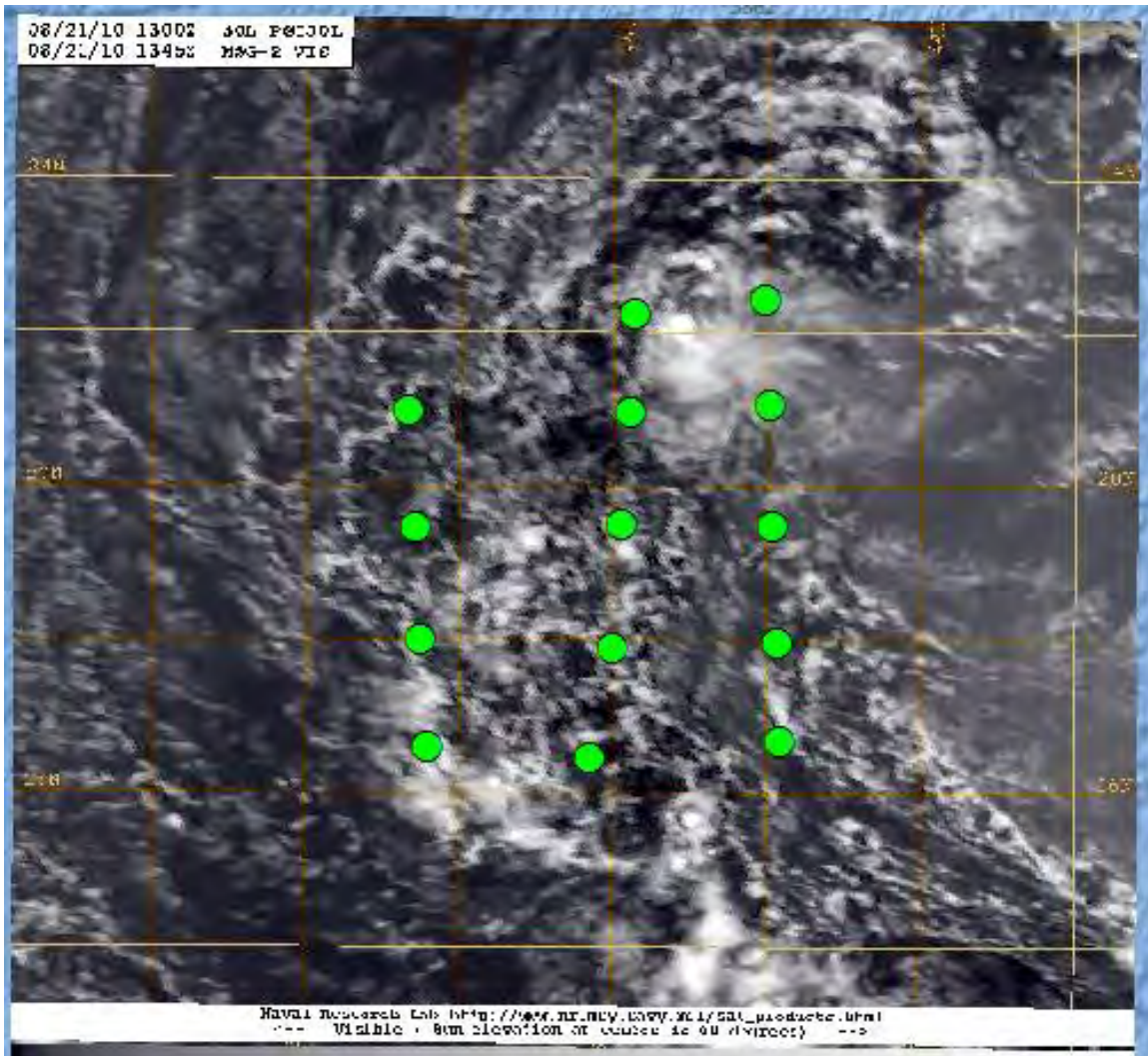
Figure 4.   Visible satellite image from MSG-2 of RF04 with dropsonde positions overlaid as green circles (original image from Naval Research Laboratory-Monterey at http://www.nrlmry.navy.mil/TC/tc10/ATL).

As will be shown later in the Results Chapter, PREDICT mission scientist summary by Dr. Michael Bell (2010b) indicated that data from RF05 has shown the disturbance was in decay with no observable pouch and only scattered convection among dry air masses during the time of that research flight. A large anticyclonic circulation east of the mission dominated the flow, which can be seen in the 700mb co-moving streamline graphic from the Montgomery Research Group archives in Figure 5. A lawnmower pattern was again flown over this area.
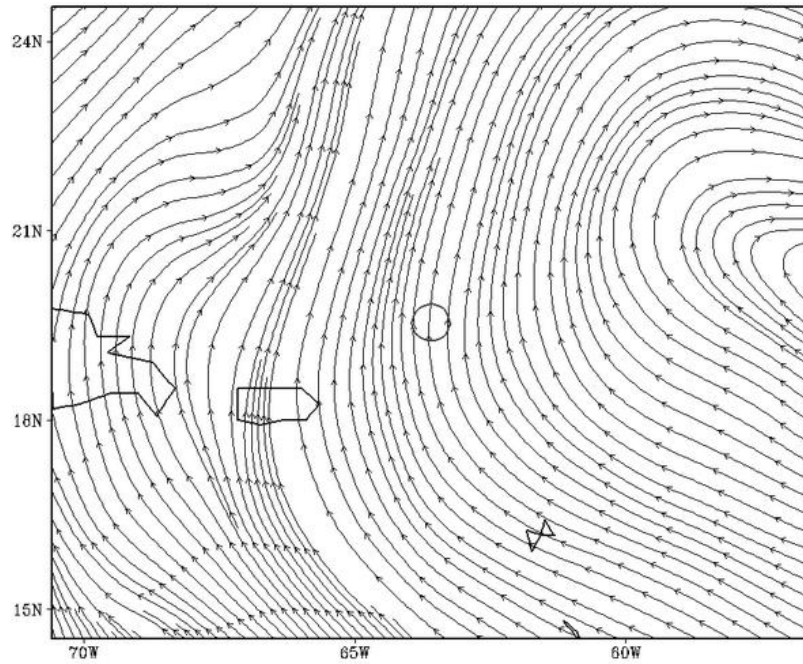
Figure 5.   Co-moving streamlines of RF05 valid during time of the drop.
The circle in the center of the figure is where the sweet spot
would be if a pouch was observed (from Montgomery 2014a).

Figure 6 shows the visible satellite image for RF05 with dropsonde positions overlaid. The visible satellite image reinforces the observations made in the previous paragraph concerning weak convection.
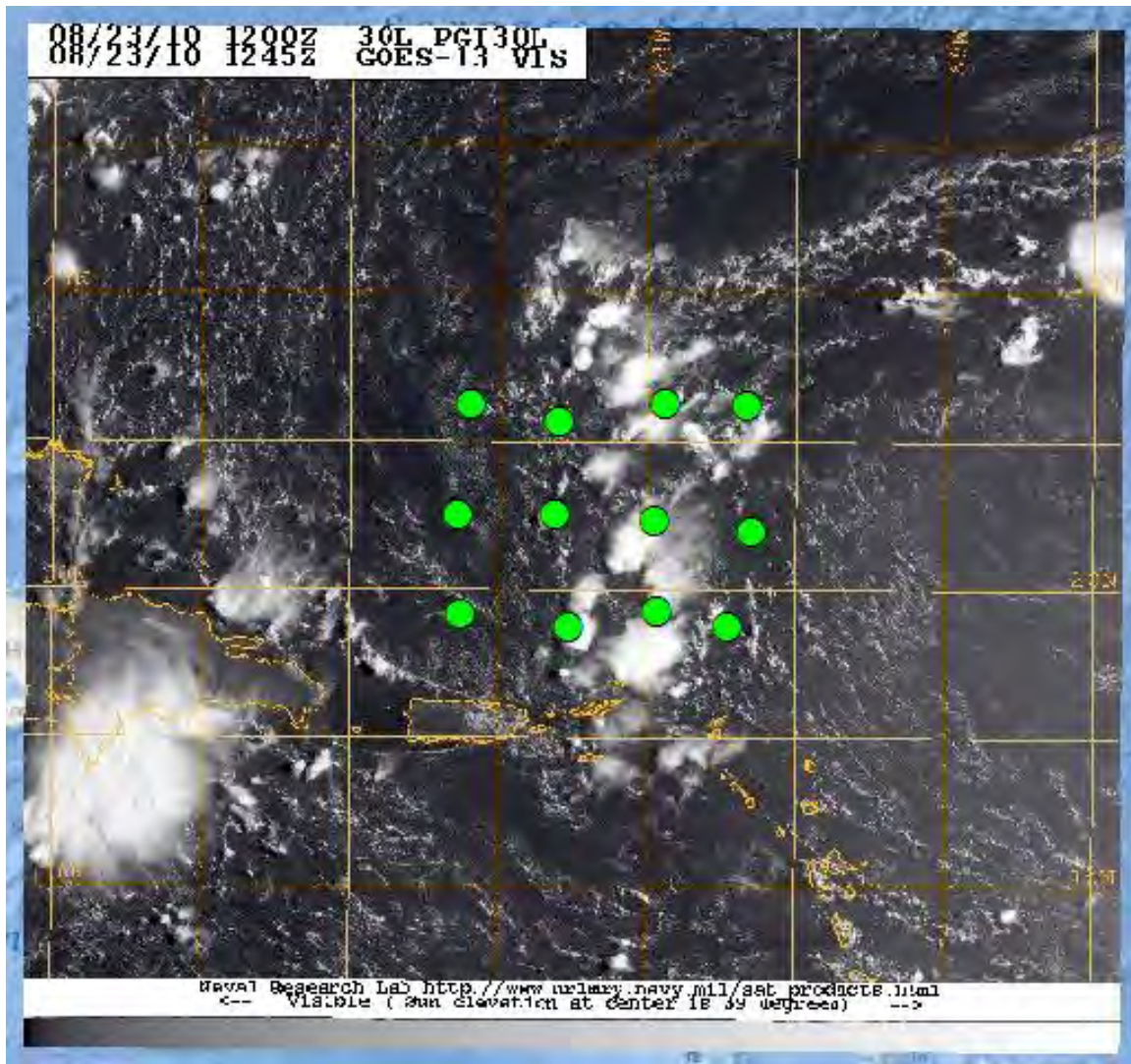
Figure 6.   Visible satellite image from GOES-13 of RF05 with quality
controlled dropsonde positions overlaid as green circles
(original image from Naval Research Laboratory-Monterey at
http://www.nrlmry.navy.mil/TC/tc10/ATL).

3.   PGI36 (Fiona)

The National Hurricane Center (NHC) Tropical Cyclone Report for Fiona
by Robbie Berg (2010) summarizes the history of Fiona (PGI36). Fiona
developed from a tropical wave that moved off the African coast on 25AUG2010.
The National Hurricane Center (NHC) designated PGI36 as an INVEST on
30AUG2010 due to strong cyclonic circulation and deep convection. Soon
thereafter, data from the first research flight (RF06) indicated that the disturbance

had enough cyclonic circulation to be classified as a tropical storm, and NHC promptly began warnings on Tropical Storm Fiona. Fiona continued to gain strength until late on 01SEP2010. Deep convection abated and a consistent northeasterly vertical shear was believed to be the key detrimental factor in Fiona's weakening late on 01SEP2010. On 03SEP2010, Fiona was between the mid-level ridge and the circulation from Hurricane Earl, where the upper level outflow from Earl produced 30 kts of vertical shear between two pressure levels for Fiona. This exposed Fiona's low level center and created an adverse kinematic environment for more deep convection. Fiona's pouch could no longer sustain the vortex to fully develop into a hurricane (Montgomery *et al*. 2012). Fiona was subsequently classified to a post-tropical cyclone on 04SEP2010 (Berg 2010). Research flights into PGI36 were flown on 30AUG2010, 31AUG2010, and 01SEP2010, and are referred to as RF06, RF07, and RF8, respectively.

The analysis provided in the Results Chapter for Fiona will not be used to draw conclusions for the marsupial paradigm. Fiona was past the point of genesis during the first research flight, and the hypotheses put forth by Dunkerton et al. (2009) were formulated for genesis. However, the kinematic flow structure and the thermodynamic properties of Fiona are useful to analysis from the lens of the marsupial paradigm as it shows how the hypotheses transition from a developing disturbance to a tropical storm.

A square spiral pattern was used for RF06. This was a very appropriate pattern given Fiona was well organized by this time, and there were no safety to flight concerns due to adverse weather areas during the research flight, which might have mitigated the desired placement of the dropsondes. As a result, the flight pattern was located in the middle of the strongest convection and in the vicinity of the predicted sweet spot of the parent wave. Strong low-level cyclonic circulation was immediately noticed during this flight (Bell 2010c), which will be examined in the Results Chapter. Figure 7 shows the visible satellite image overlaid with dropsondes for this research flight.
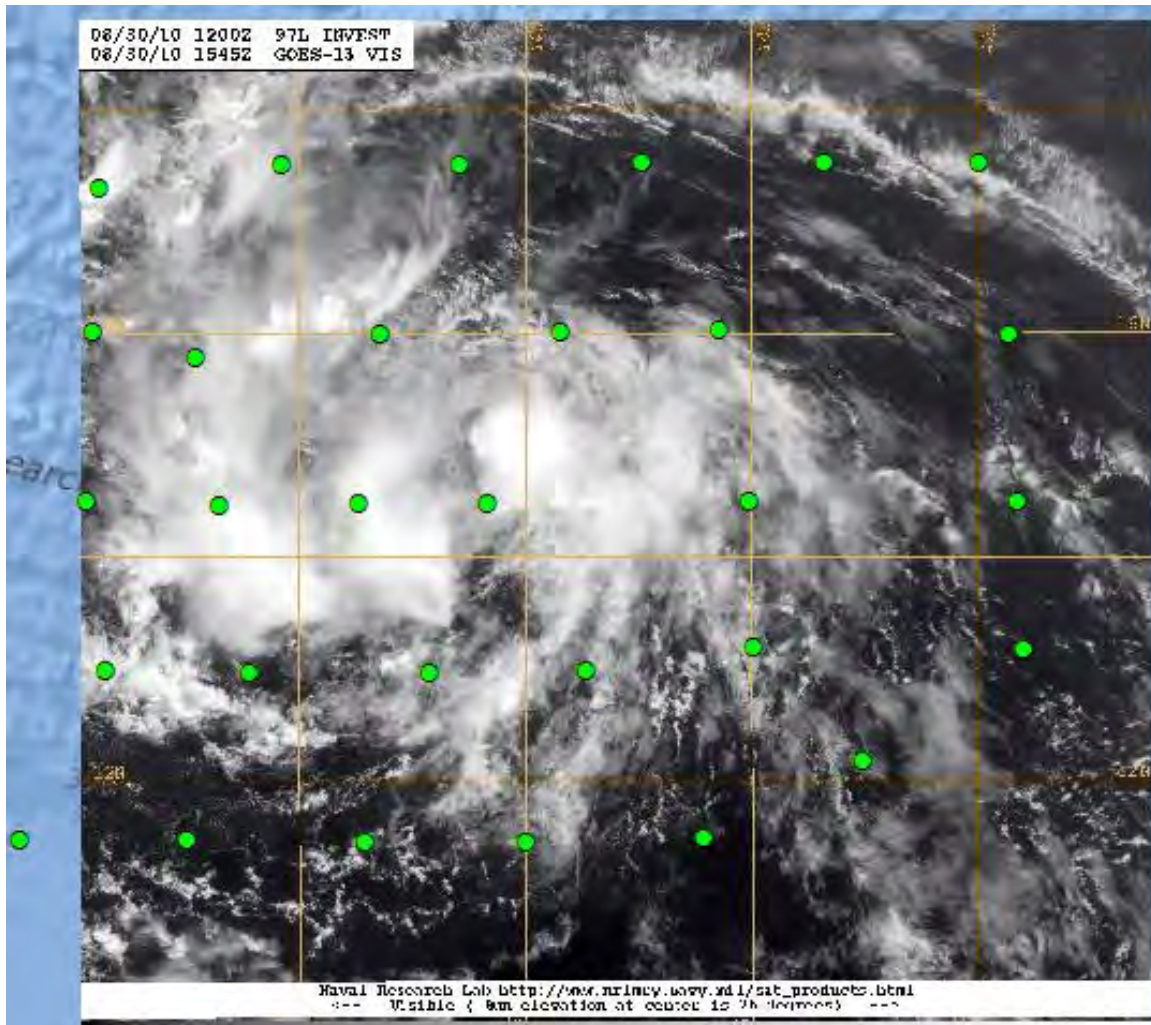
Figure 7.   Visible satellite image from GOES-13 of RF06 with dropsonde positions overlaid as green circles (original image from Naval Research Laboratory-Monterey at http://www.nrlmry.navy.mil/TC/tc10/ATL).

During RF07, it was noted that Fiona was moving faster than the forecast translation speed and the pattern had to be shifted westward. The square spiral pattern was successfully executed over the sweet spot, and the storm was again well sampled from the dropsondes deployed in the flight pattern (Bell 2010d). Figure 8 illustrates the visible satellite image midway through the flight overlaid with dropsonde positions.
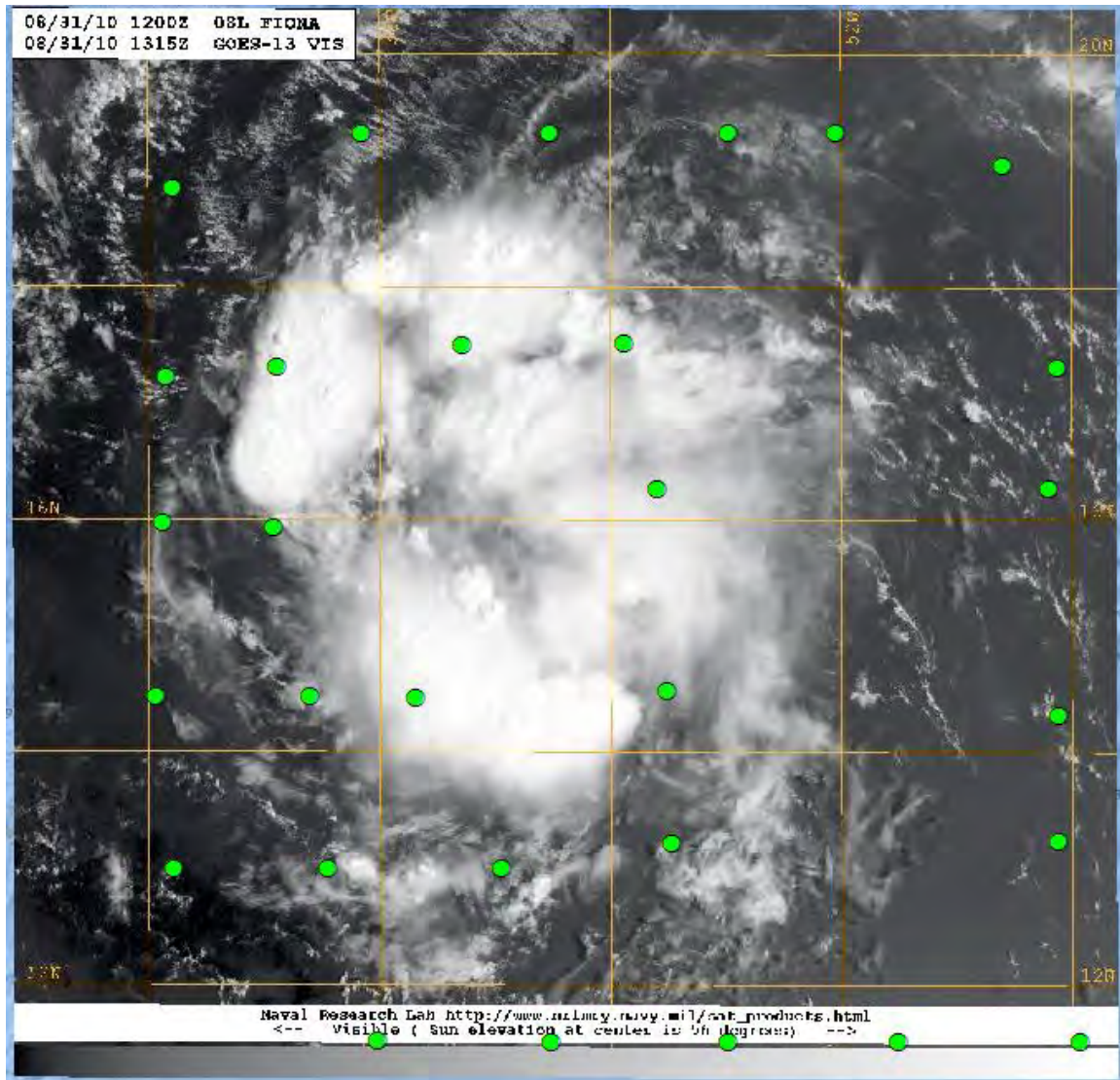
Figure 8.   Visible satellite image from GOES-13 of RF07 with dropsonde
positions overlaid as green circles (original image from Naval
Research Laboratory-Monterey at
http://www.nrlmry.navy.mil/TC/tc10/ATL).

Fiona was at its peak intensity during RF08. Another square spiral pattern with excellent placement around the convective center was deployed with an additional drop inside the convective center (Bell 2010e). Figure 9 shows the placement of the dropsondes overlaid on a visible satellite image around the midpoint of the research flight.
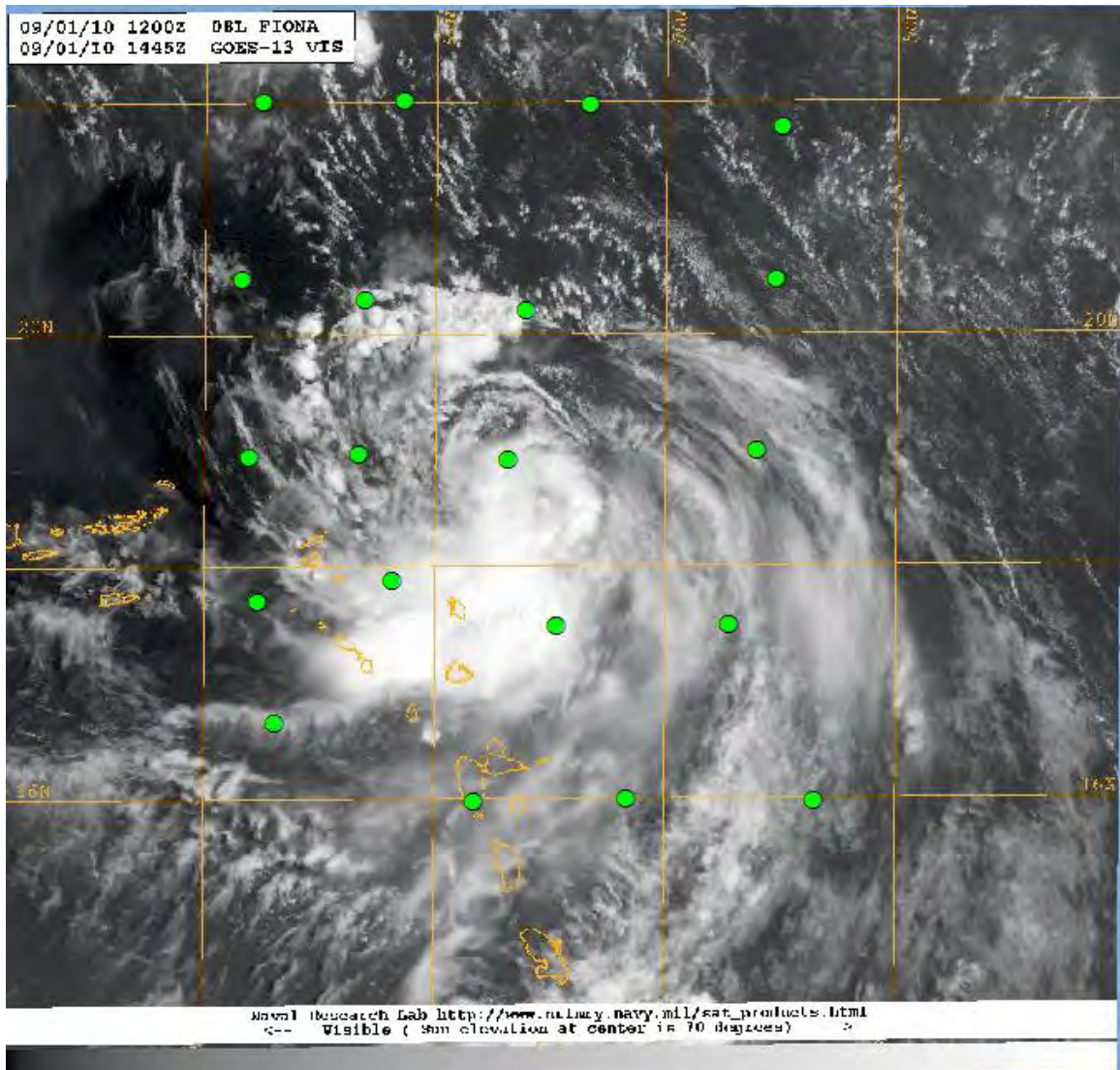
Figure 9.   Visible satellite image from GOES-13 of RF08 with dropsonde positions overlaid as green circles (original image from Naval Research Laboratory-Monterey at http://www.nrlmry.navy.mil/TC/tc10/ATL).

THIS PAGE INTENTIONALLY LEFT BLANK

II. METHODOLOGY

A. GENERAL APPROACH

This thesis uses dropsonde data from two tropical disturbances that did not develop and one disturbance that did develop into a tropical storm. The data was collected from the dropsondes deployed in the PREDICT Experiment. The PREDICT experiment set out to collect information about developing storms in order gain a better understanding of the parameters associated with a developing and non-developing tropical disturbance. Studies by Smith and Montgomery (2012) and Wang (2012) set out to investigate the thermodynamic environment in developing and non-developing tropical disturbances. Smith and Montgomery (2012) investigated the parameters of CAPE and CIN as well as the vertical structure of the thermodynamic properties such as virtual potential temperature and equivalent potential temperature of the dropsonde profiles. The Wang (2012) study highlighted the regional variations of the vertical structure of vorticity and moist equivalent potential temperature within the pouch.

This thesis is a continuation of the study by Smith and Montgomery and Wang *op. cit.*. The methods employed therein have been used to expand those studies to PGI27, PGI30, and Fiona. Additional kinematic flow parameters are examined also for these three systems to further quantify necessary conditions for development of a tropical disturbance. For information on how the dropsonde data was processed, the reader is referred to Appendix C.

Being a continuation of the Smith and Montgomery and Wang studies, this thesis is strongly guided by the marsupial paradigm. The marsupial paradigm as defined by Dunkerton *et al*. (2009) is based on three main hypotheses, and consists of the following:

H1. Proto-vortex cyclonic eddies instrumental in TC formation are intimately associated with the parent wave's critical latitude in the *lower troposphere*. The critical layer and Kelvin cat's eye within, formed as a result of

the wave's finite-amplitude interaction with its own critical latitude, contain a region of cyclonic rotation and weak straining/shearing deformation in which synoptic waves and mesoscale vorticity anomalies, moving westward together, amplify and aggregate on a nearly zero relative mean flow. This multi-scale interaction provides a dynamical pathway to "bottom-up" development of the proto-vortex from below.

H2. The critical-layer cat's eye of the parent wave provides a set of quasi-closed material contours inside of which air is repeatedly moistened by convection, protected to some degree from lateral intrusion of dry air and impinging vertical shear, and (thanks to its location near the critical latitude) able to keep pace with the parent wave until the proto-vortex has strengthened into a self-maintaining entity.

H3. The parent wave is maintained and possibly enhanced by diabatically amplified eddies within the wave (proto-vortices on the mesoscale), a process favored in regions of small intrinsic phase speed.

The overarching hypothesis for the marsupial paradigm as stated by Smith and Montgomery (2012) is that "tropical depression formation is greatly favored in the critical-layer region of the synoptic-scale, pre-depression wave or subtropical disturbance." This thesis will test the generality of the findings of Smith and Montgomery concerning CAPE and CIN within the critical layer or "pouch" region of identified tropical disturbances. The relationship of CAPE to the hypotheses **H1** and **H2** is believed to be that the presence of moderately strong CAPE (1000-2000 J/kg) allows air parcels moistened from the moisture flux from the ocean in the boundary layer to be raised through the lower to middle troposphere (Smith and Montgomery 2012). This thesis will also document the moisture content of the lower and middle troposphere. Additionally, possible relationships between the kinematic flow structure boundary and thermodynamic properties will be examined. Co-moving wind streamlines, the Okubo-Weiss parameter, area-averaged vorticity, and vertical shear will be the parameters

utilized to assess the kinematic flow structure boundary (Dunkerton *et al.* 2009). These parameters will be defined in section B and C of this chapter.

B.   THERMODYNAMIC ANALYSIS

CAPE is the equivalent work that can be released by the buoyancy force upon raising an air parcel through the atmosphere to its level of neutral buoyancy from an initial altitude near the surface. CAPE is calculated by computing said air parcel's virtual temperature compared to the environment it is lifted in and integrating the corresponding temperature difference (and buoyancy force per unit mass) until the level of neutral buoyancy is attained. The specific methodology used to calculate CAPE assumes a pseudo-adiabatic ascent to the level of neutral buoyancy and ignores the latent heat of fusion. The buoyancy force per unit mass is accounted for by the difference in the virtual temperature. Below are equations summarizing the CAPE calculations (Montgomery 2014b).

CAPE = PA-NA

$$PA = \frac{1}{2}u_{LNB}^2 - \frac{1}{2}u_{LFC}^2 = \int_{P_{LNB}}^{P_{LFC}} R_d(T_{vp} - T_{va})d\ln p$$

$$NA = CIN = -\int_{P_{LFC}}^{P_{parcel}} (T_{vp} - T_{va})R_d d\ln p$$

Here, PA is the positive area on a skew-t ln-p thermodynamic diagram, NA is the negative area on a skew-t ln-p thermodynamic diagram, u is the vertical velocity, LNB is the level of neutral buoyancy, LFC is the level of free convection, p is the pressure at the location of the various subscripts, T_{vp} is the virtual temperature of the parcel, T_{va} is the virtual temperature of the ambient environment, R_d is the gas constant for dry air, and $d\ln p$ is the differential of the natural log of pressure. These equations were from Roger Smith's Tropical Meteorology Lectures, which are found on the Montgomery Research Group webpage (2014b).

The integral of the buoyancy force per unit mass over height was calculated using the trapezoidal method between the dropsonde environment and the theoretical air parcel in 100 meter increments. This process is carried out five times: Starting at 100 meters above the surface to 500 meters above the surface in 100 meter increments where it is lifted to the level of neutral buoyancy. The average of these five trials was then computed for the CAPE. The averaging of multiple calculations of CAPE at different heights takes into account the air parcels lifting from different altitudes. The surface is excluded from this calculation because it can give much larger values that are not representative of the environment due to the often observed high but shallow moisture content observed near the surface. CIN is defined as the minimum amount of energy necessary for a parcel to be raised through the environment to the level of free convection. CIN is calculated by using the minimum value of the six negative integrals starting from the surface up to 500 meters above the surface in 100 meter increments where it is lifted to the level of free convection. The smallest magnitude of the six trials is chosen as the CIN value (Smith and Montgomery 2012).

Once these calculations are complete, CAPE and CIN are then plotted geospatially for each dropsonde that was deployed for each research mission. The geospatial values of CAPE and CIN for each research mission are then related to observations such as relative location to the vortex of the storm, relative location of the dropsonde in the pouch of the storm, and the strength of the vorticity and tangential winds of the storm (Smith and Montgomery 2012). Relationships between the values of CAPE, CIN, and storm related quantities are then examined.

An analysis of equivalent potential temperature is also performed in order to assess the relative dryness of the two disturbances and tropical storm studied in this thesis. All of the equivalent potential temperature (θ_e) profiles are graphed on a single graph for each research mission, and then averaged at each altitude range to form an averaged profile. The averaged saturated equivalent potential

temperature (θ_{es}) profile and the averaged virtual potential temperature (θ_v) profile were also calculated and graphed for each research mission. The maximum and minimum values of the area-averaged θ_e profile is subsequently subtracted from each other to find $\Delta\theta_e$. A high value of $\Delta\theta_e$ indicates a relatively dry area that is unfavorable for convection, and a low value of $\Delta\theta_e$ indicates a relatively moist area that is favorable for convection. The definitions employed herein for equivalent potential temperature and virtual potential temperature are given by Bolton (1980) and Smith (1997):

$$\theta_e = T(\frac{1000}{p})^{0.2854(1-0.28*10^{-3}r)} exp[(\frac{3.376}{TL} - 0.00254)r(1+0.81*10^{-3}r)]$$

$$\theta_v = (1+0.61r)*T(\frac{1000}{p})^{0.2854}$$

In the foregoing definitions, T is temperature. p is pressure. r is the water vapor mixing ratio (expressed as $g \cdot kg^{-1}$), TL is the temperature at the lifted condensation level. θ_{es} is found using the equation for θ_e where r is replaced by the saturation mixing ratio.

C. KINEMATIC ANALYSIS

The relative circulation of the tropical disturbance for each research mission was calculated using the methodology summarized in Figures 10 and 11 from Holton (1979) and Boothe and Montgomery (2012). Figures 10 and 11 illustrate the methodology used to calculate the relative circulation associated with a series of dropsondes. The wind speed and direction are taken from the dropsondes from each height in Figure 11. The strength of the winds are then projected onto the directional lines, which when multiplied by the length of the segment between the two midpoints adjacent to the dropsonde in the circulation pattern of Figure 11, gives a circulation element. When all of the subsequent circulation elements are added together, the total circulation in Figure 10 is achieved. From the calculated circulation, the averaged tangential velocity

25

around the circulation perimeter can be calculated by dividing the circulation by the perimeter of the circulation path. Similarly, from Stokes' theorem, the area-averaged relative vorticity within the region is calculated by dividing the circulation by the chosen area. Below are the equations used to calculate the circulation (C), averaged tangential velocity (V_T) and averaged vertical vorticity (ζ_{avg}) from circulation:

$$C = \oint V \bullet dl$$

$$V_T = \frac{C}{P} = \frac{1}{P}\oint V \bullet dl$$

$$\zeta_{avg} = \frac{1}{A}\iint_A curlV \bullet \hat{n}dA = \frac{1}{A}\oint V \bullet dl$$

where C is the relative circulation, P is the horizontal perimeter, V is tangential velocity, dl is the directional line element, A is the area, and $\hat{n}$ is the normal unit vector to the area element dA.

The results in Chapter 3 will show the specific paths used for each research flight, as well as the values of these three flow measures at the levels listed in Figure 11.

Circulation

$$C = \oint V \cdot dl$$

Average vorticity
C / area

Average tangential cyclonic wind
C / perimeter
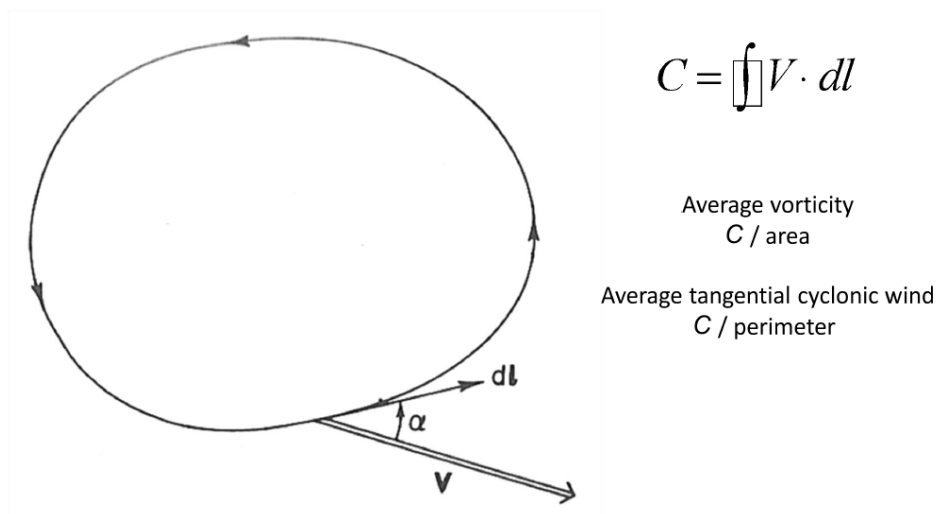
Figure 10.   Circulation around a chosen closed path is defined by a line integral of the velocity vector in the direction of the finite line segment. Image from Holton (1979).

Circulation

Determine midpoints between the drops.

Heading of dl is average of the headings of the two adjacent perimeter segments with the midpoints as the endpoints.

Wind values are simply read from the drop files. Some interpolation required (usually within 1 hPa).

Calculation at each point used the distance between the adjacent midpoints.

12 Levels (hPa)
200
300
400
500
600
700
750
800
850
900
925
950

Figure 11.   Summary of method to calculate the relative circulation from dropsonde data obtained in each research flight (from Boothe and Montgomery 2012).

27

The calculations used to determine the midpoint and distance between each dropsonde, the heading of the directional length (dl) of each dropsonde, and the wind value projected onto each directional length were taken from the website 'calculate distance, bearing and more between Latitude/Longitude points' constructed by Veness (2012).

The great circle distance (d) between each of the dropsonde points was calculated using the Haversine formula (Veness 2002):

$$a = sin^2(\Delta\varphi/2) + cos\ \varphi_1 \cdot cos\ \varphi_2 \cdot sin^2(\Delta\lambda/2)$$
$$c = 2 \cdot atan2(\sqrt{a},\ \sqrt{(1-a)})$$
$$d = R \cdot c$$
$\varphi = latitude$ (φ_1 and φ_2 are latitude points and
$\Delta\varphi$ is the distance between points), $\Delta\lambda = $ distance
between two $longitude$ points, $R = earth's\ radius$

And the formula for the bearing (θ) of the directional line (Veness 2002):

$$\theta = atan2(\ sin\ \Delta\lambda \cdot cos\ \varphi_2\ ,\ cos\ \varphi_1 \cdot sin\ \varphi_2 - sin\ \varphi_1 \cdot cos\ \varphi_2 \cdot cos\ \Delta\lambda\ )$$

Co-moving streamlines are an important element of the pouch product array used in this thesis. The co-moving streamlines were calculated by subtracting the zonal translation velocity at the level the pouch was tracked from the entire Earth relative velocity field at all levels, and computing the corresponding streamlines from this co-moving velocity field. The co-moving streamline field yields a slowly evolving velocity field on the scale of the pouch circulation and gives a reasonable estimate of the Lagrangian trajectories in and around the pouch circulation. While the Earth-relative frame and the co-moving frame yields the same amount of vorticity, seeing the circulation without the translation speed of the disturbance provides a much more intuitive feel for the vorticity that exists in the disturbance (Dunkerton *et al*. 2009). Appendix A compares the dropsonde observations against the global model analyses for the three disturbances examined here. The results show that the global model analyses for the three disturbances performed reasonably well.

The ECMWF forecast field with the closest forecast time to the research flight missions for the 925 mb and 700 mb layers were used in all cases except PGI30 in which GFS had a more accurate representation with the data collected in that mission.

Another parameter introduced by Weiss (1991) and McWilliams (1984) that proves insightful in the diagnosis of developing and non-developing tropical disturbances is the Okubo-Weiss parameter

$$OW = \varsigma^2 - S_1^2 - S_2^2 = (V_x - U_y)^2 - (U_x - V_y)^2 - (V_x + U_y)^2$$

which is vorticity squared (ς) minus the normal (S_1) and parallel (S_2) strain rates squared. U and V are the zonal and meridional velocities and the x and y subscripts indicate partial derivatives. The magnitude and units found throughout the Results Chapter of this thesis are $10^{-9}s^{-2}$. Positive values of OW reveal that vorticity is greater than strain; and the flow is rotationally dominant. Similarly, negative values of OW indicate that strain is greater than vorticity; and the flow is strain dominant. Positive values of the OW parameter are shown in the streamline pouch products in order to highlight the relatively strain-free regions where development would be favorable. In this way, OW is a useful quantitative measure of areas that tend to be immune from the horizontal straining motion deforming any convective elements that could potentially take place. The magnitude of the OW parameter reflects the threshold value that allows confidence that those areas are indeed regions with cyclonic vorticity that are not dominated by straining motions. One additional note to the reader is that the traditional sign of OW used by researchers studying large-scale geophysical turbulence has been reversed in applications to tropical cyclogenesis such as Montgomery *et al*. (2012) and in this thesis.

The last kinematic parameter examined in this thesis is vertical shear. Vertical shear gives an indication of how well aligned the kinematic flow structure will be throughout the vertical column of the disturbance. A high value of area-averaged vertical shear would indicate that the kinematic flow structure between

two pressure levels would tend towards vertical misalignment if aligned initially. If the disturbance is surrounded by dry air, this potential lack of vertical alignment will not provide the kinematic flow boundary throughout the vertical column of the disturbance that inhibits dry air intrusion above the proto-vortex. On the basis of the high-resolution cloud model simulations by Kilroy and Smith (2012), dry air intrusion above the proto-vortex is hypothesized to weaken updraughts. Weakened updraughts would limit the vorticity amplification throughout the vertical column via vortex tube stretching (Kilroy and Smith 2012).

The vertical shear acting on a candidate disturbance is quantified through an area-average of vertical shear over a three by three-degree horizontal region centered on the sweet spot of the pouch region. Strictly speaking, in order to estimate the impact of this vertical shear on a tropical disturbance, one should normalize this shear by the area-averaged tangential winds of the disturbance (Davis and Ahijevych 2012). Such normalization would allow a relative comparison between two different disturbances possessing significantly different perimeter-averaged tangential velocities. For example, simply comparing two systems' area-averaged vertical shear with an area-averaged tangential velocity of 5 $m \cdot s^{-1}$ and 10 $m \cdot s^{-1}$ would not produce completely meaningful results unless the difference in tangential velocity was taken into account also.

The area-averaged layer vertical shear was calculated using the winds from the 850 mb and the 200 mb levels, and the area-averaged pouch vertical shear was calculated using the winds from the 500 mb and 850 mb levels. These two vertical shear calculations were subsequently normalized by dividing the area averaged deep vertical shear by the area-averaged 500 mb level tangential velocity and the area averaged pouch vertical shear by the 700 mb level area averaged tangential velocity, representing the tangential velocity at the mid-level of each shear column. The resulting normalization produces a unitless quantity which is useful for comparing different disturbances or the same disturbance on different days (Davis and Ahijevych 2012).

III. RESULTS

This chapter is organized around the disturbances investigated during the experiment. In each disturbance the individual research missions flown on each day will be analyzed using the same methodology. The inferred relationships between the thermodynamic parameters and the kinematic flow structure of the various flights will then be summarized at the end of the chapter.

A.   PGI27

Figure 12 shows an analysis of the 700 mb ECMWF co-moving streamlines with the OW parameter displayed via color shading for August 17 and 18 for the disturbance identified as PGI27. The green dots identify the locations where dropsondes were released from the GV aircraft during the research flights on 17 and 18 August 2010 for RF02 and RF03, respectively. The outer-most circular ring is centered on the sweet spot of the pouch and extends to spatially encompass all of the dropsondes. The inner concentric rings are 75%, 50%, and 25% of the radius of the outermost ring. The concentric rings are used to assess regional variations of thermodynamic and kinematic variables within the pouch region of the wave disturbance. The black curve depicts the trough axis defined by the locus of points with meridional velocity equal to zero. The purple curve depicts the local critical level defined as the locus of points where the co-moving zonal velocity vanishes, or, in other words, where the Earth relative zonal velocity equals the phase speed of the parent wave disturbance (Montgomery 2014a)
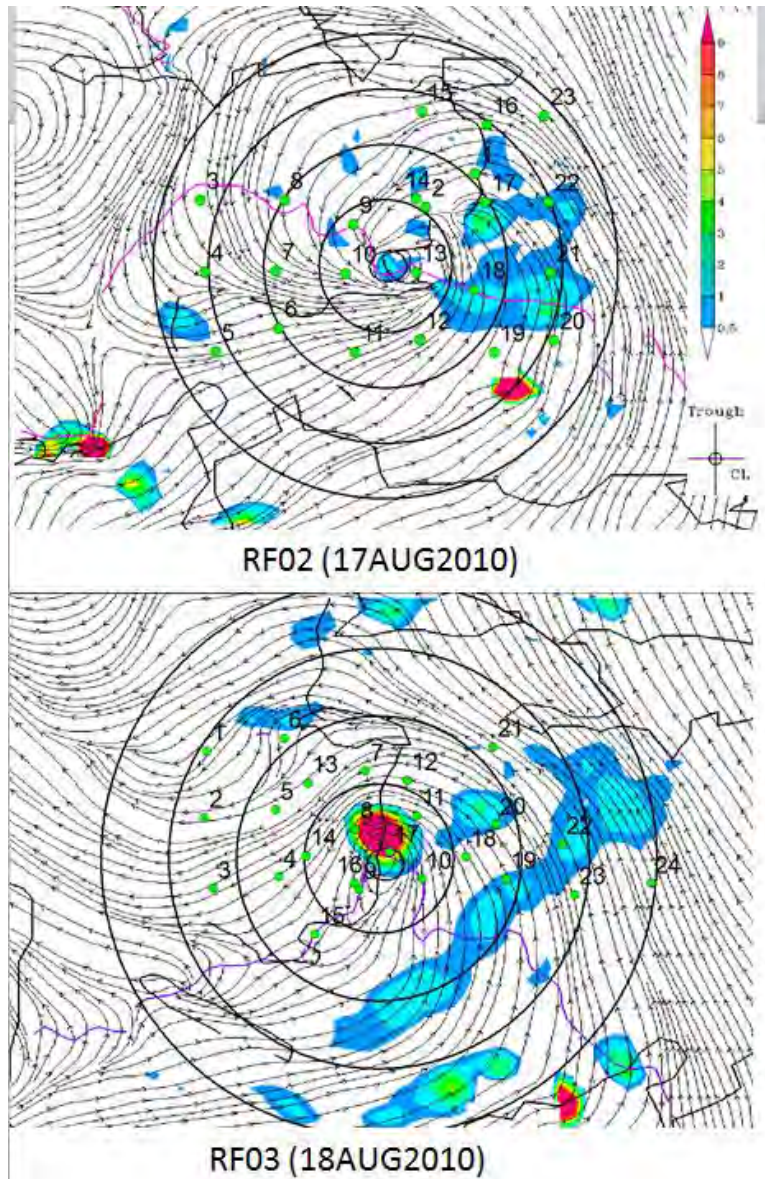
Figure 12. 700 mb ECMWF co-moving streamline and Okubo-Weiss
graphics of RF02 and RF03. RF02 is valid 2010081712 (0 hour
tau). RF03 is valid 2010081800 (12 hour tau). Numbers indicate
the chronological order of dropsondes
(after Montgomery 2014a).

The co-moving streamlines for 17 August suggest a recirculating flow in
the pouch region of the disturbance. The OW parameter is positive in an
elongated patch in the eastern portion of the pouch. On 18 August, the OW
parameter has increased near the sweet spot of the pouch. Elsewhere, OW has

a filamentary/linear structure on the south and east portion of the pouch and zero or negative values elsewhere. The co-moving streamlines for 18 August suggest less recirculating flow and more open flow in the pouch region of the disturbance. However, the OW parameter is approximately three to four times stronger in magnitude. This observation is consistent later in the Results Chapter when looking at the 700 mb vorticity values for RF02 and RF03. There is an additional elongated patch of positive OW east of the sweet spot. Given **H1**, the disturbance appears favorable for development as the increase in OW values indicates a growing region of cyclonic rotation and weak deformation where the aggregation of cyclonic vorticity is favored. Later in this section, the vertical shear and thermodynamic structure will also be examined to determine how favorable the disturbance may be (Dunkerton *et al*. 2009).

On an administrative note concerning Table 2 and subsequent tables displaying the values of CAPE and CIN, there were dropsondes that did not record wind values necessary for calculating circulation and/or thermodynamic parameters necessary for calculating CAPE and CIN. The presence or absence of these missing values are indicated by a W in the CAPE and CIN column if a dropsonde was unable to furnish CAPE and CIN values, but does furnish wind data. The letter N is in the CAPE and CIN if a dropsonde was unable to furnish CAPE and CIN values, and does not have wind values recorded; and an N in the CIN column only if the dropsonde does have accurate CAPE and CIN values recorded, but no wind data recorded.

	RF02			RF03	
objectid	CAPE	CIN	objectid	CAPE	CIN
1	3053	3	1	3582	6
2	W	W	2	2854	15
3	4456	14	3	2623	21
4	3634	12	4	253	149
5	3261	5	5	2716	26
6	2485	15	6	2043	43
7	3491	12	7	280	155
8	2916	29	8	1625	8
9	2696	17	9	1920	27
10	1700	13	10	W	W
11	1900	51	11	988	2
12	2566	28	12	W	W
13	2063	18	13	4024	4
14	1115	0	14	524	87
15	1742	17	15	1348	32
16	2551	29	16	1200	1
17	1567	27	17	1574	12
18	W	W	18	1032	7 N
19	2775	20	19	1291	83
20	2928	6	20	2695	6
21	1735	36	21	677	37
22	3154	16	22	790	60
23	W	W	23	2860	3
			24	3130	12

Table 2.   RF02 and RF03 CAPE and CIN values (J/kg) corresponding to the object-id (chronological drop order) numbers found in Figure 12. Concerning W and N: There were dropsondes that did not record wind values necessary for calculating circulation and/or thermodynamic parameters necessary for calculating CAPE and CIN. The presence or absence of these missing values are indicated by a W in the CAPE and CIN columns if a dropsonde was unable to furnish CAPE and CIN values, but does furnish wind data. The letter N is in the CAPE and CIN columns if a dropsonde was unable to furnish CAPE, CIN, and wind values; and an N in the CIN column only if the dropsonde does have accurate CAPE and CIN values recorded, but no wind data recorded. Table derived from NSF GV dropsondes.
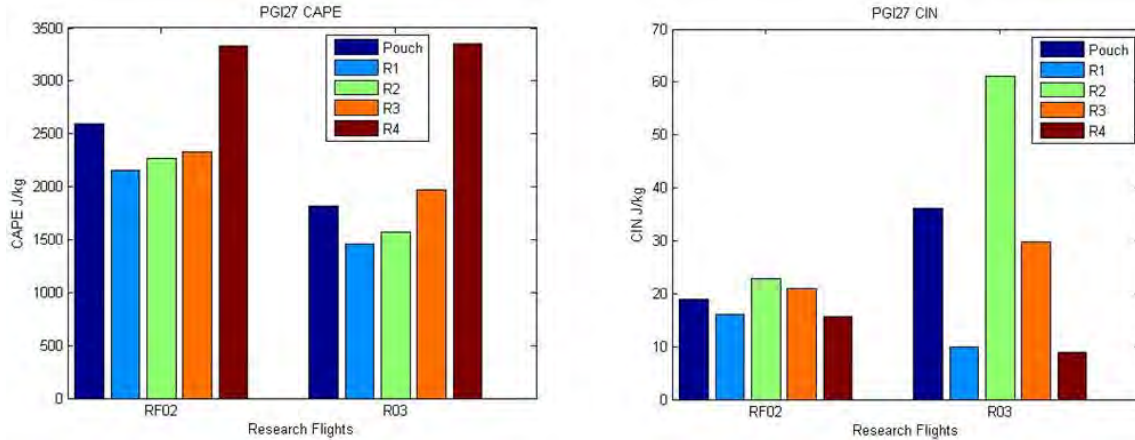
Figure 13.   CAPE and CIN for RF02 and RF03 plotted according to the dropsondes' distance from the sweet spot. Pouch is the average value of the dropsondes for the entire radius shown in Figure 12. R1 is the average value of the dropsondes in the inner radius extending to 25% of the largest radius. R2 is the average value of the dropsondes in the area between the 25% and 50% value of the largest radius. R3 is the average value of the dropsondes in the 50% to 75% area of the largest radius, and R4 is the average value of the dropsondes in the area between 75% value of the outer radius to the outer radius. Images derived from NSF GV dropsondes.

The averaged CAPE values found for all dropsondes released in PGI27 were 2589 J/kg and 1820 J/kg for RF02 and RF03, respectively, while the averaged CIN values were found to be 19 J/kg and 36 J/kg, respectively. The CAPE in both RF02 and RF03 gradually increases with increasing radius from the center of the pouch. Additionally, the values of CAPE decrease for all bins inside of 75% of the outer radius from the sweet spot, but the outer-most bin remains constant from RF02 to RF03. The values of CIN have on average increased from RF02 to RF03. A possible explanation for the change in CAPE and CIN from 17AUG2010 to 18AUG2010 offered by Dunkerton (2014, personal communication) is that convection tends to preferentially consume CAPE near the sweet spot, which according to the marsupial paradigm, is the most favorable place for deep convection, vortex tube stretching, and vorticity concentration. Overall, the prevalent result seen frequently in recent thermodynamic studies of developing and non-developing pouches from the PREDICT experiment as

discussed by Komaromi (2010) is that pouch-averaged CAPE is typically in the range of 2000 J/kg, and CIN is typically well under 50 J/kg for both developing and non-developing disturbances.

Figure 14 shows circulation paths chosen for RF02 depicted on a visible satellite image, together with 925 mb and 700 mb level co-moving streamlines and Okubo-Weiss from the ECMWF global model. The trough and critical latitude (CL) are represented by a black and purple curve, respectively. A circle representing the intersection between the trough and CL (the sweet spot) at 700 mb level is drawn on both the 700 mb and 925 mb level plots. Figure 15 accompanies Figure 14 as it displays the area-averaged vertical vorticity for RF02.
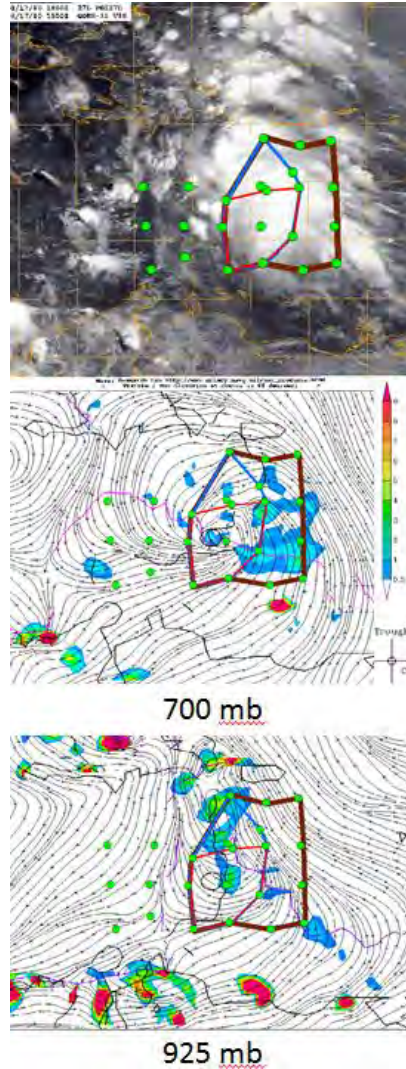
Figure 14. Circulation paths chosen for RF02 depicted on a visible satellite image and 700 mb and 925 mb ECMWF co-moving streamlines and Okubo-Weiss image in color valid 2010081712 (0 hour tau). The outer, middle, and inner circulation paths are indicated by brown, blue, and red circuits, respectively. See methodology for the calculation of OW values (magnitude and units: $10^{-9} s^{-2}$). The trough and critical latitude (CL) are represented by a black and purple line, respectively. A circle representing the intersection between the trough and CL (sweet spot) at 700 m is drawn on both the 700 mb and 925 mb plots (original satellite image from Naval Research Laboratory-Monterey at http://www.nrlmry.navy.mil/TC/tc10/ATL; co-moving streamline images after Montgomery 2014a).

As seen in Figure 14's co-moving streamline images, the 925 mb and the 700 mb level circulation centers are horizontally separated by a distance of 230 km. Figure 15 shows a difference in vorticity greater than $2 \times 10^{-5} s^{-1}$ between the 950 mb and the 700 mb levels for the inner and middle circulation paths. This relatively large difference in area-averaged vorticity indicates that the disturbance is either not vertically aligned or shallow. The co-moving streamlines previously mentioned in Figure 14 suggest that the flow region is not vertically aligned. From Davis and Ahijevych (2012), a disturbance does not need to be vertically aligned the entire duration of the development. The importance of vertical alignment appears to be that it occurs when other diabatic processes are occurring simultaneously. The next day's development will reveal that the disturbance did become vertically aligned.

Figure 15 shows a deep cyclonic circulation throughout most of the troposphere. All circulation paths become anti-cyclonic between the 300 mb and 200 mb levels.
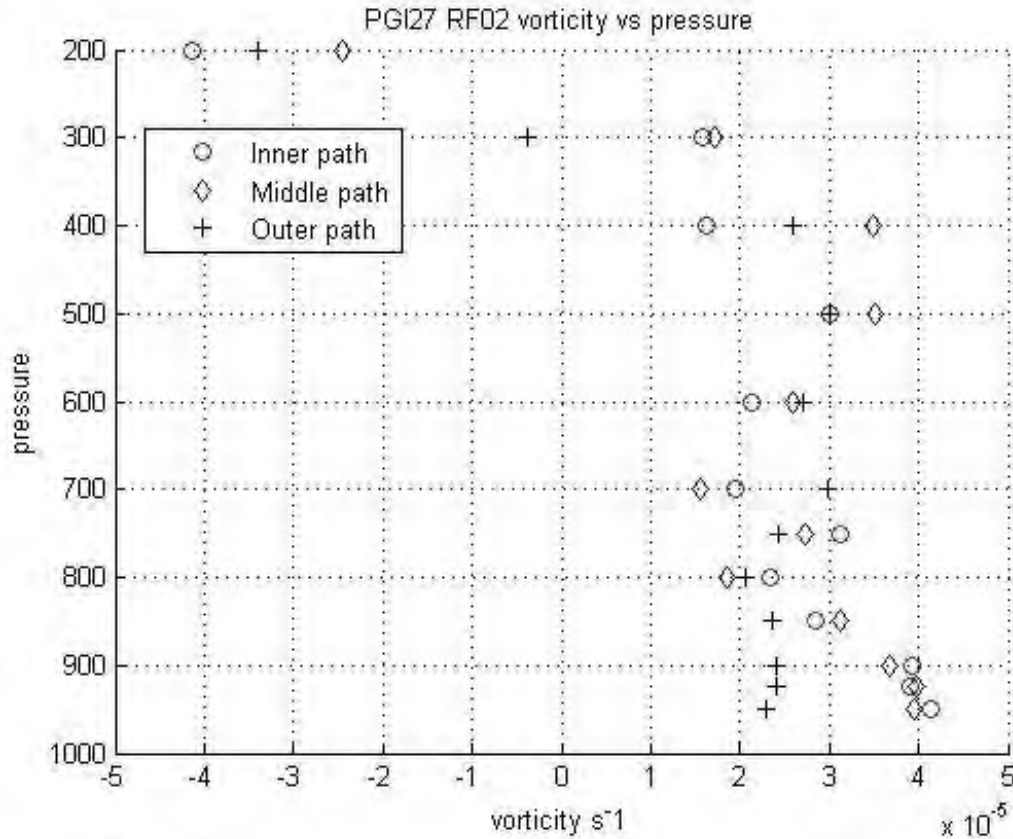
Figure 15. Vertical profile of area-averaged vorticity for Research Flight 02 (in PGI27) for the paths shown in Figure 14. Vorticity plotted in units of $10^{-5}\ s^{-1}$. The symbols denoting values from each circulation path is given in the legend. Image derived from NSF GV dropsondes.

As seen in Figure 16, the co-moving streamlines indicate the circulation is vertically aligned in the 925 mb and the 700 mb levels for RF03. Additionally, the OW values have a high concentration in the center of the circulation near the sweet spot as well as positive bands around the circulation. However, the co-moving streamlines also show the 700 mb level becomes more open. Figure 17 shows that, both circulation paths of RF03 strengthen with height until approximately 700 mb, which is the opposite finding of the inner and middle circulation of RF02. In RF03 the disturbance has its strongest vorticity values at the 700 mb level, while RF02 has its weakest vorticity values at the 700 mb level. Additionally, for RF03 the relative vorticity is cyclonic for the entire vertical profile.
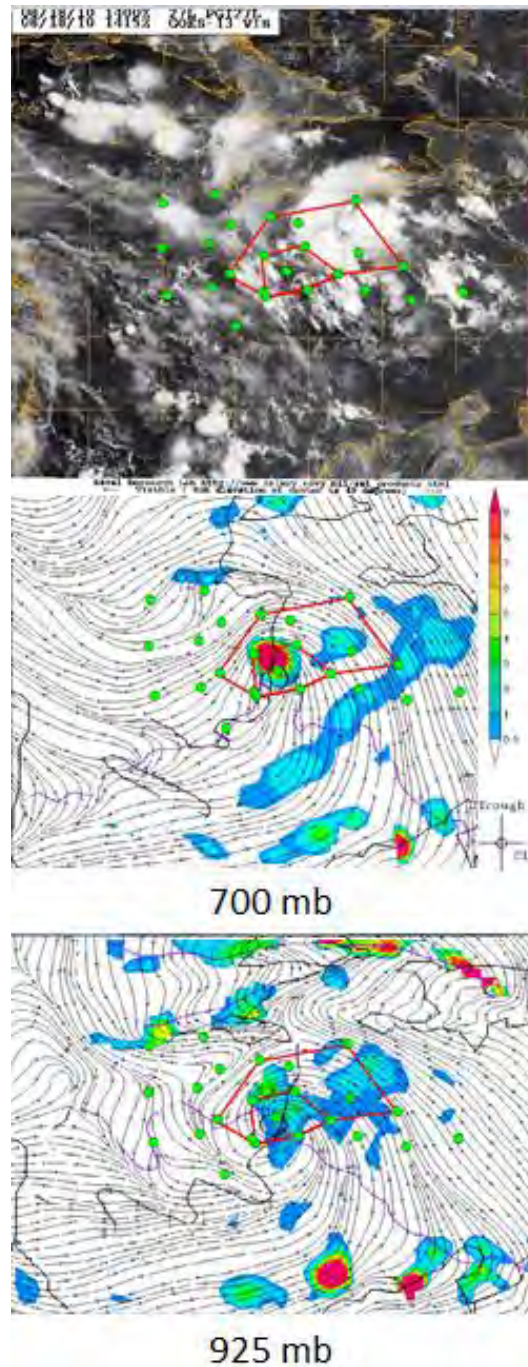
700 mb

925 mb

Figure 16.   Inner and outer circulation paths chosen for RF03 depicted on a visible satellite image and 700 mb and 925 mb ECMWF co-moving streamlines and Okubo-Weiss image in color valid at 2010081800 (12 hour tau). Refer to Figure 14 for description. (original satellite image from Naval Research Laboratory-Monterey at http://www.nrlmry.navy.mil/TC/tc10/ATL; co-moving streamline images after Montgomery 2014a).
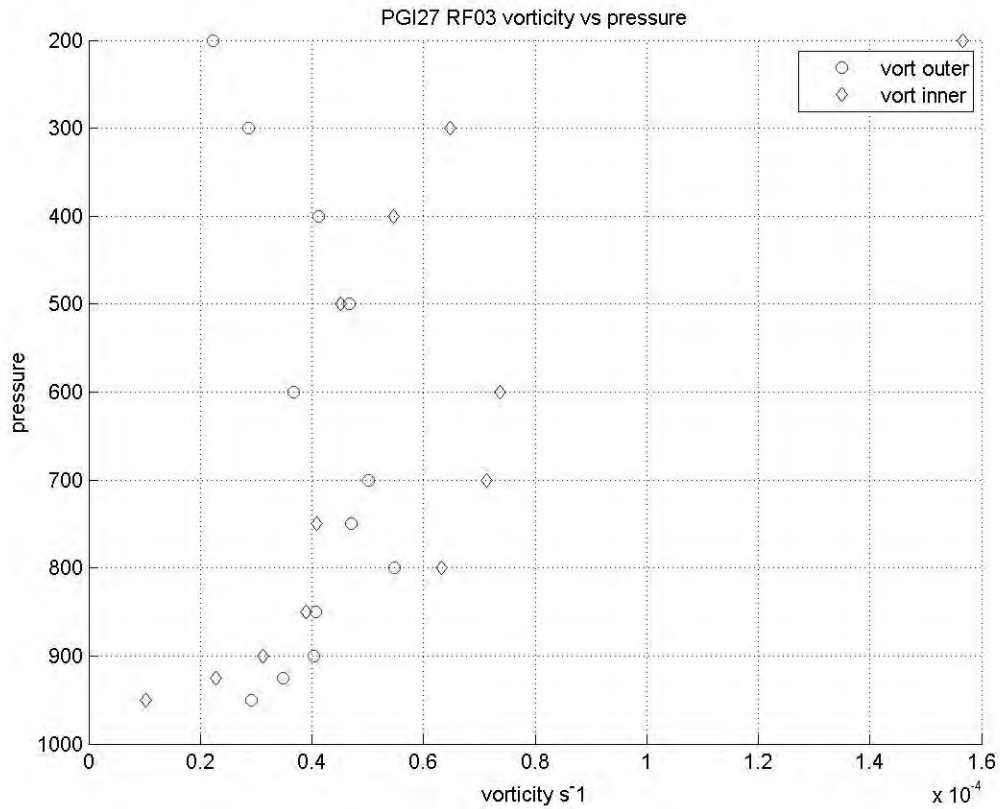
Figure 17.   Vertical profile of area-averaged vorticity for Research Flight 03 (in PGI27) for the paths shown in Figure 16. Vorticity plotted in units of $10^{-4} s^{-1}$. The inner circulation path is shown with blue diamonds and the outer circulation path is shown with red circles. Image derived from NSF GV dropsondes.

The large value of cyclonic vorticity at 200 mb for the inner path is slightly misleading. As Figure 21 (shown later) illustrates, this value is largely the result of the circulation path's location corresponding with the high winds associated with the edge of the 200 mb trough-ridge feature.

Overall, the vorticity and favorable kinematic flow structure has increased from RF02 to RF03. Due to the increased vorticity near the sweet spot inferred from Figure 16, **H1** would suggest this disturbance is kinematically favorable for development (Dunkerton *et al*. 2009).

Figure 18 gives a side-by-side comparison of the area-averaged vorticity for the inner path of RF02 and the outer path of RF03 from Figure 16 at vertical pressure levels from 300 mb and below. These two circulation paths were chosen as they had the most comparable area to each other. The reasoning for choosing areas of approximately the same size is to reduce the uncertainty given the possibility that higher vorticity values could be concentrated closer to the sweet spot (Davis and Ahijevych 2012). These higher concentrations would yield higher values of area averaged vorticity for a smaller circulation path area centered on the sweet spot. Additionally, the 200 mb level is not shown as the high winds corresponding to an upper tropospheric trough-ridge shown in Figure 21 skew the circulation values for the 200 mb level. RF03 has greater values of vorticity in comparison to RF02 from 900 mb and up for all vertical levels. Figure 18 and Figure 13 further show that as the overall CAPE decreased, the overall vorticity increased for this disturbance.
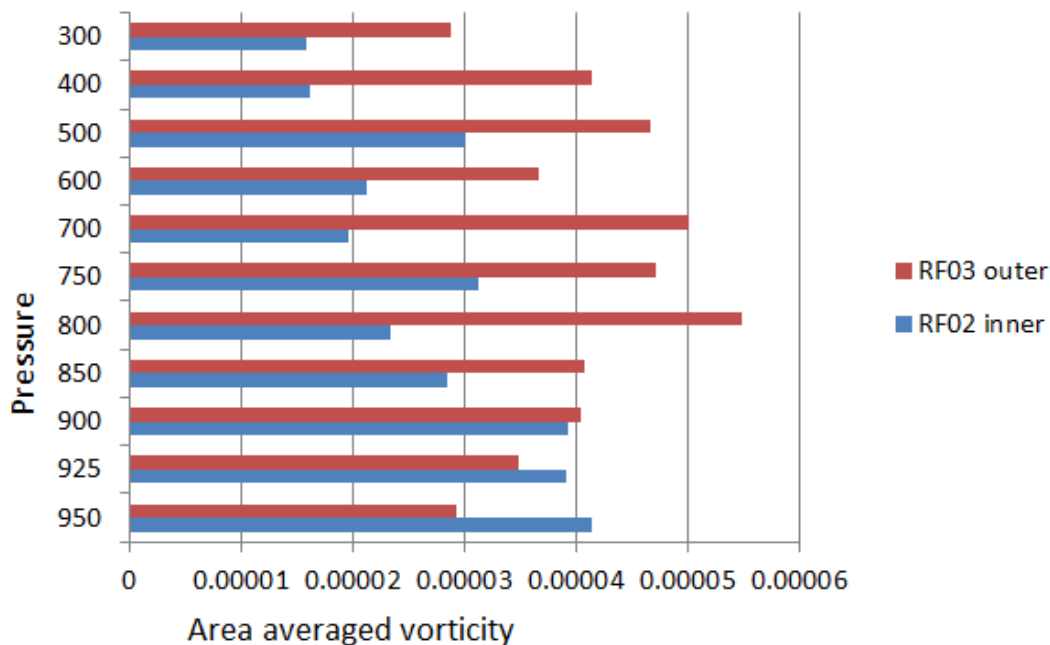
Figure 18.   Comparison of the area-averaged vorticity for RF02's inner circulation and RF03's outer circulation from Figure 14 and Figure 16 at different altitudes. Image derived from NSF GV dropsondes.

Figure 19 shows wind direction and magnitude for each dropsonde in the research flight. The figure illustrates the magnitude of the vertical wind shear at each location of the dropsondes deployed for the two research missions. Figure 20 shows the amount of vertical shear in the area of PGI27's pouch using the areally-averaged value of shear in the pouch. Figure 20 indicate the presence of low area-averaged vertical shear. Likewise, although the 925 mb and 500 mb dropsonde co-moving winds and 700 mb streamline images do not perfectly line up in Figure 19, the presence of a large vertical shear is not evident. This would suggest that reasons other than vertical shear in the middle to lower troposphere must be sought as to why PGI27 did not develop into a tropical storm. However, normalizing area averaged vertical shear, and examining the upper troposphere winds will reveal additional information.

Using the tangential velocity vs pressure graphs in Appendix B, the inner circulation path area-averaged tangential velocities for RF02 and RF03 are 1.3 $m \cdot s^{-1}$ and 2.8 $m \cdot s^{-1}$ for the 700 mb level and 2.1 $m \cdot s^{-1}$ and 1.8 $m \cdot s^{-1}$ for the 500 mb level. The normalized area-averaged pouch vertical shear for RF02 and RF03 are 3.1 and 1.4, respectively. The normalized area-averaged deep vertical shear for RF02 and RF03 are 2.9 and 4.6, respectively. Thus, on the vertical scale of the pouch, the normalized vertical shear decreases. In contrast, on the vertical scale of the troposphere, the normalized vertical shear increases.

On the basis of **H2**, as the magnitude of the normalized vertical shear decreases, the vertical kinematic boundary structure should be more effective at preventing dry air intrusion above the proto-vortex. The sweet spot can be subsequently moistened by deep convection (Dunkerton *et al*. 2009). In view of the opposing trends of the pouch vertical shear and deep vertical shear, no conclusive results can be ascertained.
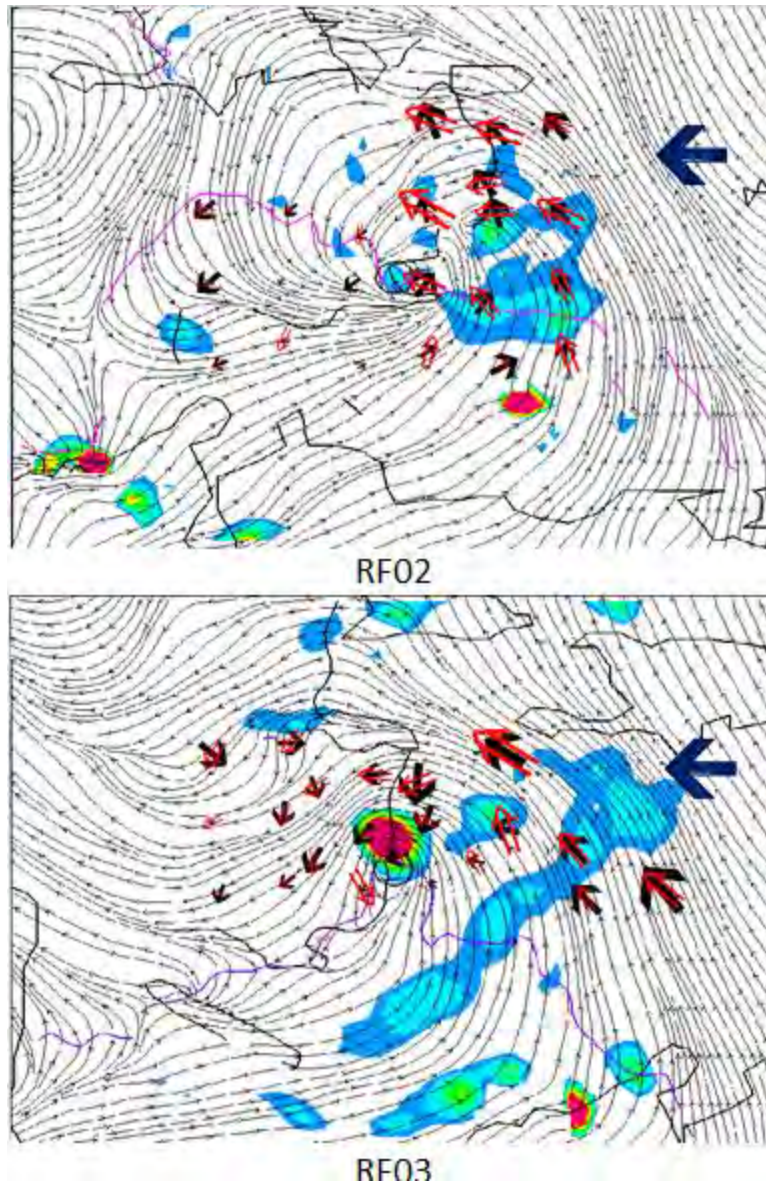
Figure 19.   Co-moving winds from dropsondes overlaid on the ECMWF co-moving streamlines and Okubo-Weiss-image for RF02 and RF03. The black arrows are 925 mb co-moving winds from NSF GV dropsondes, the red arrows are 500 mb co-moving winds from NSF GV dropsondes, and the co-moving streamlines and OW values are from the ECMWF 700 mb co-moving streamline product valid at 2010081712 (0 hour tau) and 2010081800 (12 hour tau) from top to bottom. All vectors are scaled to the same magnitude. The blue vector is drawn for scaling purposes and represents $10\, m \cdot s^{-1}$ wind speed (co-moving streamline images after Montgomery 2014a).
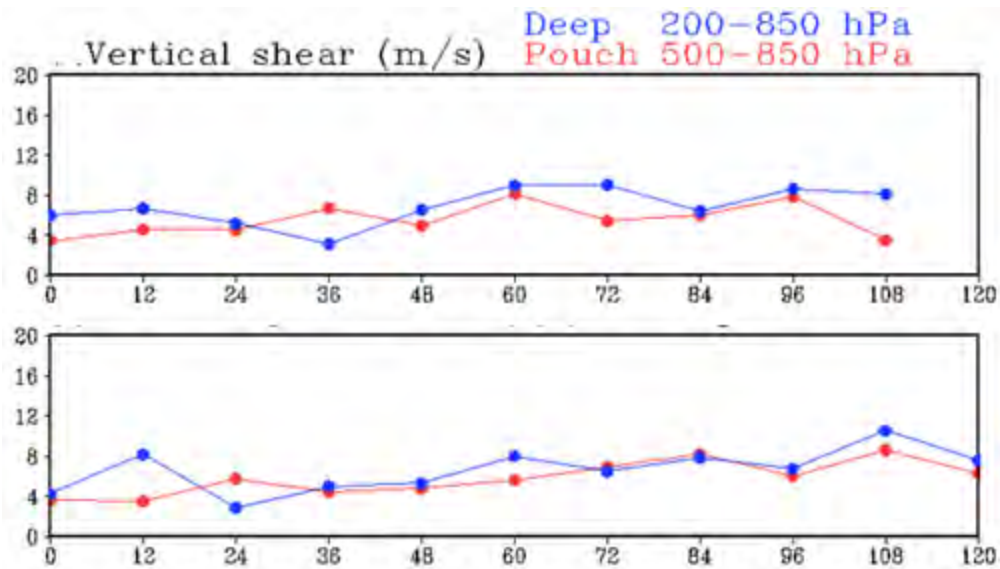
Figure 20. Vertical shear averaged over the three by three degree area of the pouch for RF02 (top) and RF03 (bottom). Values come from ECMWF. The valid forecast times are 2010081712 and 2010081800 from top to bottom, respectively (from Montgomery 2014a).

In the foregoing discussion, we are using an areal-averaged vertical shear as a way of estimating the quantitative strength of vertical shear acting on the pouch region. Figure 21 shows wind magnitude and direction at the 200 mb level (green arrows), 400 mb level (red arrows), and 925 mb level (black arrows). An examination of Figure 21 suggests that the deep shear vertical average is quite substantial over the western side of the disturbance, but not completely revealed in the areal-averaged measure. This is due to the area-averaged vertical shear only accounting for a three-by-three degree box centered on the sweet spot. Comparing the 925 mb co-moving winds to the 200 mb co-moving winds suggests there is a significant amount of vertical wind shear. Additionally, by comparing the 200 mb winds to the 400mb winds, the predominant amount of shear appears to reside above the middle troposphere. The strong wind from the 200 mb level ridge-trough feature thus appears to be a hindrance for the development of PGI27.

45
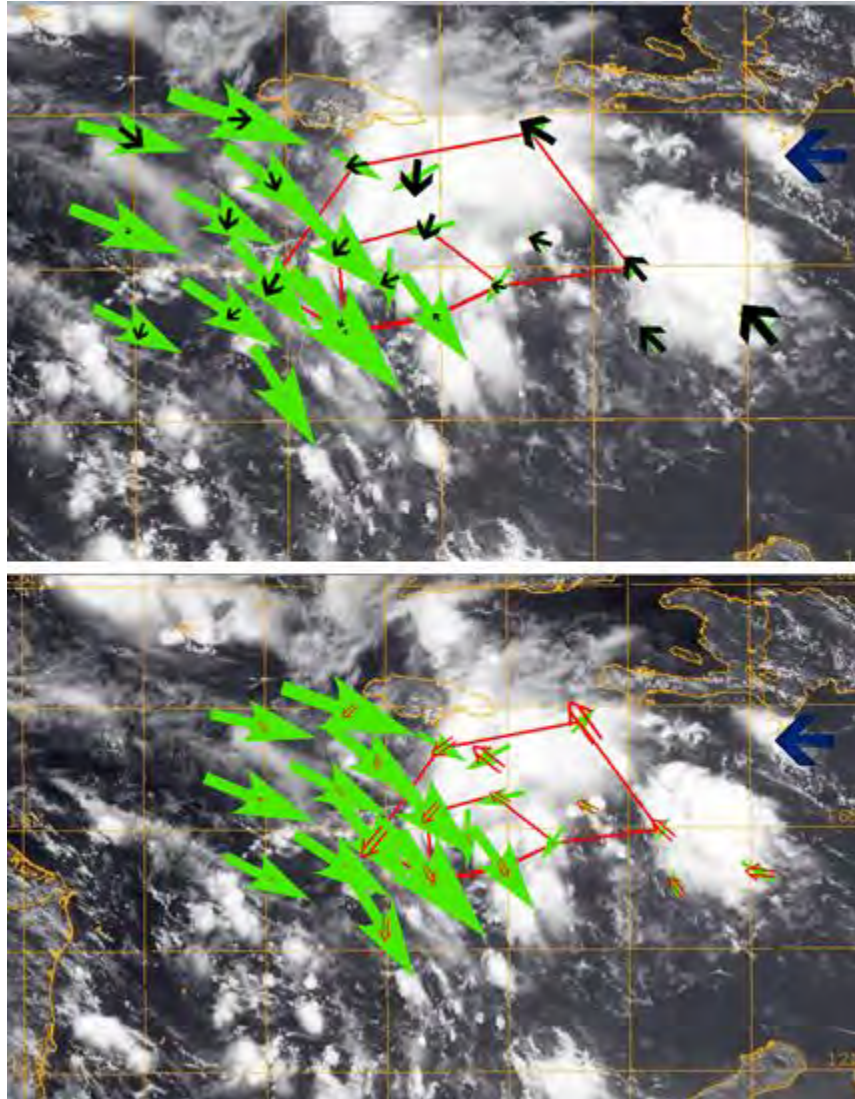
Figure 21.   Co-moving winds from dropsondes overlaid on the visible satellite image for RF03. The black arrows are 925 mb co-moving winds, the red arrows are the 400 mb co-moving winds, and the green arrows are 200 mb co-moving winds from NSF GV dropsondes. All vectors are scaled to the same magnitude. The blue vector is exclusively shown for scaling purposes and represents $10\,m \cdot s^{-1}$ winds. (original satellite image from Naval Research Laboratory-Monterey at http://www.nrlmry.navy.mil/TC/tc10/ATL).

Figure 22 shows the equivalent potential temperature, saturated equivalent potential temperature, and virtual potential temperature profiles throughout the co-moving flow structure of RF03. Figure 22 enables relationships

to be made between the co-moving winds and the amount of moisture entering or escaping the pouch.
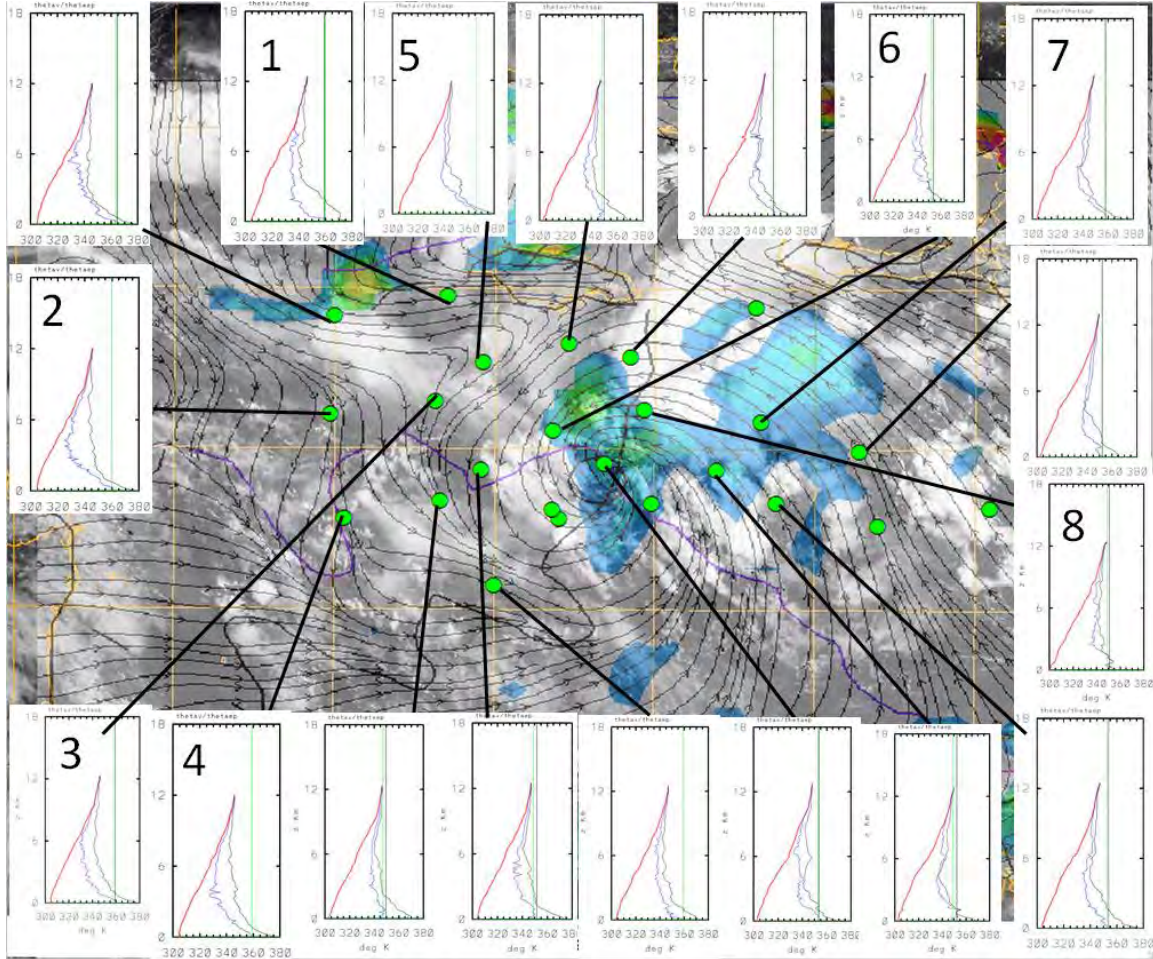
Figure 22.   Selected dropsonde profiles corresponding with dropsonde positions overlaid on the ECMWF 925 mb OW/co-moving streamline product and visible satellite image. Profiles derived from NSF GV dropsondes (original satellite image from Naval Research Laboratory-Monterey at http://www.nrlmry.navy.mil/TC/tc10/ATL; co-moving streamline images after Montgomery 2014a).

The equivalent potential temperature (θ_e) is indicated by the blue curves, the saturated equivalent potential temperature (θ_{es}) is indicated by the black curves, and the virtual potential temperature (θ_v) is indicated by the red curves.

47

The black and green vertical lines are the values of the equivalent potential temperature at the surface and 100 m from the surface. Following this vertical line with height gives a good approximation of raising a parcel with height moist adiabatically. The horizontal distance from the vertical line to the saturated equivalent potential temperature (θ_{es}) at a given height is approximately proportional to the buoyancy force per unit mass: a parcel is positively buoyant when its surface (or 100 m) equivalent potential temperature (θ_e) resides to the right of the saturated equivalent potential temperature curve (θ_{es}) (Smith and Montgomery 2012). The green dots are the locations of the dropsondes. The thick black lines throughout the image connect the vertical profiles with the dropsonde locations. The 925 mb ECMWF co-moving streamline, OW (color shaded) graphic is overlaid on top of a visible satellite image taken during the midway time of the research mission. The difference between saturation equivalent potential temperature (θ_{es}) and equivalent potential temperature (θ_e) at a given height is a relative measure for how dry the air is.

As the profile ascends with height, the amount of water vapor necessary to saturate the air will become less. This must be taken into account when comparing the difference of the two temperature measurements at for example one km and six km.

Figure 22 provides some evidence of dry air at the 925 mb level found below the 1.5 km height on the profiles entering the sweet spot from the west. Additionally, Figure 22 indicates the profiles on the western side of the system at mid to upper levels in the troposphere are relatively dry in comparison to the other profiles during this research flight. Specifically, profiles one through four indicates relatively dry air on the west side of the pouch, and profiles five through eight indicate moist profiles. Figure 21 shows strong northwesterly winds in the western vicinity in the middle to upper troposphere. However, it is uncertain of the consequences of the dry air near the surface on the western side of the pouch as the vapor flux coming from the ocean may moisten air parcels en route

to the inner region of the pouch. Additionally, the co-moving streamlines at this level do not appear to yield a direct path to the sweet spot for some of the dry air. Nevertheless, this observation combined with the possibility of dry air being transported into the system from aloft may have contributed to this system not developing as speculated from the mission scientist report for PGI27 (Davis 2010a).

The purpose of Figure 23 is to infer a broad picture of the thermodynamic characteristics of this pouch. It indicates a fairly dry mid and lower tropospheric pouch structure relative to the surface as measured by the difference between the smallest and largest value of the averaged θ_e . This difference $(\Delta\theta_e)$ is 22.9 K and 19.3 K from the surface to 5.4 km and 3.7 km for RF02 and RF03, respectively. Smith and Montgomery (2012) state that while it has previously been believed that "ensuing convection within a relatively dry, elevated layer of air would lead to comparatively strong downdraughts," there have been numerical modeling studies indicating "the principal effects of the dry air are to reduce the convective updraught strength and water loading, while the convective downdraught strengths are not changed appreciably." These studies were performed by James and Markowski (2009) and Kilroy and Smith (2012), and the results were found to be applicable on the convective scale.
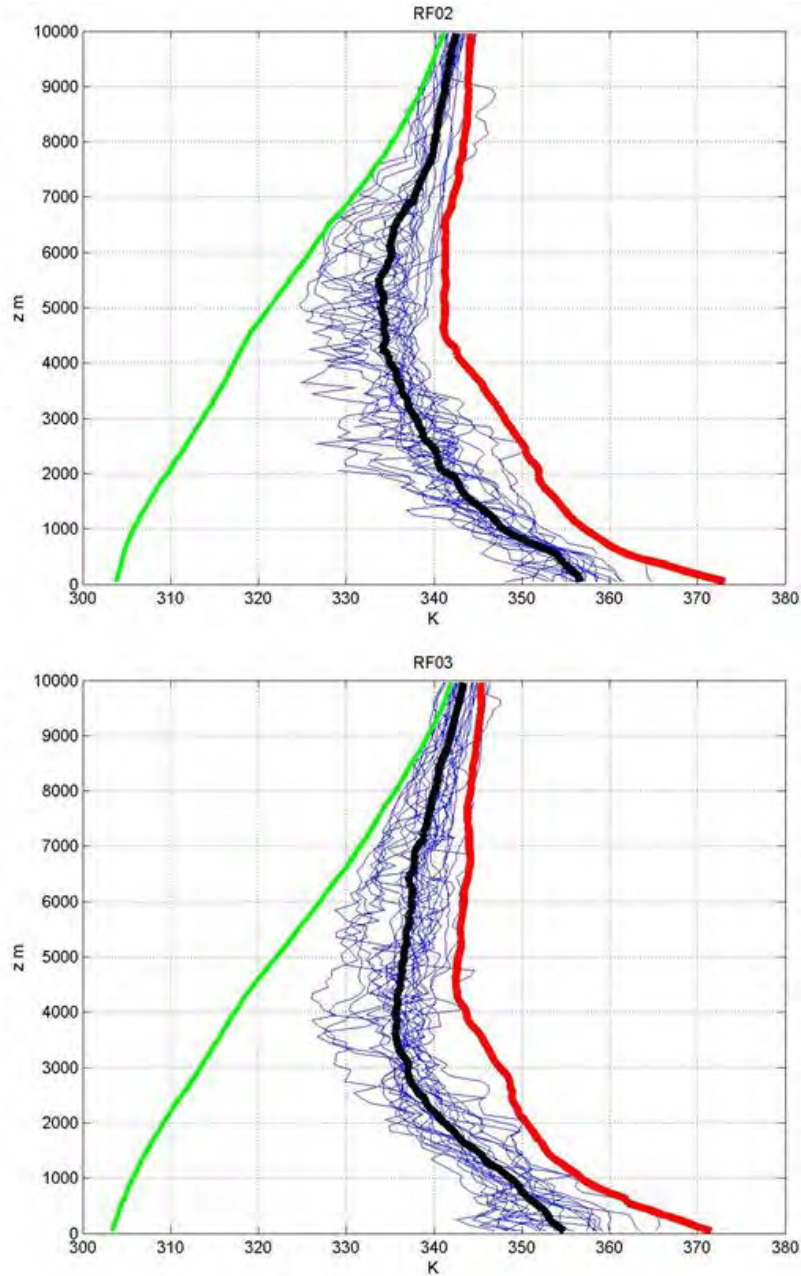
Figure 23.   Vertical profiles of the soundings displaying the values of θ_e, θ_{es}, and θ_v. The thin blue curves are all of the values of individual soundings for θ_e for RF02 (top) and RF03 (bottom). The black curve is the average θ_e value. The red curve is the average θ_{es} value for each research mission, and the green line is the average θ_v value for each research mission. Images derived from NSF GV dropsondes.

For a simulated updraught cycle, approximately one km in horizontal scale and one hour, the tangential wind increases due to vortex tube stretching effects. The increase of tangential wind tends to be approximately a couple of meters per second (Kilroy and Smith 2012). The consequence of a dry mid and lower tropospheric pouch structure relative to the surface acts to limit vorticity amplification on the convective scale due to reduced updraught strengths, which consequently would lead to less concentrated vorticity because the vortex-tube stretching would be weakened. A relatively large difference between θ_e at the surface and between 3 to 6 km above the surface indicates dry air (Smith and Montgomery 2012).

Smith and Montgomery (2012) found that developing disturbances Karl and Matthew had an area-averaged $\Delta\theta_e$ of approximately 17 K and non-developing disturbances had an area-averaged $\Delta\theta_e$ of approximately 24 K. PGI27's averaged $\Delta\theta_e$ difference of 22.9 K and 19.3 K for RF02 and RF03 is found to be in the middle of those two values. A favorable trend for development is that the area-averaged $\Delta\theta_e$ is declining from RF02 to RF03. Figure 24 further shows that as the area-averaged θ_e values are taken closer to the sweet spot, the $\Delta\theta_e$ has decreased even more (Wang 2012). Table 3 displays the relevant values for $\Delta\theta_e$.
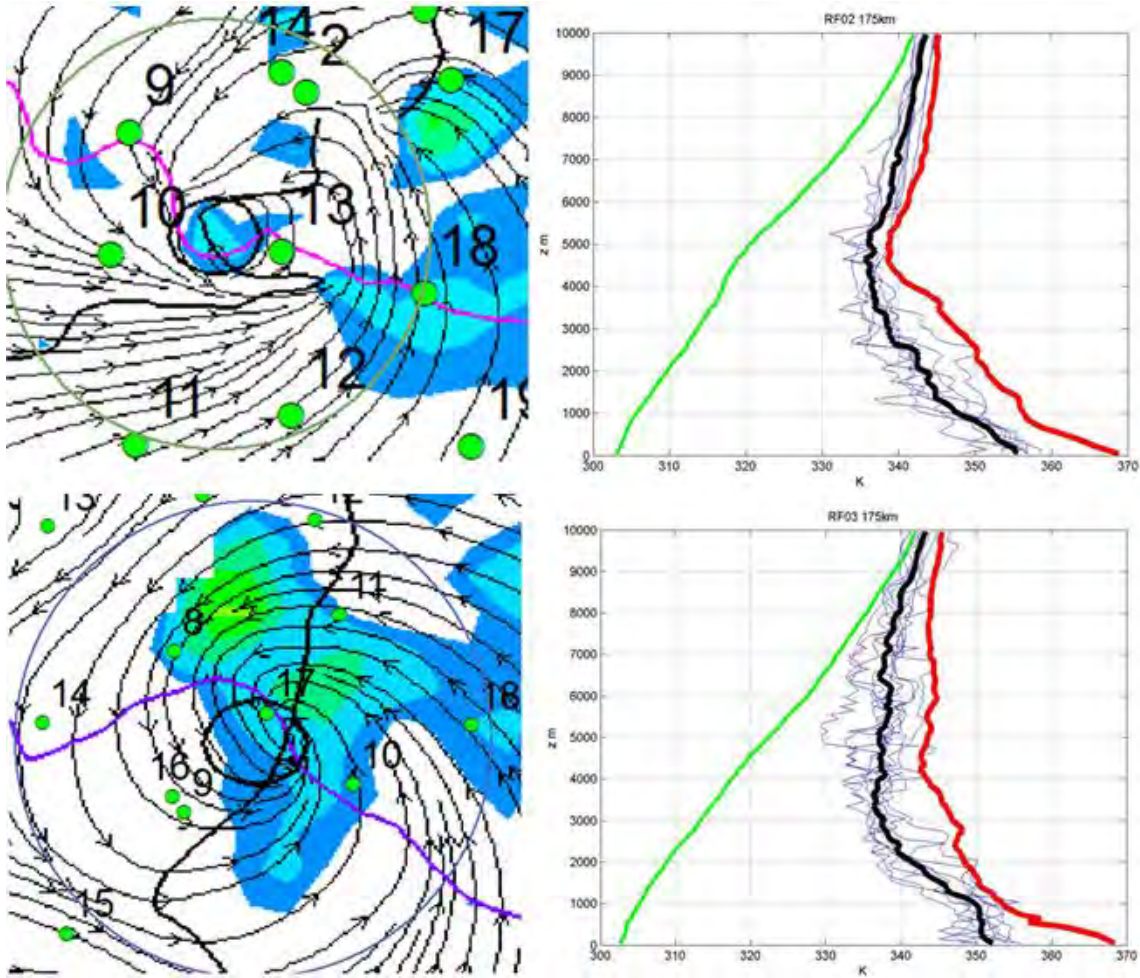
Figure 24.   Vertical profiles of the soundings from RF02 and RF03 displaying the values of θ_e, θ_{es}, and θ_v. This figure is similar to Figure 23 except it only incorporates the profiles that are within 175 km from the sweet spot (profiles derived from NSF GV dropsondes; co-moving streamline images after Montgomery 2014a).

RF	min Θe	min Z	max Θe	max Z	ΔΘe	ΔZ
2	333.7	5450	356.6	50	22.9	5400
2 (175 km)	335.5	4650	355.4	150	19.9	4500
3	335.5	3650	354.8	50	19.3	3600
3 (175 km)	336.3	3650	352.2	50	15.9	3600

Table 3.   Display of $\Delta\theta_e$ values for PGI27. Min θ_e, max θ_e, and $\Delta\theta_e$ are the minimum θ_e value, maximum θ_e value, and difference between the maximum value and minimum value for the area-averaged θ_e profile. The units are in Kelvin. Min Z and max Z correspond to the vertical profile height of min θ_e and max θ_e, respectively. ΔZ is the difference between min Z and max Z. The units are in meters. Table derived from NSF GV dropsondes.

Figure 25 depicts the vertical profile of the difference in θ_e and θ_v between RF03 and RF02. Positive values for the θ_e difference indicate moistening and negative values indicate drying. Positive values for the θ_v difference indicate warming and negative values indicate cooling. The vertical profile of the difference in area-averaged θ_e between the two days indicates alternating layers of weak moistening and drying throughout the column, yielding inconclusive results. Additionally, a more comprehensive analysis needs to be carried out on Figure 25 in order to isolate the θ_e signal from the noise. Therefore, the relationship between the decrease in $\Delta\theta_e$ and moistening is uncertain.
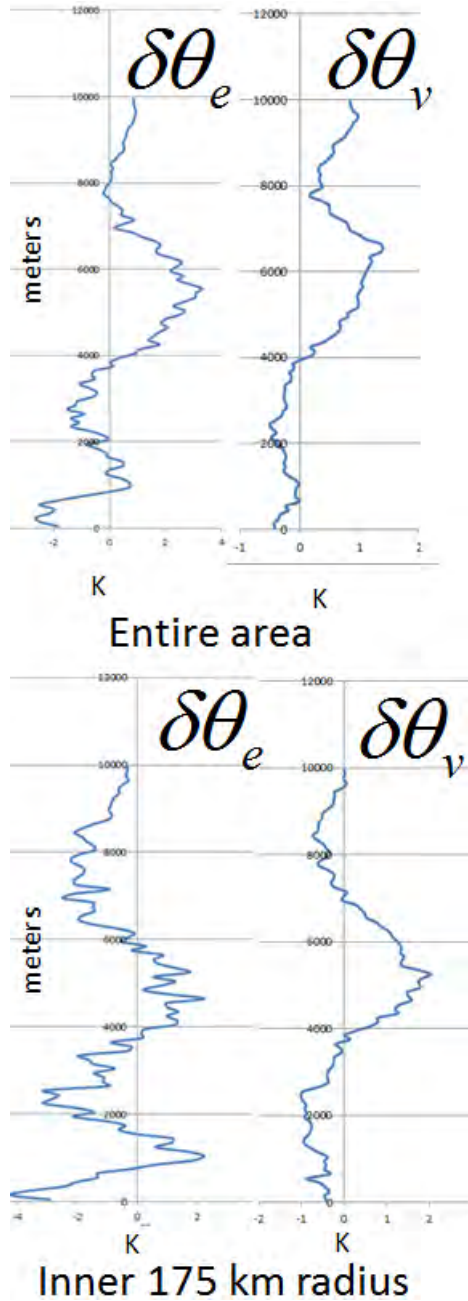
Figure 25. Vertical profiles of the difference of θ_e (left hand side) and θ_v (right hand side) in Kelvin defined as $\delta\theta_e$ and $\delta\theta_v$ between RF03 and RF02. Positive values for $\delta\theta_e$ indicate moistening and negative values indicate drying. Positive values for $\delta\theta_v$ indicate warming and negative values indicate cooling. Images derived from NSF GV dropsondes.

In summary, two of the three hypotheses (**H1** and **H2**) put forward by Dunkerton *et al*. (2009) are supported to some extent by the foregoing analysis. The favorable kinematic flow characteristics from 17 August to 18 August were as follows: The OW parameter increased by a factor of four close to the sweet spot. The area-averaged vorticity increased above the 900 mb level. The normalized area-averaged pouch vertical shear decreased. The disturbance became vertically aligned. Co-moving streamlines become more closed at the 925 mb level. The unfavorable kinematic flow characteristics were as follows: The normalized area-averaged deep vertical shear increased. Streamlines become less closed at the 700 mb level. The area averaged vorticity decreased below the 900 mb level.

Assuming the favorable kinematic flow characteristics outweigh the unfavorable flow characteristics, the marsupial paradigm would predict a gradual moistening of the pouch. Such a moistening is reflected to some extent in the decline of the area-averaged $\Delta\theta_e$. However, $\Delta\theta_e$ as a metric on its own comes with several sources of uncertainty: The area-averaged surface θ_e decreases from 17 August to 18 August. The vertical profile of the difference in area-averaged θ_e between the two days indicates alternating layers of weak moistening and drying throughout the column, yielding inconclusive results. Additionally, a more comprehensive analysis needs to be carried out on this profile in order to isolate the θ_e signal from the noise.

B.   PGI30

Figure 26 shows an analysis of the 700 mb GFS co-moving streamlines with the OW parameter displayed via color shading for August 21 and 23 for the disturbance identified as PGI30. The green dots identify the locations where dropsondes were released from the GV aircraft during the research flights on 21 and 23 August 2010 for RF04 and RF0, respectively (Montgomery 2014a).
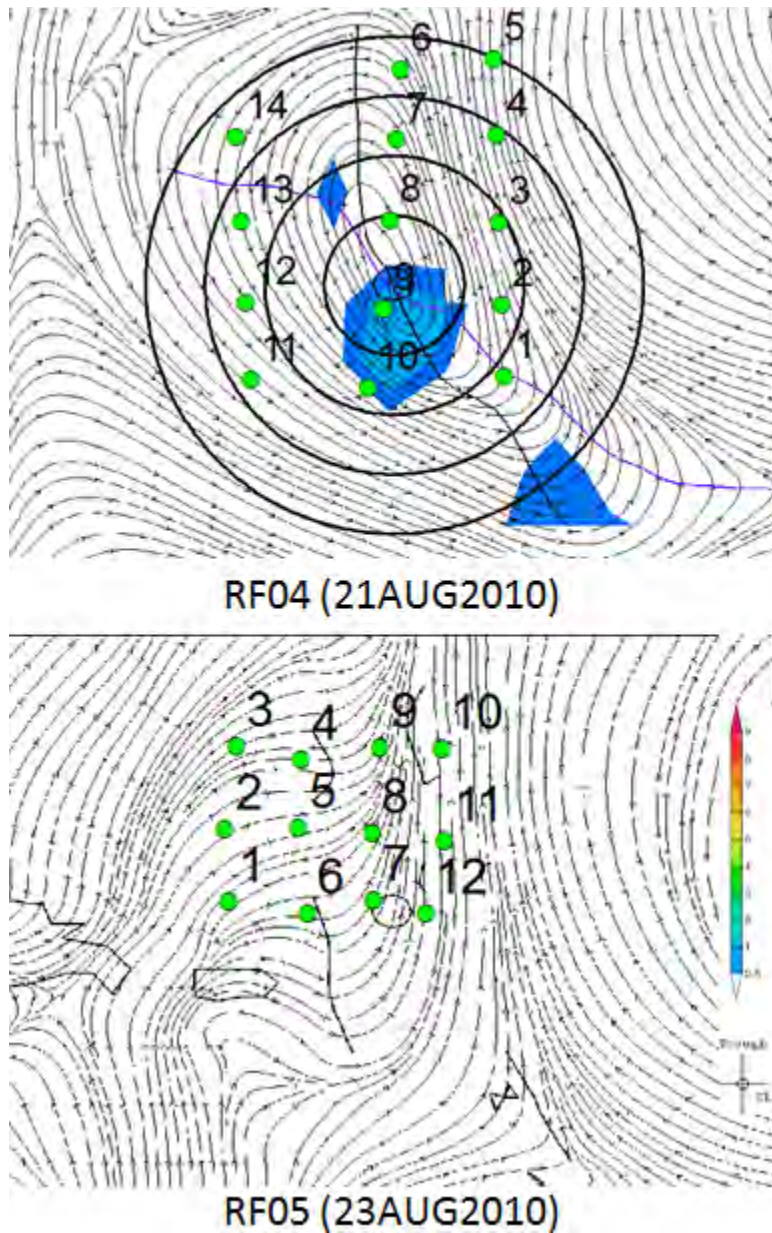
Figure 26.   As in Figure 12, except for 925 mb GFS co-moving streamline and Okubo-Weiss colored graphics of RF04 and RF05. RF04 is valid 2010082100 (12 hour tau). RF03 is valid 2010082212 (24 hour tau). Numbers indicate the chronological order of dropsondes (co-moving streamline images after Montgomery 2014a).

The co-moving streamlines in the 925 mb level for 21 August suggest a recirculating flow in the pouch region of the disturbance for that level. The largest concentration of the OW parameter is co-located with the sweet spot of the

pouch. On 23 August, neither the co-moving streamlines nor the OW parameter indicate that there is a recirculating flow or enough cyclonic vorticity to prevent the straining motions from deforming the favorable kinematic structure necessary for development. Given **H1**, this disturbance is an unlikely candidate for development as an organized cyclonic rotation and weak straining/shearing need to be present for a tropical disturbance to develop (Dunkerton et al. 2009).
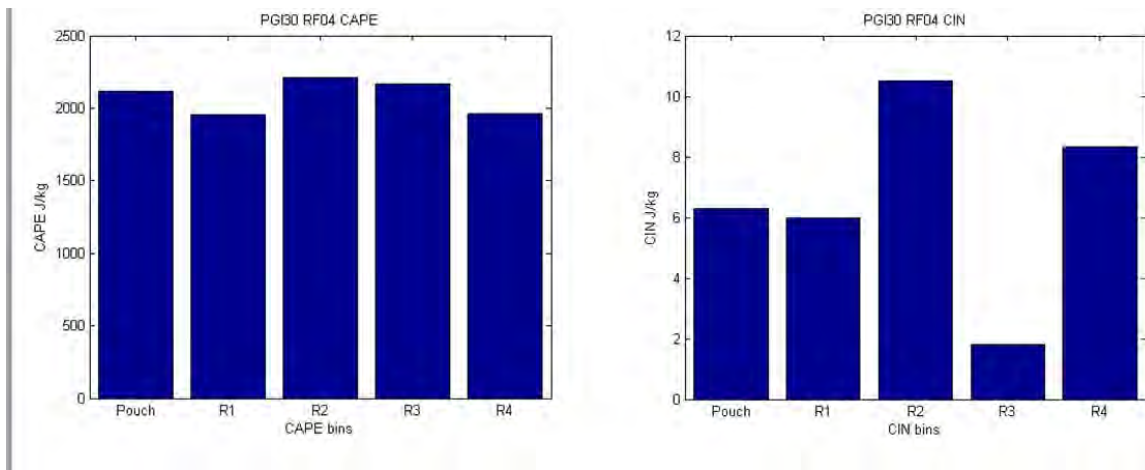
Figure 27.   CAPE and CIN for RF04 plotted according to the dropsondes distance from the sweet spot shown in Figure 26. All dropsonde distances are defined in the same way as in Figure 13. Images derived from NSF GV dropsondes.

Binning was not performed for RF05 as there was no apparent sweet spot or pouch. However, there is a sizable amount of observable CAPE and little CIN. The lowest CAPE value is greater than 2500 J/kg for RF05. The same convention of identifying which dropsondes had wind data and which dropsondes were without wind data from Table 2 is applied to Table 4.

RF04			RF05		
objectid	CAPE	CIN	objectid	CAPE	CIN
1	1973	4	1	2536	7
2	1906	15	2	2518	7
3	2373	5	3	2623	12
4	2583	0	4	2990	7
5	2336	4	5	3530	2
6	2061	4	6	2938	15
7	2437	2	7	3296	6
8	2763	0	8	3047	4
9	1957	6	9	3043	5
10	1814	22	10	3531	1
11	2094	1 N	11	2938	23
12	1753	2	12	3077	29
13	N	N			
14	1491	17			
15	N	N			
16	N	N			

Table 4.   RF04 and RF05 CAPE and CIN values corresponding to the object-id numbers found in Figure 26. Object-ids 15 and 16 were not shown in Figure 26 for RF04 as they had no useable data. See Table 2 for a description of W and N. Table derived from NSF GV dropsondes.

PGI30 was a clear nonstarter for developing into a tropical storm. Interestingly, the CAPE in RF04 and RF05 is higher than any of the other research flights in this thesis, with an average value of 2119 J/kg and 3006 J/kg, respectively. Furthermore, the CIN is lower than any of the other research flights found in this thesis, with an average value of 6 J/kg and 10 J/kg for RF04 and RF05, respectively. Again, a possible explanation for this was offered by Dunkerton (2014, personal communication), as this may reflect the tendency for convection to preferentially consume CAPE near the sweet spot, which according

to the marsupial paradigm, is the most favorable place for deep convection, vortex tube stretching, and vorticity concentration. However, if CAPE is not consumed, it stands to reason that CAPE could increase over time. The pouch-averaged CAPE and CIN for the developing and non-developing pouches from the PREDICT experiment as discussed by Komaromi (2010) is typically in the range of 2000 J/kg and under 50 J/kg, respectively. PGI30 demonstrates that thermodynamic quantities such as CAPE and CIN are just one of many parameters that need to be observed when determining if a disturbance is a candidate to develop into a tropical storm.

Figure 28 shows a kinematically unfavorable disturbance for development. For RF04, the local circulation centers locations are approximately 630 km apart between the 925 mb and 700 mb levels. Additionally, the positive OW values only exist at the 925 mb level. Figure 29 depicts the vertical profile of area-averaged vorticity for the circulation displayed in Figure 28. Figure 29 shows shallow cyclonic circulation, extending only from the surface to 700 mb. The circulation is anti-cyclonic from 500 mb to 200 mb. The co-moving streamlines and OW parameter in Figure 28 echo the vertical profile of area-averaged vorticity. The 925 mb co-moving streamlines indicate a recirculating flow in the pouch region with weakly concentrated OW values near the 700 mb sweet spot location. The 700 mb co-moving streamlines and OW parameter do not indicate any form of circulation around the circulation path shown in Figure 28, which is reflected also in Figure 29. The 700 mb level appears disorganized in its kinematic flow structure around the circulation path chosen. This is most likely why the vorticity at the 700 mb level in Figure 29 is zero.
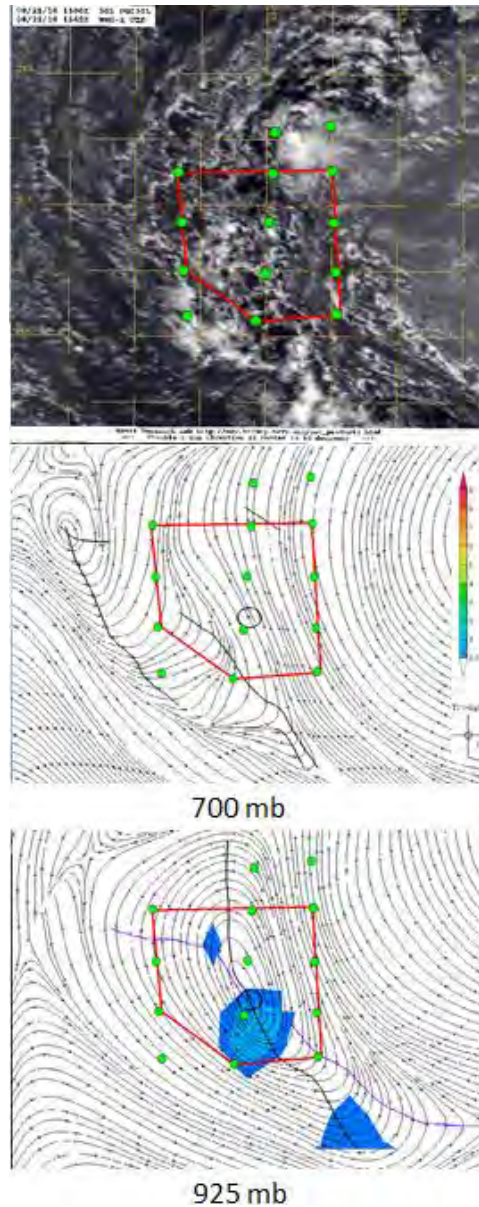
700 mb

925 mb

Figure 28. Circulation path chosen for RF04 depicted on a visible satellite image and 700 mb and 925 mb GFS co-moving streamlines and Okubo-Weiss image in color valid at 2010082100 (12 hour tau). See methodology for the calculation of OW values (magnitude and units: $10^{-9} s^{-2}$). The trough and CL are represented by a black and purple line, respectively. A circle is drawn over the point of intersection between the tough and CL at 925 mb to represent the sweet spot (original satellite image from Naval Research Laboratory-Monterey at http://www.nrlmry.navy.mil/TC/tc10/ATL; co-moving streamline images after Montgomery 2014a).
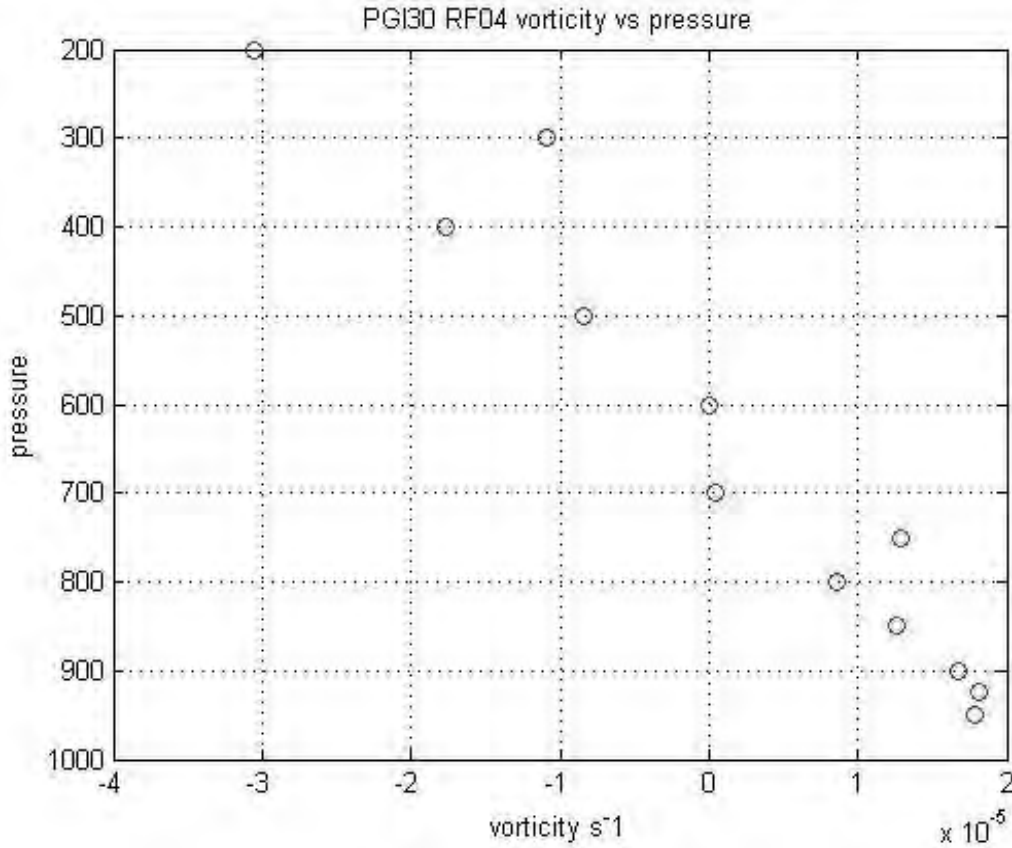
Figure 29.   Vertical profile of area-averaged vorticity for Research Flight 04 (in PGI30) for the path shown in Figure 28. Vorticity is plotted in units of $10^{-5}s^{-1}$. Image derived from NSF GV dropsondes.

The co-moving streamlines and the OW parameter at the 925 mb and 700 mb levels for RF05 show no indication of cyclonically recirculating flow for PGI30 (Figure 30). Figure 31 depicts the vertical area-averaged vorticity with height for the circulation displayed in Figure 30. The cyclonic circulation of 23 August is shallower than that found on 21 August. RF05 becomes anticyclonic between the 800 mb and 750 mb level. The dominant circulation in Figure 30 is a large anticyclonic circulation found to the east of what was the PGI30 disturbance. The flow kinematics does not support the development of this disturbance due to lack of a kinematic boundary as **H1** would suggest (Dunk*erton et al. 2009).*
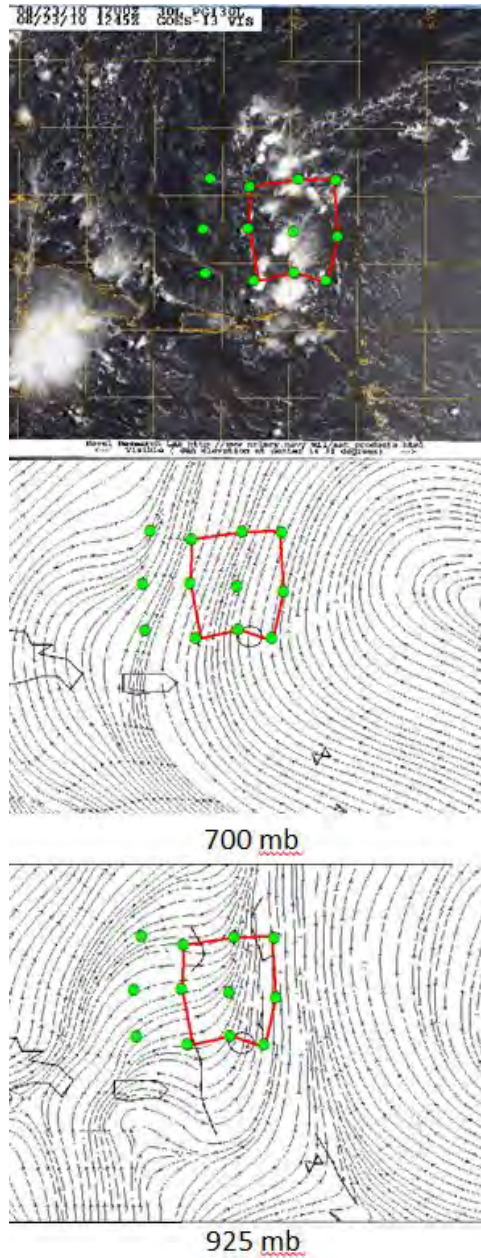
Figure 30.   Circulation path chosen for RF05 depicted on a visible satellite image and 700 mb and 925 mb GFS co-moving streamlines and Okubo-Weiss image in color valid at 2010082212 (24 hour tau). There is no trough, CL, or sweet spot (original satellite image from Naval Research Laboratory-Monterey at http://www.nrlmry.navy.mil/TC/tc10/ATL; co-moving streamline images after Montgomery 2014a).
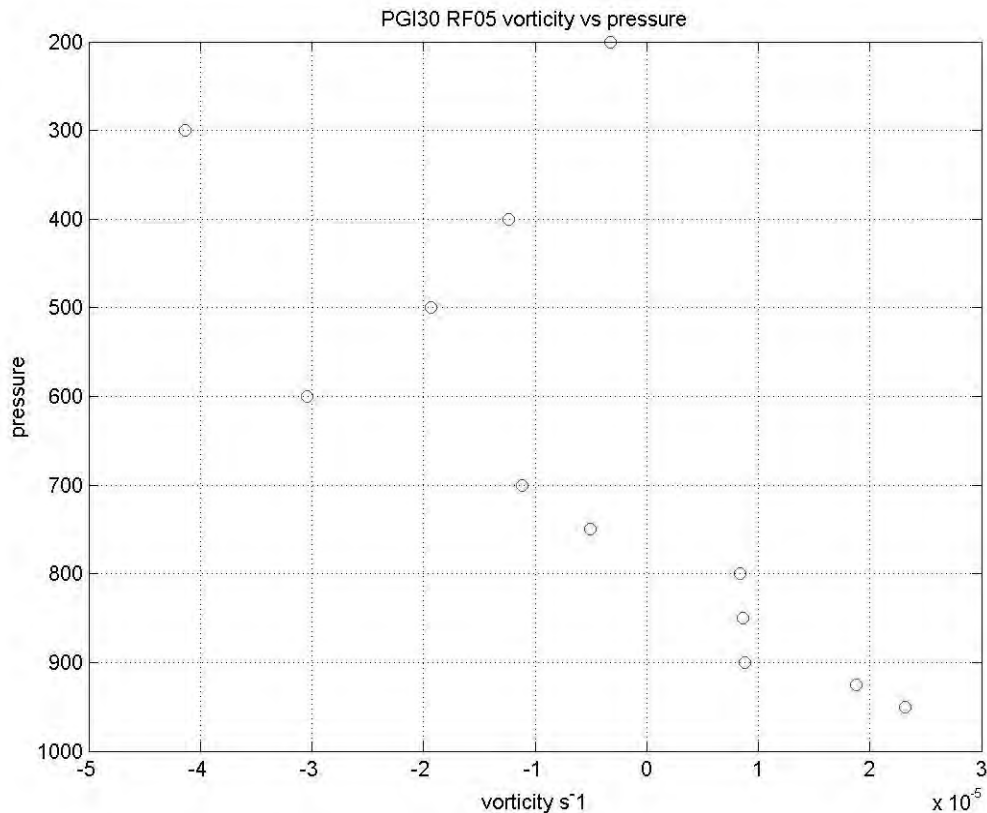
Figure 31. Vertical profile of area-averaged vorticity for Research Flight 05 (in PGI30) for the path shown in Figure 30. Vorticity is plotted in units of $10^{-5} s^{-1}$. Image derived from NSF GV dropsondes.

Figure 32 shows the magnitude of shear at each location of the dropsondes deployed for the two research missions of PGI30. Figure 33 quickly conveys a sense of the amount of vertical shear in the area of PGI30's pouch by calculating the areal-averaged value of shear in the pouch. Figure 33 indicates the presence of low area-averaged vertical shear. Additionally, the 925 mb and 500 mb dropsonde co-moving winds and 700 mb streamline image for RF04 do not perfectly line up, but the presence of a large vertical shear is not evident. However, the area-averaged vertical shear for RF05 is slightly misleading. The values of the area-averaged vertical shear in RF05 are comparable to RF04. However, a closer inspection of the individual dropsonde co-moving winds found in Figure 32 indicate weak values in magnitude, but in many cases the 925 mb

63

co-moving winds and the 500 mb co-moving winds are blowing in different directions between 90 to 180 degrees. It is the weak magnitude of the winds themselves that is masking how different the flow structure is between those two levels. A normalized value of the area-averaged vertical shear is not appropriate given how shallow the cyclonic circulation of this disturbance is. The area-averaged tangential winds are zero at the 700 mb level for RF04 and then become negative with height. The 700 mb level area-averaged tangential velocity value is already negative at the 700 mb level for RF05. These results agree well with the previous kinematic flow discussion for PGI30 in which the kinematic flow structure does not provide a sufficiently protective boundary throughout the vertical column of the disturbance to allow deep convection to occur as is required for development given **H2** (Dunkerton *et al*. 2009). Dry air intrusion will occur in the lower troposphere close to the already weak proto-vortex. This dry air will act to limit the amplification of vorticity throughout the vertical column of the disturbance via vortex tube stretching (Smith and Montgomery 2012).
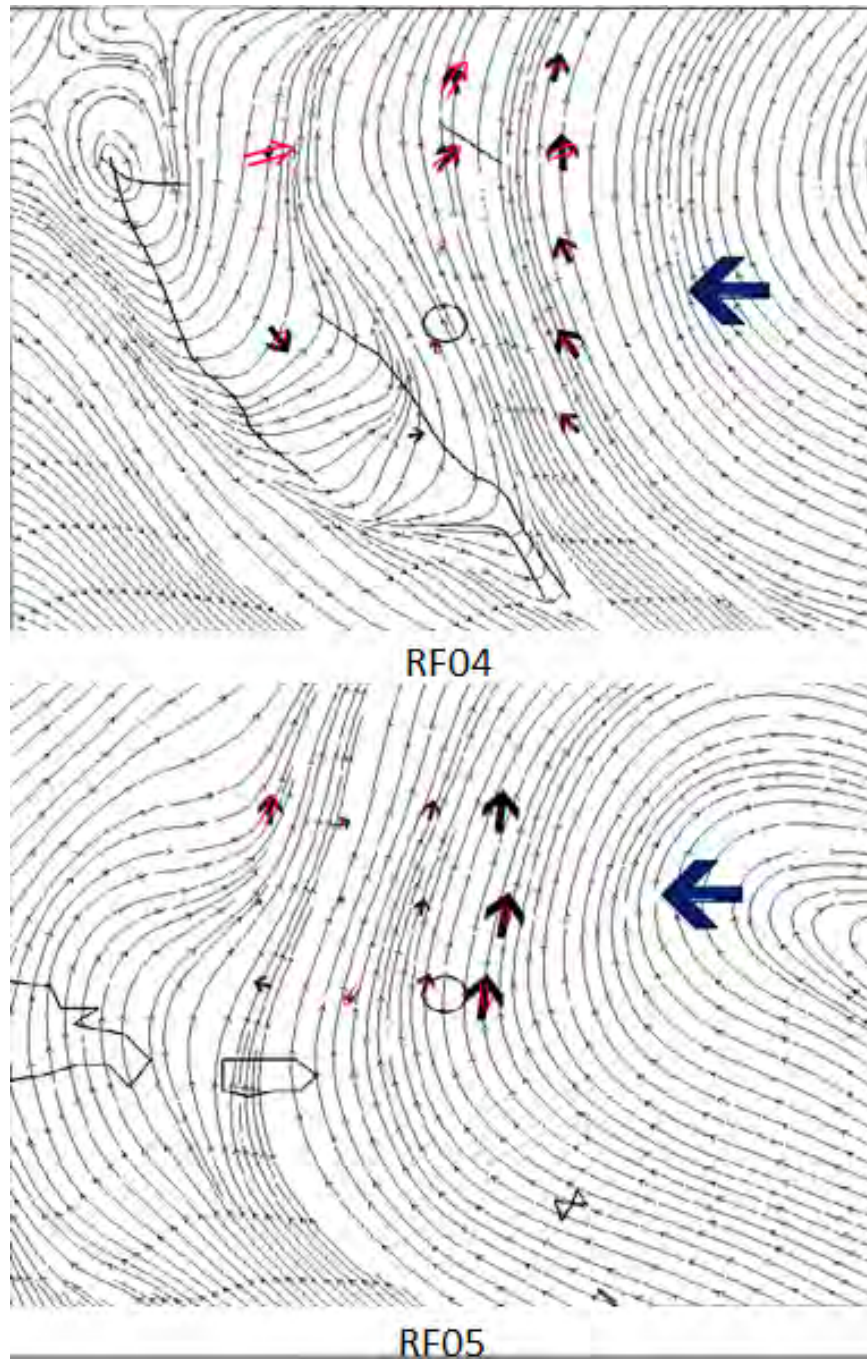
Figure 32. Vertical shear spatially represented by the 925 mb co-moving winds (black arrow), 500 mb co-moving winds (red arrow) from NSF GV dropsondes, and 700 mb GFS co-moving streamline background for RF04 and RF05. All vectors are scaled to the same magnitude. The blue vector represents $10\,m \cdot s^{-1}$ winds (co-moving streamline images after Montgomery 2014a).
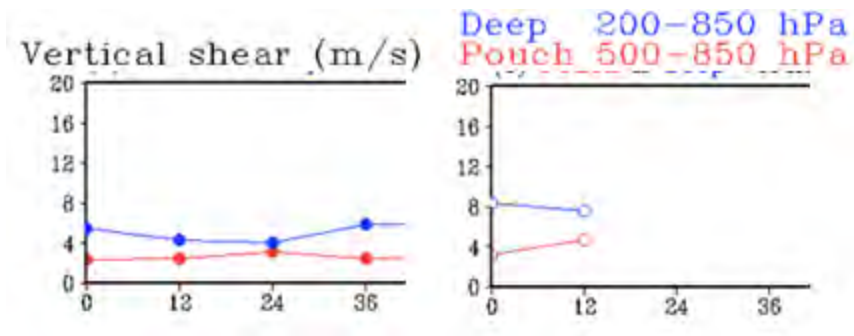
Figure 33.   Vertical shear averaged over the three by three-degree area of the pouch for RF04 (left) and RF05 (right) using ECMWF model results using ECMWF model results. The valid forecast times are 2010082100 and 2010082300 from left to right, respectively (from Montgomery 2014a).

Similar to Figure 22, Figure 34 summarizes the equivalent potential temperatures, saturated equivalent potential temperatures, and virtual potential temperatures profiles throughout RF04.
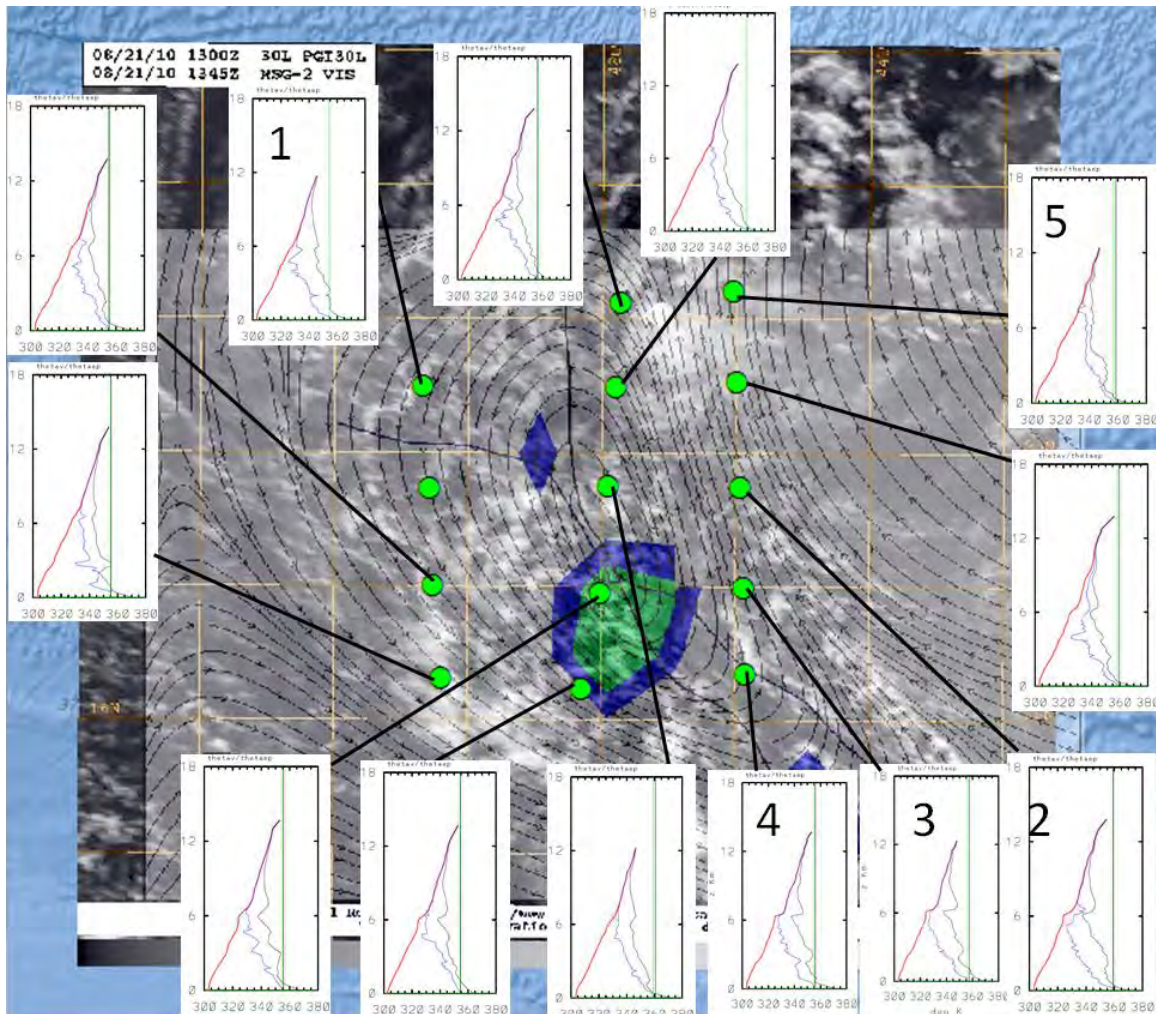
Figure 34.   Selected dropsonde profiles corresponding to dropsonde positions overlaid on the ECMWF 925 mb streamline product and visible satellite image. Profiles derived from NSF GV dropsondes (co-moving streamline images after Montgomery 2014a).

Figure 34 provides evidence of dry air at all levels surrounding the center of RF04. The majority of the profiles seen in Figure 34 are relatively dry. There is evidence this disturbance did not develop because of the presence of dry air. However, by studying Figure 34 independently it is not conclusive why PGI30 did not develop. A statistical analysis will be performed on these profiles augmenting this observation. Profiles one through four indicate dry profiles and profile five indicates a moist profile.

As mentioned previously, the purpose of Figure 35 is to infer a broad picture of the thermodynamic characteristics of this pouch. Table 5 displays the relevant $\Delta\theta_e$ values for PGI30.
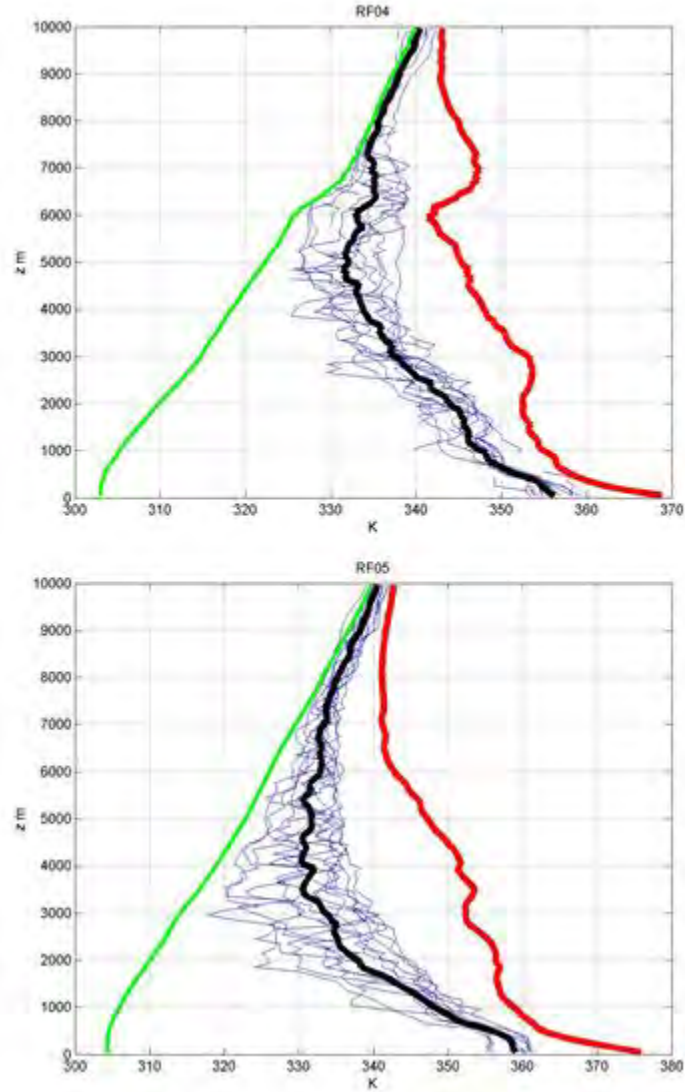
Figure 35.   Vertical profiles of the soundings displaying the values of θ_e, θ_{es}, and θ_v. Curves are defined in Figure 23. Images derived from NSF GV dropsondes.

RF	min Θe	min Z	max Θe	max Z	ΔΘe	ΔZ
4	331.4	4850	356.2	50	24.8	4800
5	330.4	4050	359	50	28.7	4000

Table 5.   Display of $\Delta\theta_e$ values for PGI30. Values are defined in Table 3. Table derived from NSF GV dropsondes.

For PGI30, Figure 35 indicates a dry mid- and lower-tropospheric pouch structure relative to the surface due to the difference between the smallest and largest value of the averaged θ_e which is 24.8 K and 29 K from the surface to 4.9 km and 4.1 km for RF04 and RF05, respectively. The $\Delta\theta_e$ values for PGI30 are even higher than those found in the non-developer "ex-Gaston (PGI38)" analyzed in Smith and Montgomery (2012). Given **H2**, the high $\Delta\theta_e$ values for PGI30 reaffirms that it is highly unlikely that PGI30 will develop on account of the lack of a kinematic boundary that prevents dry air intrusion and allows repeated moistening of the sweet spot by convection (Dunkerton *et al*. 2009).

C.   PGI36 (FIONA)

Figure 36 for PGI36 is presented in the same format as Figure 12 for PGI27 and Figure 23 for PGI30. As previously mentioned in the introduction, PGI36 was upgraded to a tropical storm after the first research flight for this system was conducted. Therefore, the system is more organized in several respects compared to the disturbances previously analyzed in this paper. It is apparent in Figure 36 that the co-moving streamlines show strong cyclonic circulation; and a high OW values is concentrated in the center of the pouch around the sweet spot as well as high OW values located as patches along the co-moving streamlines, particularly in the case of RF07. From a kinematic viewpoint, the 700 mb ECMWF streamline and OW analysis would indicate that PGI36 has indeed developed into a tropical storm.
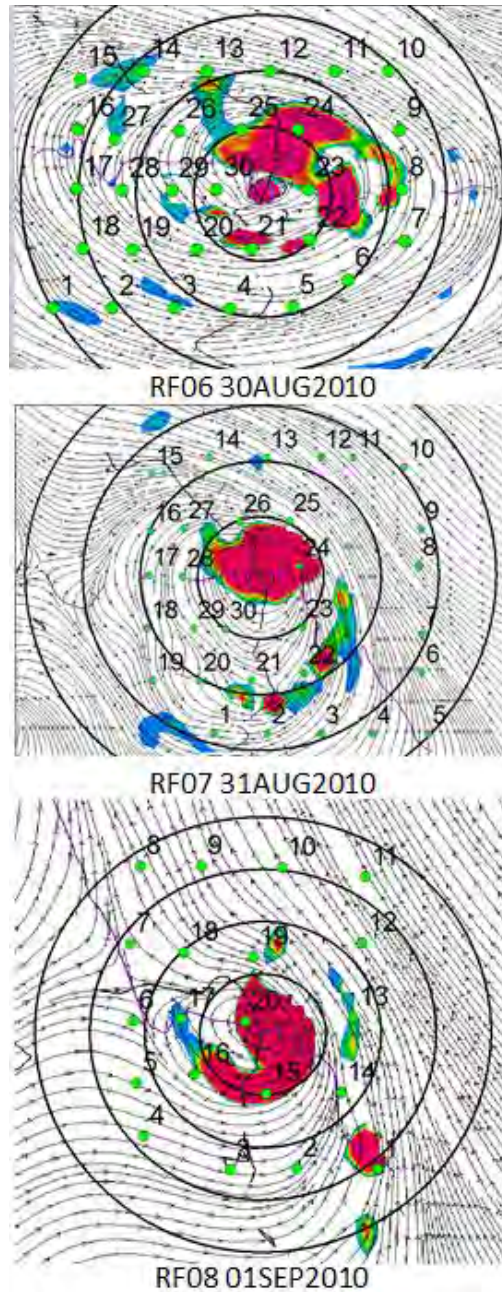
Figure 36.   700 mb ECMWF co-moving streamline and Okubo-Weiss graphics of RF06, RF07, and RF08 valid 2010083012 (0 hour tau), 2010083112 (0 hour tau), and 2010090112 (0 hour tau). The numbers correspond with the object-id assignments of the dropsondes assigned in chronological order. Table 6 shows the CAPE and CIN values for RF06, RF07, and RF08 with respect to each object-id. Data derived from NSF GV dropsondes (co-moving streamline images after Montgomery 2014a).

Table 6 displays the CAPE and CIN values corresponding to the object-ids found in Figure 36.

	RF06			RF07			RF08	
objectid	CAPE	CIN	objectid	CAPE	CIN	objectid	CAPE	CIN
1	2795	0	1	1379	18	1	1443	13
2	2442	2	2	1404	13	2	1920	55
3	1337	17	3	3071	0	3	2763	0
4	1018	29	4	1359	32	4	2137	13
5	1130	19	5	2152	12	5	1626	24
6	1896	0	6	934	64	6	1736	14
7	2322	4	7	2298	5	7	4102	0
8	939	23	8	1674	32	8	1533	35
9	1734	32	9	1915	15	9	1999	29
10	2054	11	10	2363	20	10	3430	1
11	2941	0	11	2430	20	11	2644	17
12	1395	36	12	2190	19	12	2444	18
13	1880	7	13	1690	61	13	1860	19
14	1836	17	14	2496	15	14	891	126
15	1368	44	15	2903	5	15	1734	13
16	1623	5	16	3364	2	16	552	15
17	1613	3	17	2880	1	17	129	47
18	1121	32	18	1353	30	18	588	28
19	1341	4	19	3052	3	19	441	103
20	869	6	20	2313	7	20	340	0
21	558	31	21	1546	15	21	330	0
22	2123	0	22	1819	13			
23	850	12	23	1687	15			
24	2290	0	24	1852	27			
25	338	29	25	1653	54			
26	1227	20	26	1955	54			
27	2958	0	27	1506	32			
28	983	28	28	1527	101			
29	599	33	29	2489	0			
30	1308	2	30	1769	34			

Table 6.   RF06, RF07, and RF08 CAPE and CIN values corresponding to the object-id numbers found in Figure 36. No kinematic or thermodynamic data was missing from any dropsondes. Table derived from NSF GV dropsondes.

As seen in Figure 37, the average CAPE value found for all dropsondes released in PGI36 were 1563 J/kg, 2034 J/kg, and 1650 J/kg for RF06, RF07, and RF08, respectively and the average CIN values were found to be 15 J/kg, 24 J/kg, and 27 J/kg for RF06, RF07, and RF08, respectively.
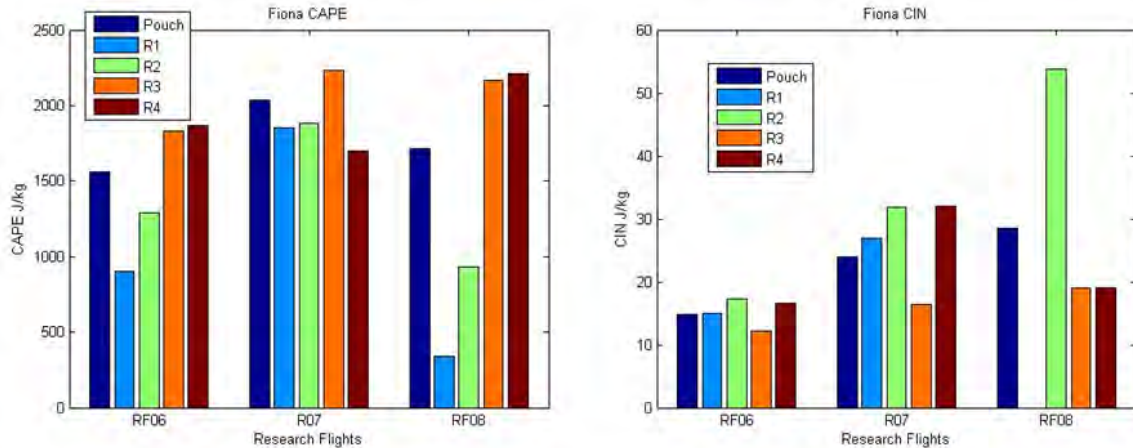
Figure 37.   CAPE and CIN for RF06, RF07, and RF08 plotted according to the dropsondes distance from the sweet spot. Refer to Figure 13 for explanation of graphic. Images derived from NSF GV dropsondes.

The kinematic flow structure will be analyzed applying the same approach as was done in PGI27 and PGI30. However, jumping ahead to a comparison of the area-averaged vorticity with height for the three research flights in Figure 38 yields an interesting relationship with Figure 37. Figure 38 is a vertical comparison of the amount of vorticity found from the inner and outer circulation paths chosen for the three research flights that will be discussed later in this section for PGI36. Of note is the inner circulation path for PGI36 at and below 500 mb. The vorticity at those levels slightly increases from RF06 to RF07 and then increases significantly from RF07 to RF08. Focusing the reader's attention back to Figure 37 indicates a CAPE increase in the inner three bins from 30 August (RF06) to 31 August (RF07) and a CAPE decrease in the inner three bins from 31 August (RF07) to 01 September (RF08). An explanation that has been brought up in the previous two depressions that still seems applicable for this tropical storm is from Dunkerton (2014, personal communication): This may reflect the tendency for convection to be preferentially consuming CAPE near the sweet spot, which according to the marsupial paradigm, is the most favorable place for deep convection, vortex tube stretching, and vorticity concentration. This explanation may explain also why two of the three averaged CAPE values of

the research missions for PGI36 were 300 J/kg to 400 J/kg below the average CAPE value of all the PREDICT experiments found to be in the range of 2000 J/kg (Komaromi 2010) as CAPE may have already been preferentially consumed to build PGI36 into a tropical storm.
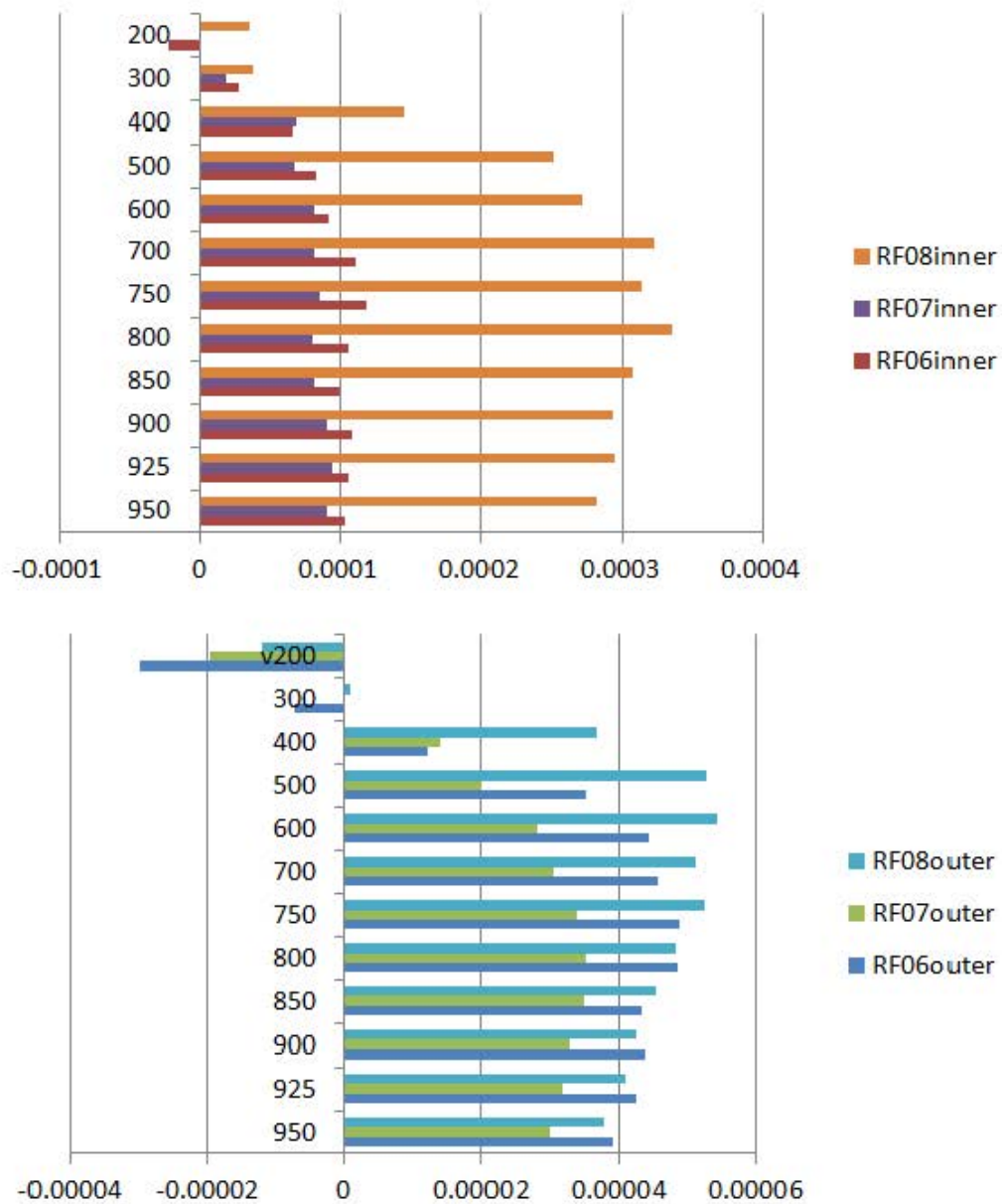
Figure 38.   Comparison of the area-averaged vorticity for RF06, RF07, and RF08's previously chosen inner and outer circulation paths. Images derived from NSF GV dropsondes.

The co-moving streamlines in Figure 39 indicate that the vertical profile of Fiona is vertically stacked. The high OW values near the sweet spot of RF06 indicate that vorticity is significantly greater than the normal and parallel strain leading to the conclusion that from a kinematic standpoint, the pouch center is favorable for development. Figure 40 which depicts the area-averaged vorticity at various heights of the inner and outer loop of Figure 39, coincides very well with the co-moving streamlines and OW parameter found in Figure 39. Both figures indicate that this tropical storm's profile is vertically stacked throughout the entire troposphere as the sweet spot and co-moving streamlines in Figure 39 are horizontally in the same location as well as the presence of the typical bow shape of a tropical storm's area-averaged vertical vorticity profile (Montgomery *et al*. 2012). The kinematic flow structure follows a typical tropical cyclone with the strongest cyclonic circulation located in the lower troposphere where the inner and outer circulations both have their strongest cyclonic values between the 800 mb and 700 mb level. The cyclonic circulation gradually weakens above those levels until the outer circulation is anticyclonic between 400 mb and 300 mb and the inner circulation is anticyclonic at 300 mb. Additionally, as expected the inner cyclonic vorticity is over twice as strong as the outer cyclonic vorticity.

Figure 39. Inner and outer circulation paths chosen for RF06 depicted on a visible satellite image and 700 mb and 925 mb ECMWF co-moving streamlines and Okubo-Weiss image in color valid at 2010083012 (0 hour tau). Refer to Figure 14 for further explanation of graphic (original satellite image from Naval Research Laboratory-Monterey at http://www.nrlmry.navy.mil/TC/tc10/ATL; co-moving streamline images after Montgomery 2014a).

75

Figure 40.   Vertical profile of area-averaged vorticity for Research Flight 06 (in PGI36) for the paths shown in Figure 39. Vorticity plotted in units of $10^{-5} s^{-1}$. The inner and outer circulation paths in Figure 39 are plotted using blue diamonds and red circles, respectively. Image derived from NSF GV dropsondes.

Figure 41 shows that there is still strong cyclonic flow in PGI36. The system still appears vertically stacked, the co-moving streamlines are organized in cyclonic flow, and the strongest concentration of the OW parameter is near the sweet spot for both the 925 mb and 700 mb level with the addition of a moderately strong band of OW values across the southeast of the sweet spot. Figure 42 indicates the outer circulation center (strongest vorticity value) has appeared to shift downward to the 800 mb level, and the inner circulation center has appeared to shift downward to the 950 mb level. Overall, the values for vorticity have decreased from RF06 for every level beneath 500 mb. Additionally, the inner circulation path is cyclonic throughout the entire profile while the outer circulation path is anticyclonic between 300 mb and 200 mb.

Figure 41.   Inner and outer circulation paths chosen for RF07 depicted on a visible satellite image and 700 mb and 925 mb ECMWF co-moving streamlines and Okubo-Weiss image in color valid at 2010083112 (0 hour tau). Refer to Figure 14 for further explanation of graphic (original satellite image from Naval Research Laboratory-Monterey at http://www.nrlmry.navy.mil/TC/tc10/ATL; co-moving streamline images after Montgomery 2014a).

Figure 42. Vertical profile of area-averaged vorticity for Research Flight 07 (in PGI36) for the paths shown in Figure 41. Vorticity plotted in units of $10^{-5} s^{-1}$. The inner and outer circulation paths for RF07 are depicted as blue diamonds and red circles, respectively. Image derived from NSF GV dropsondes.

Figure 43 indicates the magnitude of positive vorticity found in RF08 is between one to three times as large as the magnitude of positive vorticity found in RF06 or RF07. RF08's inner circulation center has shifted vertically up to approximately the 800 mb level, and the circulation is cyclonic throughout the entire vertical column. The outer circulation, however, is anticyclonic at the 200 mb level. Figure 44 indicates the outer circulation kinematic flow structure is the most vertically aligned out of all research flights as the area-averaged vorticity values throughout the vertical column have approximately the same value at and below the 500 mb level, and a high OW value is centered over the sweet spot for both the 925 mb and 700 mb level. Additionally, a hyperbolic stagnation point in the co-moving frame of reference can be observed on the northwest side of the sweet spot for both the 925 mb and 700 mb level, indicating the kinematic flow structure is the most closed of the three research flights (Rutherford and Montgomery 2012).
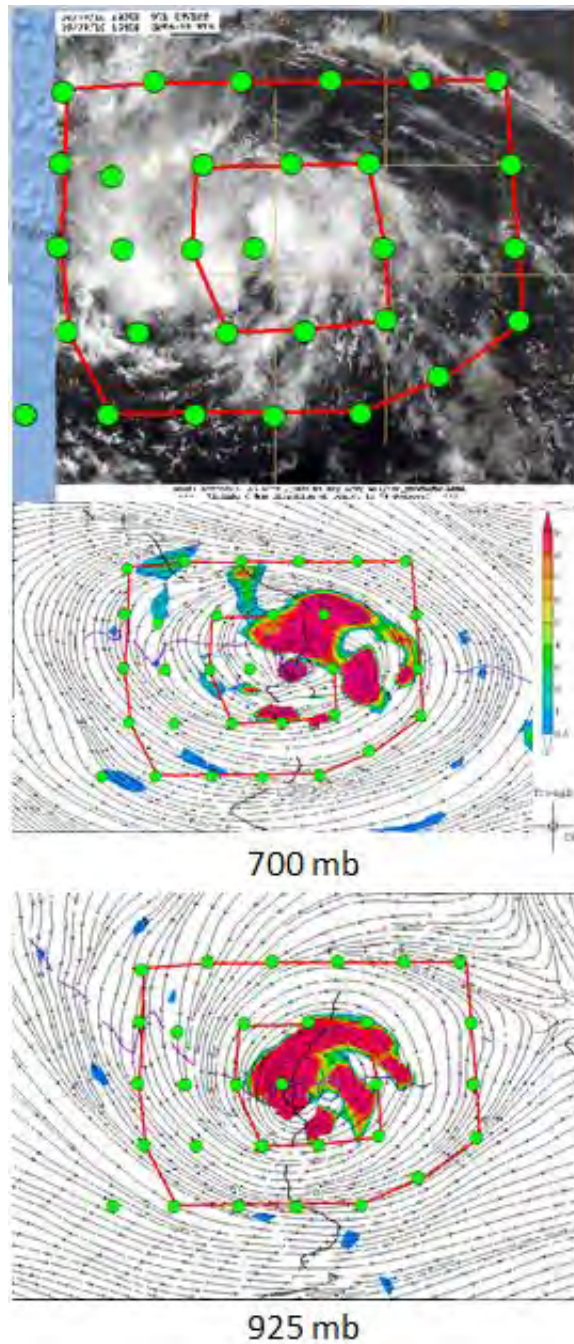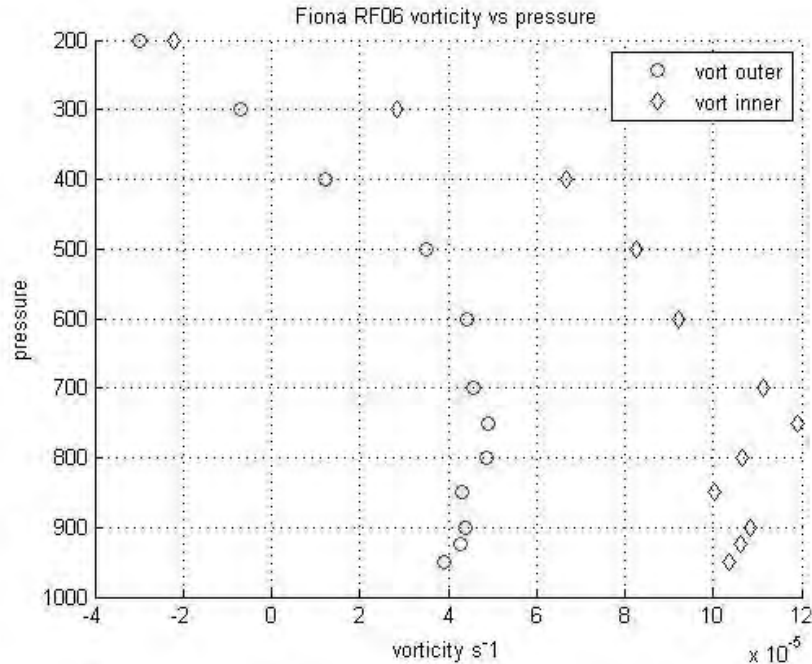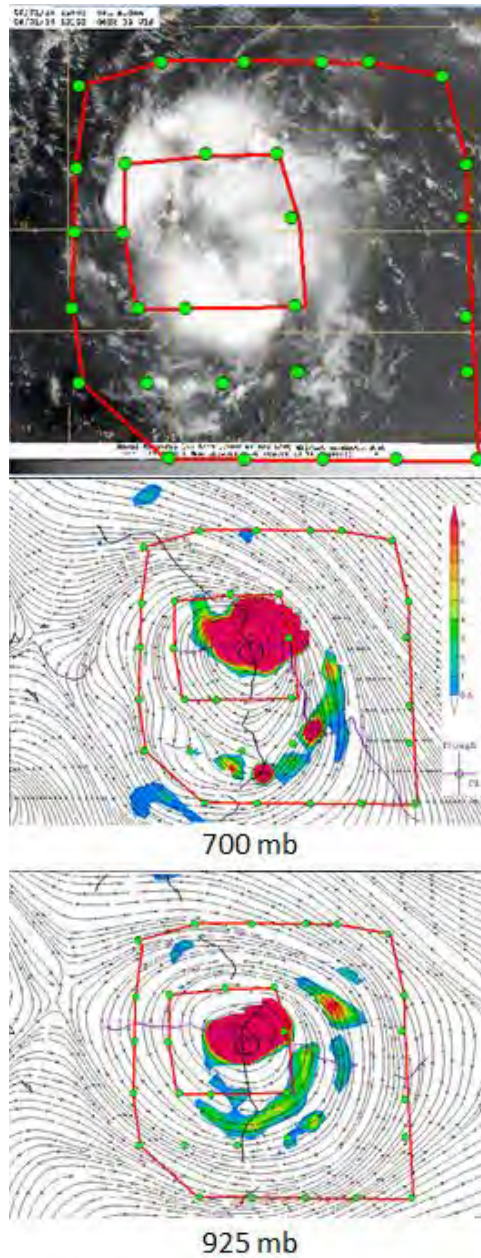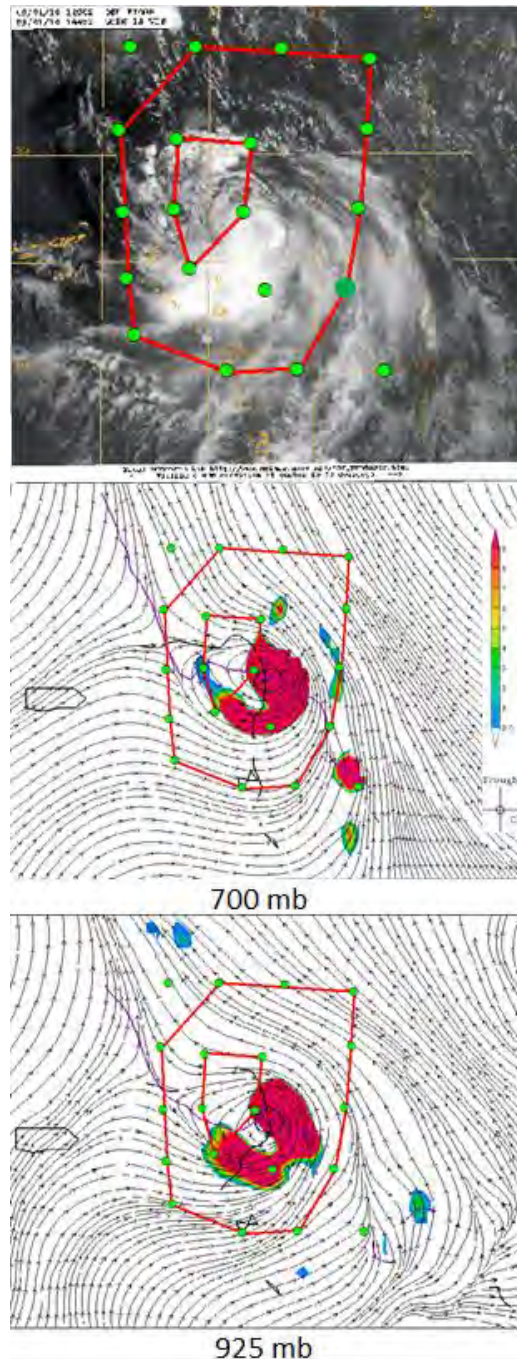
Figure 43. Inner and outer circulation paths chosen for RF08 depicted on a visible satellite image and 700 mb and 925 mb ECMWF co-moving streamlines and Okubo-Weiss image in color valid at 2010090112 (0 hour tau) (original satellite image from Naval Research Laboratory-Monterey at http://www.nrlmry.navy.mil/TC/tc10/ATL; co-moving streamline images after Montgomery 2014a).
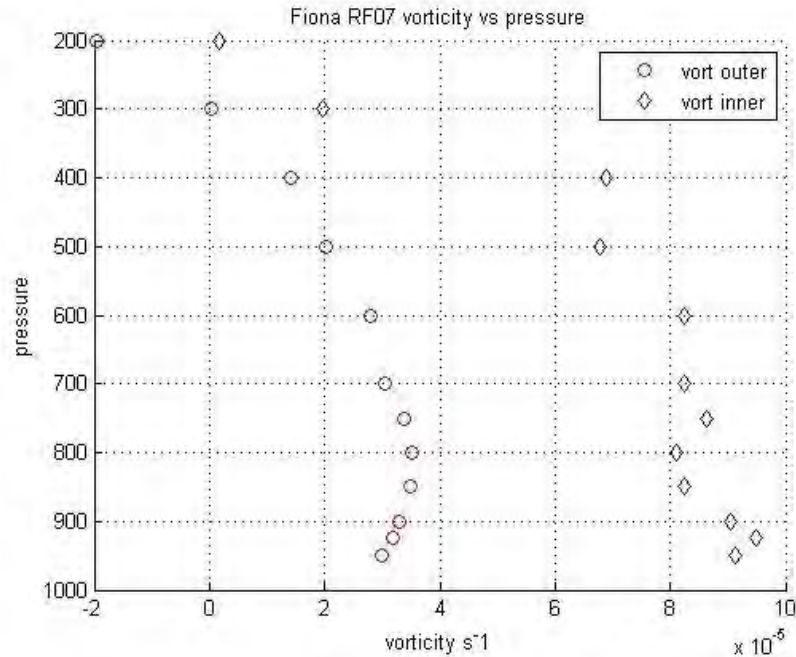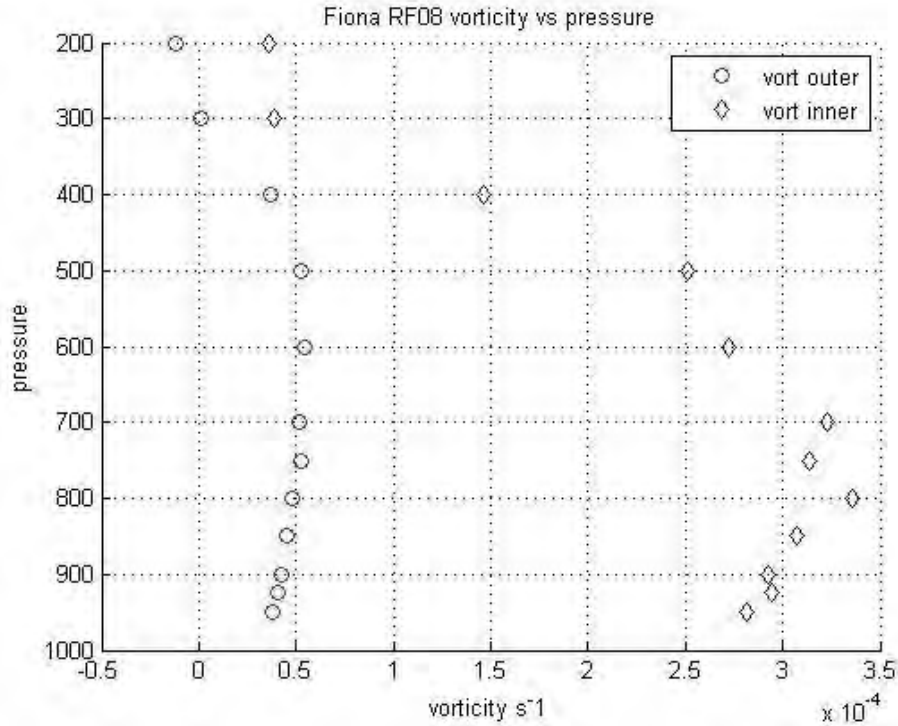
Figure 44.   Vertical profile of area-averaged vorticity for Research Flight 08 (PGI36) for the paths shown in Figure 43. Vorticity plotted in units of $10^{-4} s^{-1}$. The inner circulation path is depicted by blue diamonds and the outer circulation path is depicted by red circles. Image derived from NSF GV dropsondes.

Figure 46 indicates that the area-averaged vertical shear is larger for PGI36 than PGI30 or PGI27. However, when additionally taking into account Figure 45, the reader will see that the wind values in Fiona are larger than in the previous two disturbances discussed in this thesis. The individual co-moving wind vectors from each dropsonde in the 925 mb and 500 mb levels are, on a whole, more aligned than in the previous two disturbances. The larger area-averaged vertical shear is due to the magnitude of the winds and not the direction. Figure 45 nicely illustrates just how well vertically aligned PGI36 was from the 925 mb level to the 500 mb level.

Using the tangential velocity vs pressure graphs found in Appendix B, the inner-circulation path area-averaged tangential velocities for RF06, RF07, and RF08 are 7.7 $m \cdot s^{-1}$, 6.5 $m \cdot s^{-1}$ and 11.3 $m \cdot s^{-1}$ for the 500 mb level, respectively,

and 10.4 $m \cdot s^{-1}$, 7.9 $m \cdot s^{-1}$, and 14.5 $m \cdot s^{-1}$ for the 700 mb level, respectively. The normalized area-averaged vertical shear for RF06, RF07, and RF08 are 0.77, 0.82, and 0.55 for the pouch area-averaged vertical shear and 1.8, 1.8, and 1.3 for the deep area-averaged vertical shear. These small normalized vertical shear values would be expected given the characteristics of the kinematic flow structure of PGI36 discussed previously in this section (Davis and Ahijevych 2012).
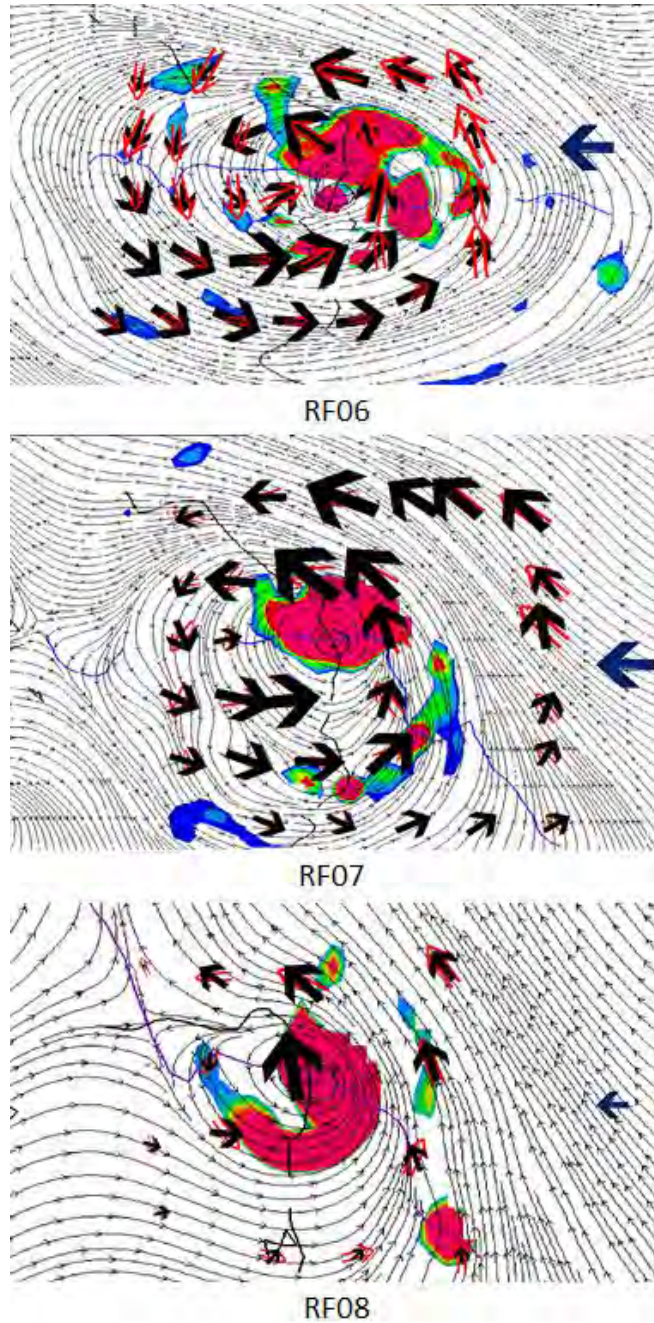
Figure 45. Vertical shear spatially represented by the 925 mb co-moving winds (black arrow), 500 mb co-moving winds (red arrow) from NSF GV dropsondes, and 700 mb co-moving streamline background for RF06, RF07, and RF08. All vectors are scaled to the same magnitude. The blue vector represents $10\,m \cdot s^{-1}$ winds (co-moving streamline images after Montgomery 2014a).
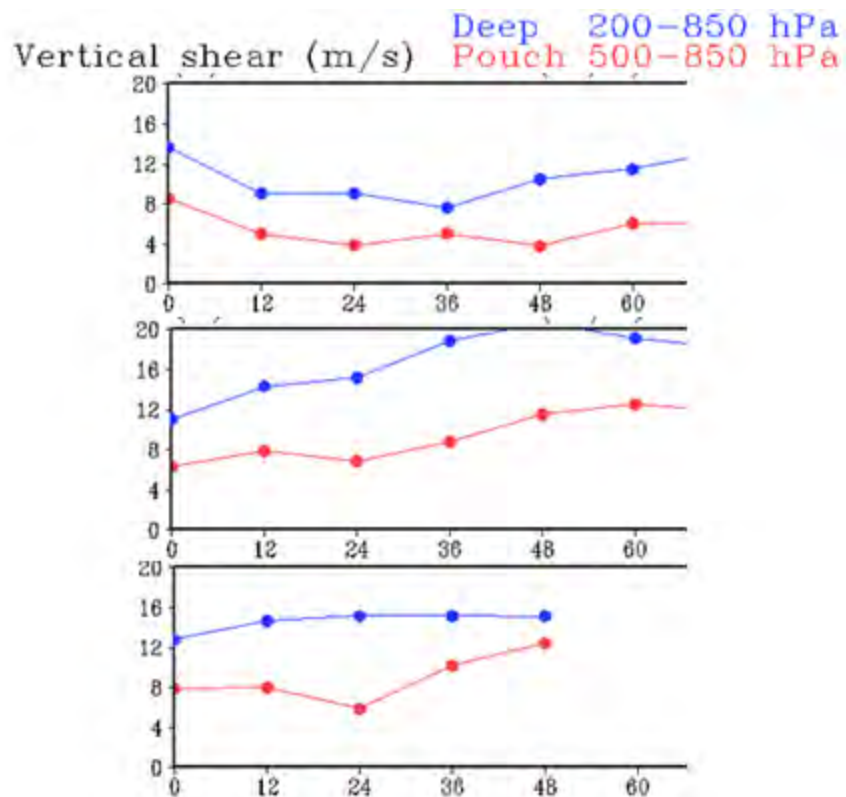
Figure 46.   Vertical shear averaged over the area of the pouch for RF06 (top), RF07 (middle), and RF08 (bottom). Values come from ECMWF. The valid forecast times are 2010083012, 2010083112 and 2010090100 from top to bottom, respectively (from Montgomery 2014a).

Figure 47 shows mixed profiles indicating moist and dry profiles throughout RF06. Additionally, the higher velocity winds will create a greater moister flux from the ocean, which should act to moisten the air as it is advected to the sweet spot.
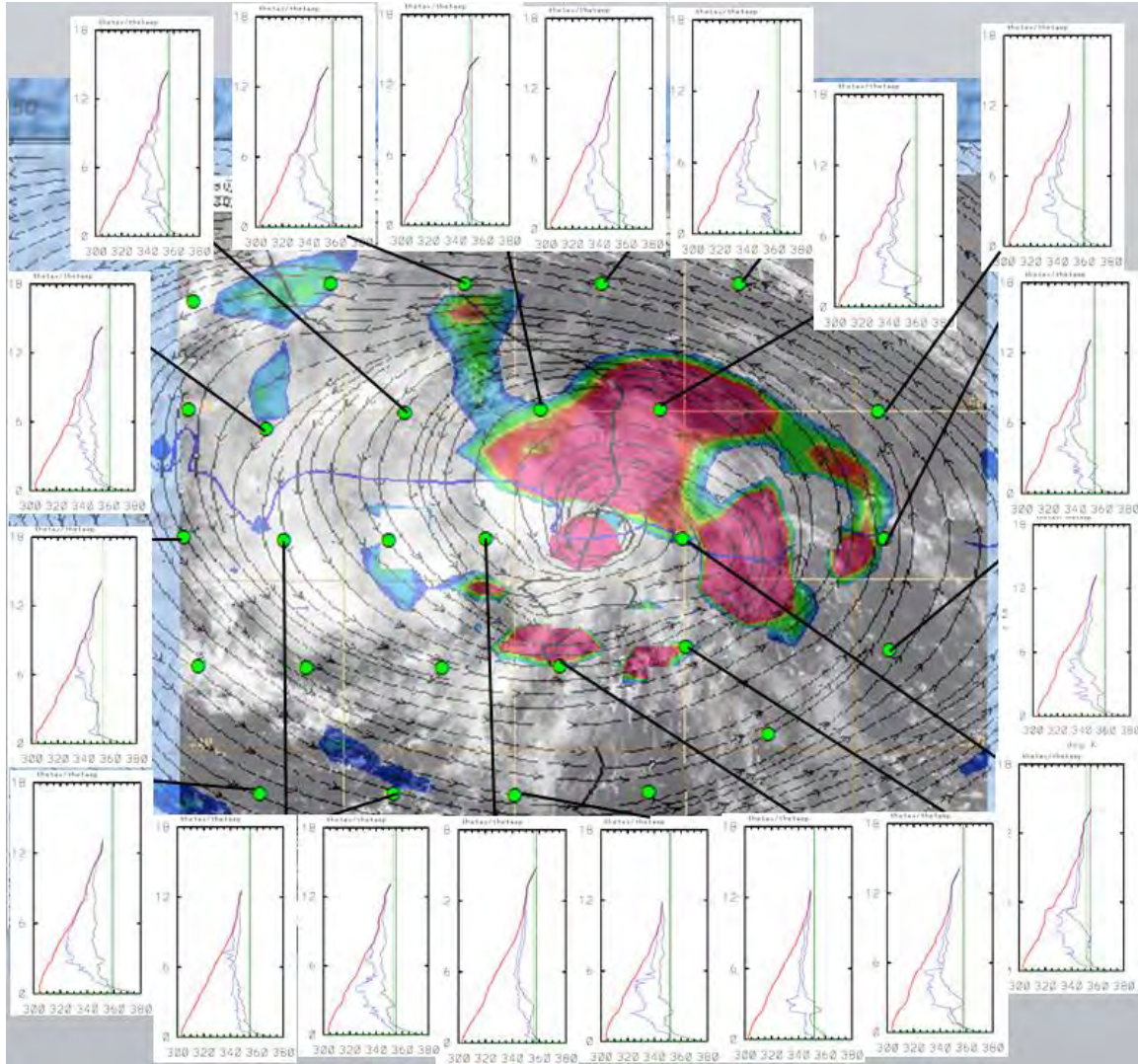
Figure 47.   Selected dropsonde profiles for RF06 corresponding with
dropsonde posits overlaid on the ECMWF 700 mb streamline
product and visible satellite image. Profiles derived from NSF
GV dropsondes (original satellite image from Naval Research
Laboratory-Monterey at
http://www.nrlmry.navy.mil/TC/tc10/ATL; co-moving streamline
images after Montgomery 2014a).

Figure 48 shows the difference between the smallest and largest value of

the averaged θ_e vertical profiles. The maximum difference ($\Delta \theta_e$) is 20.0 K, 22.0

K, and 21.3 K from the surface to 4.3 km, 4.6 km, and 3.7 km for RF06, RF07,

and RF83, respectively. The difference in the averaged θ_e could be the result of

mean surface θ_e increasing as Fiona intensified due primarily to increased winds at the surface and the increased flux of moisture that would accompany the increased winds. This would imply that the relatively large difference between the maximum and minimum averaged θ_e is the result of a surface wind increase rather than a drying effect in the vertical column (Smith and Montgomery 2012). Table 7 displays the relevant values for $\Delta\theta_e$.
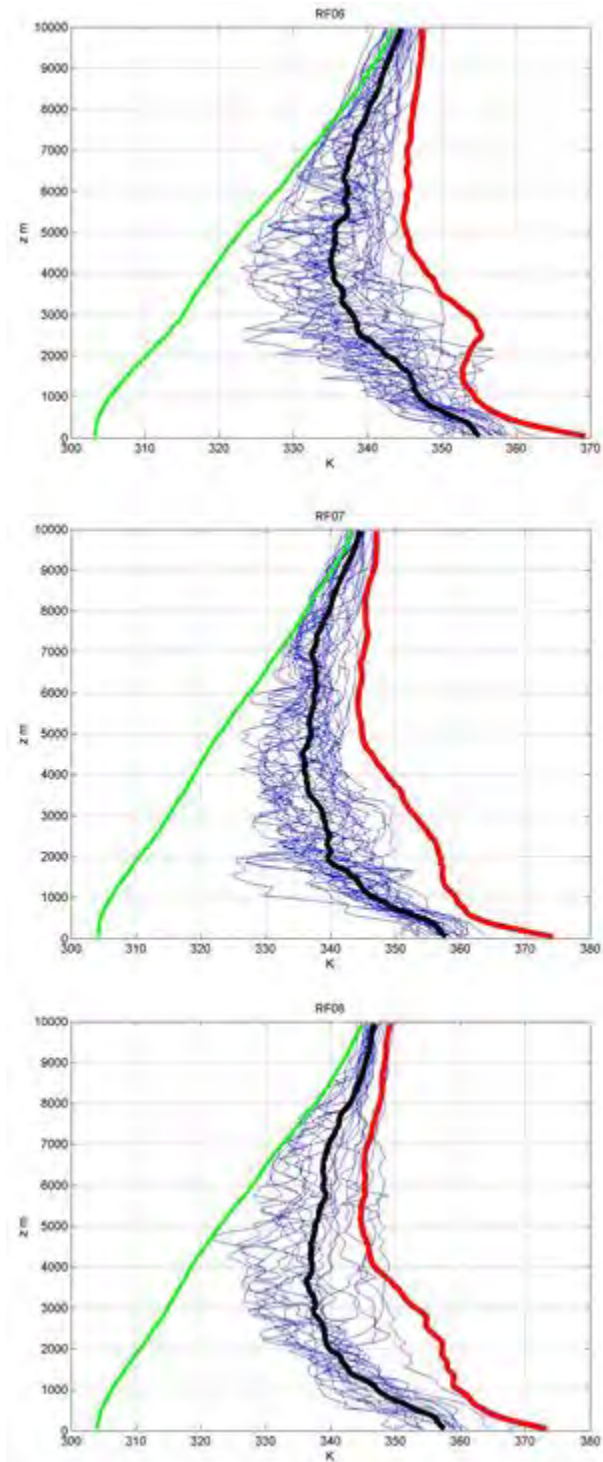
Figure 48.   Vertical profiles of the soundings displaying the values of θ_e, θ_{es}, and θ_v. Refer to Figure 23 for further explanation of graphic. Images derived from NSF GV dropsondes.

RF	min θ_e	min Z	max θ_e	max Z	$\Delta\theta_e$	ΔZ
6	335.1	4250	355	50	20	4200
7	335.7	4550	357.7	50	22	4500
8	336.2	3650	357.5	50	21.3	3600

Table 7.   Display of $\Delta\theta_e$ values for PGI36. Refer to Table 3 for further explanation of values. Table derived from NSF GV dropsondes.

THIS PAGE INTENTIONALLY LEFT BLANK

IV. CONCLUSIONS

A. SPECIFIC CONCLUSIONS RELATING TO TWO HYPOTHESES OF THE MARSUPIAL PARADIGM

Two of the three hypotheses (**H1** and **H2**) put forward by Dunkerton *et al.* (2009) are supported to some extent by my analysis of PGI27 and PGI30.

For the case of PGI27, the favorable kinematic flow characteristics from 17 August to 18 August were:

1. The OW parameter increased by a factor of four close to the sweet spot.

2. The area-averaged vorticity increased above the 900 mb level.

3. The normalized area-averaged pouch vertical shear decreased.

4. The disturbance became vertically aligned.

5. Co-moving streamlines become more closed at the 925 mb level.

The unfavorable kinematic flow characteristics were:

1. The normalized area-averaged deep vertical shear increased.

2. Streamlines become less closed at the 700 mb level.

3. The area averaged vorticity decreased below the 900 mb level.

Assuming the favorable kinematic flow characteristics outweigh the unfavorable flow characteristics, the marsupial paradigm would predict a gradual moistening of the pouch. Such a moistening is reflected to some extent in the decline of the area-averaged $\Delta\theta_e$. However, $\Delta\theta_e$ as a metric on its own comes with several sources of uncertainty:

1. The area-averaged surface θ_e decreases from 17 August to 18 August.

2. The vertical profile of the difference in area-averaged θ_e between the two days indicates alternating layers of weak moistening and drying throughout the column, yielding inconclusive results.

3. Additionally, a more comprehensive analysis needs to be carried out on the profile referenced in point 2 in order to isolate the θ_e signal from the noise.

For the case of PGI30, I found exclusively unfavorable characteristics for development from 21 August to 23 August. These unfavorable characteristics were:

1. The OW value became insignificant throughout the entire pouch.

2. The already shallow area-averaged cyclonic vorticity decreased in height.

3. The system no longer had any protective kinematic boundary structure.

The thermodynamic characteristics also became unfavorable for development as observed by the increase of the area-averaged $\Delta\theta_e$

These unfavorable kinematic and thermodynamic characteristics are consistent with **H1** and **H2** (Dunkerton et al. 2009).

B.   GENERAL CONCLUSIONS

Consistent with the findings of Smith and Montgomery (2012), moderately strong CAPE is observed in all of the developing and non-developing disturbances studied in this thesis. It would appear that the presence of moderately strong CAPE (1000-2000 J/kg) supports convective instability, creating favorable conditions for deep convection and some organization of that convection. The CAPE can be preferentially consumed near the sweet spot to support some convection organization. However, the presence of CAPE is simply

one of many characteristics a developing disturbance would require (Smith and Montgomery 2012).

For development, a favorable kinematic flow structure has to be present in conjunction with favorable thermodynamic parameters. The favorable kinematic flow characteristics include a recirculating flow, a vertically aligned structure, low horizontal strain, and low vertical wind shear. Without the presence of adequate moisture and convective activity, a favorable kinematic flow structure would not sustain itself in the presence of surface friction because the pouch would lack the vortex tube stretching and lower troposphere inflow that aggregated deep convection provides (Dunkerton *et al*. 2009; Smith and Montgomery 2012).

THIS PAGE INTENTIONALLY LEFT BLANK

APPENDIX A. CO-MOVING WIND OBSERVATIONS COMPARED TO STREAMLINE PRODUCTS

Appendix A shows graphics of model output for the 700 mb level and 925 mb level co-moving streamlines. Overlaid on the streamlines are the dropsonde co-moving wind vectors from the NSF GV dropsondes for the pressure level corresponding with the co-streamlines. This appendix exists to give the reader confidence that the model output co-moving streamlines are in agreement with the dropsonde data collected during the research missions.

A.   PGI27

Figure 49.   RF02 700 mb (top) and 925 mb (bottom) co-moving NSF GV dropsonde winds overlaid on ECMWF co-moving streamlines valid 2010081712 (0 hour tau) (after Montgomery 2014a).
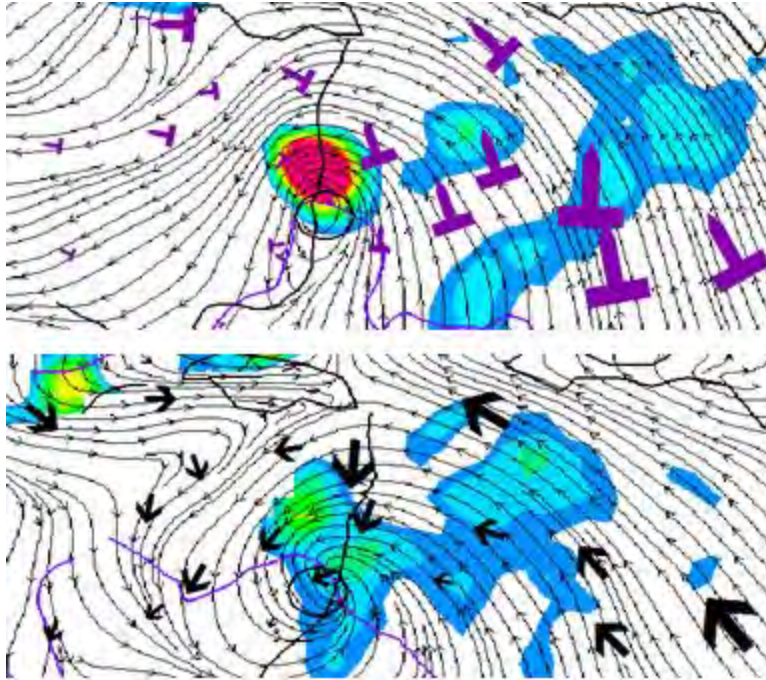
Figure 50. RF03 700 mb (top) and 925 mb (bottom) co-moving NSF GV
dropsonde winds overlaid on ECMWF co-moving streamlines
valid 2010081800 (12 hour tau) (after Montgomery 2014a).

B.   PGI30
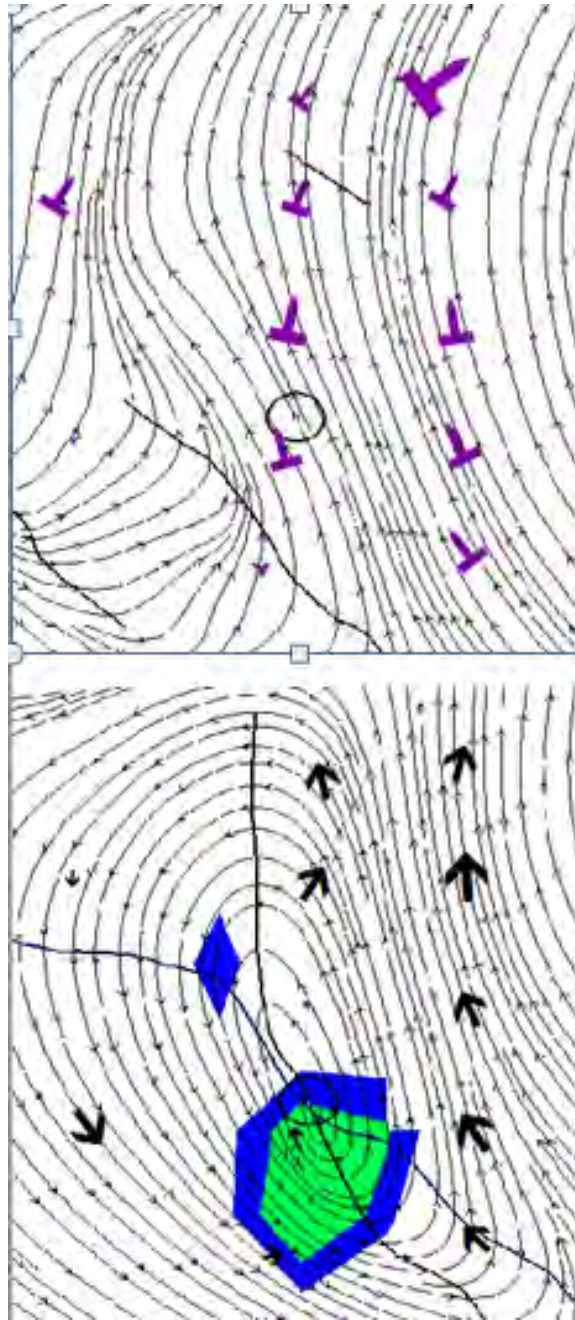
Figure 51.   RF04 700 mb (top) and 925 mb (bottom) co-moving NSF GV
dropsonde winds overlaid on GFS co-moving streamlines valid
2010082100 (12 hour tau) (after Montgomery 2014a).
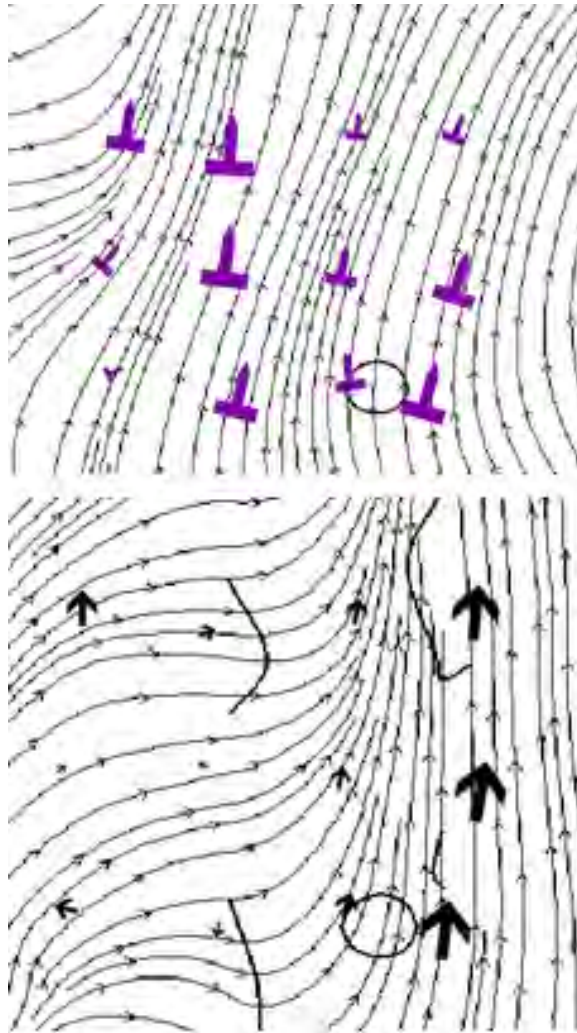
Figure 52.   RF05 700 mb (top) and 925 mb (bottom) co-moving NSF GV dropsonde winds overlaid on GFS co-moving streamlines valid 2010082212 (24 hour tau) (after Montgomery 2014a).

C.   PGI36
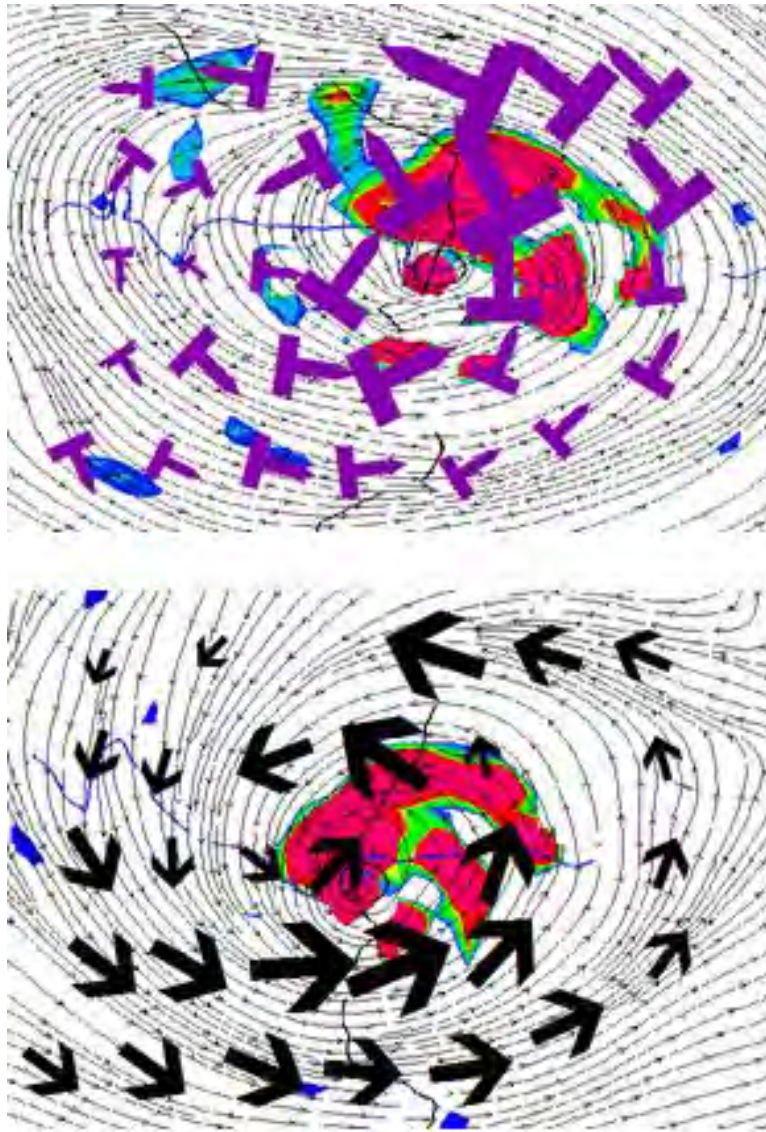
Figure 53.   RF06 700 mb (top) and 925 mb (bottom) co-moving NSF GV
dropsonde winds overlaid on ECMWF co-moving streamlines
valid 2010083012 (0 hour tau) (after Montgomery 2014a).
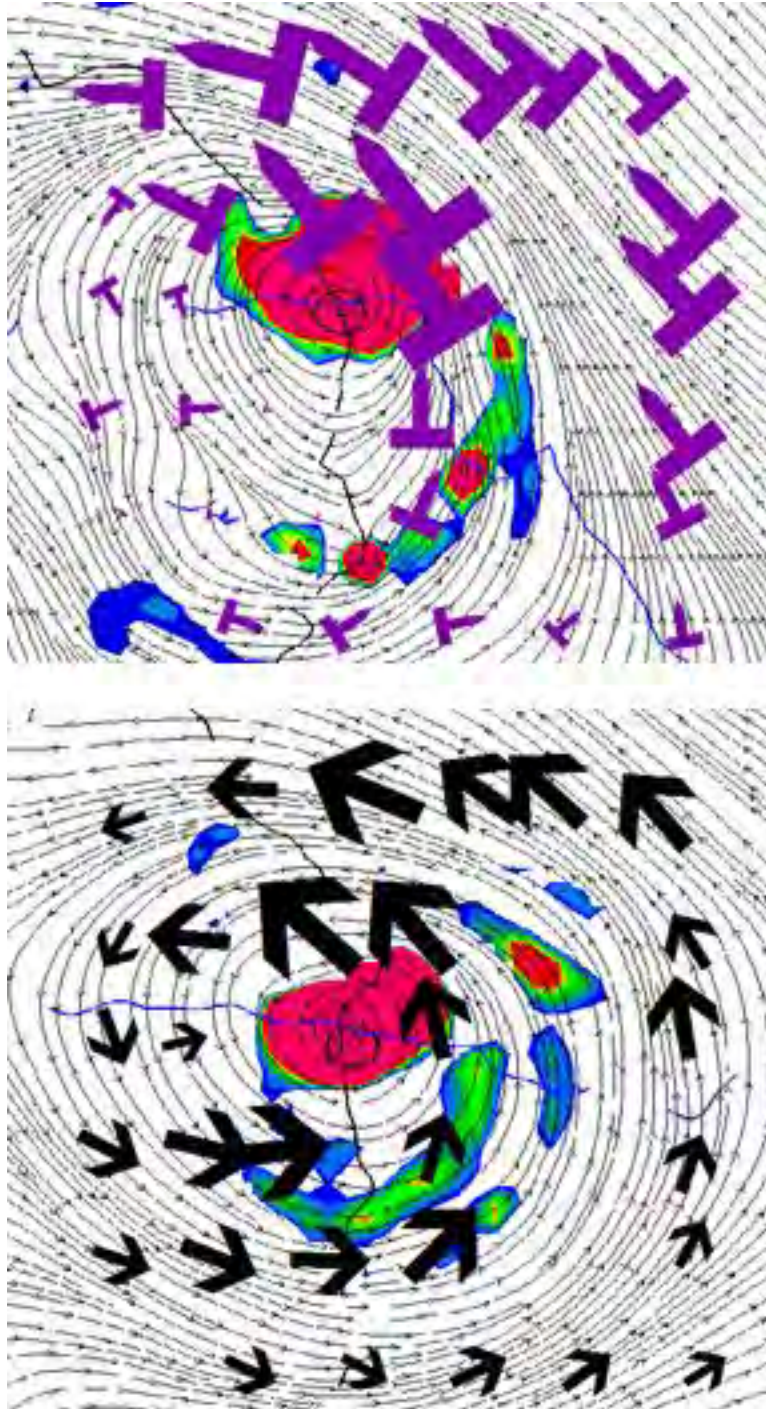
Figure 54.   RF07 700 mb (top) and 925 mb (bottom) co-moving NSF GV dropsonde winds overlaid on ECMWF co-moving streamlines valid 2010083112 (0 hour tau) (after Montgomery 2014a).
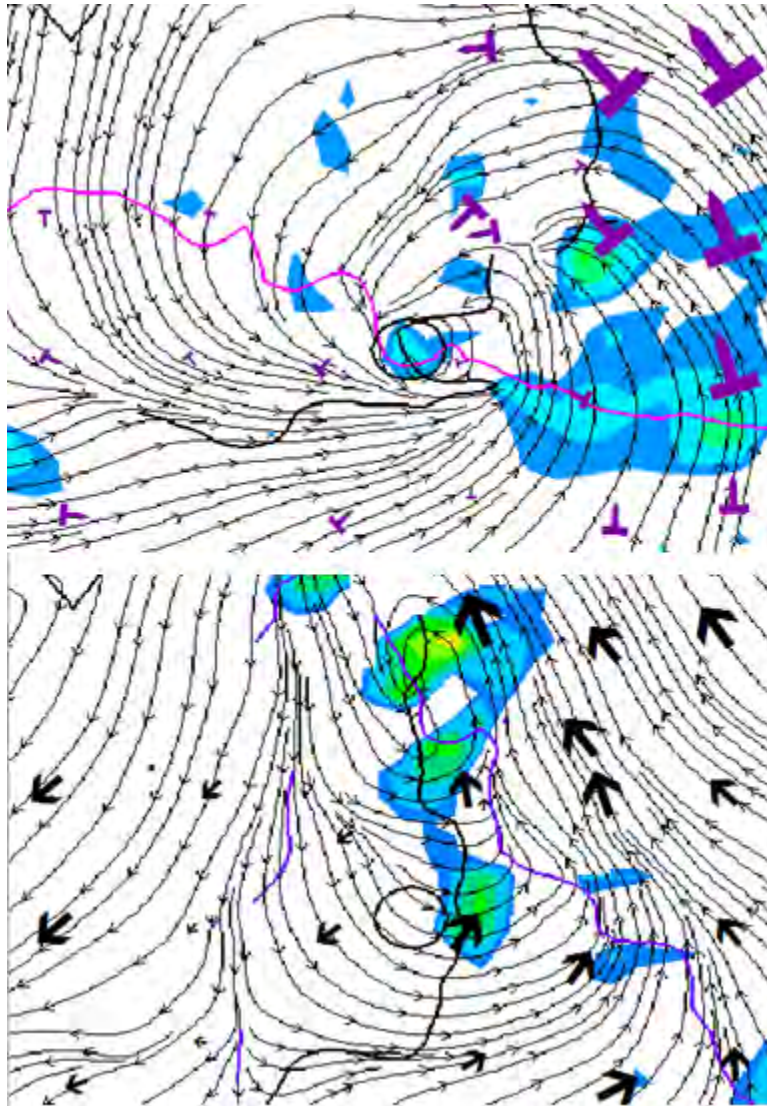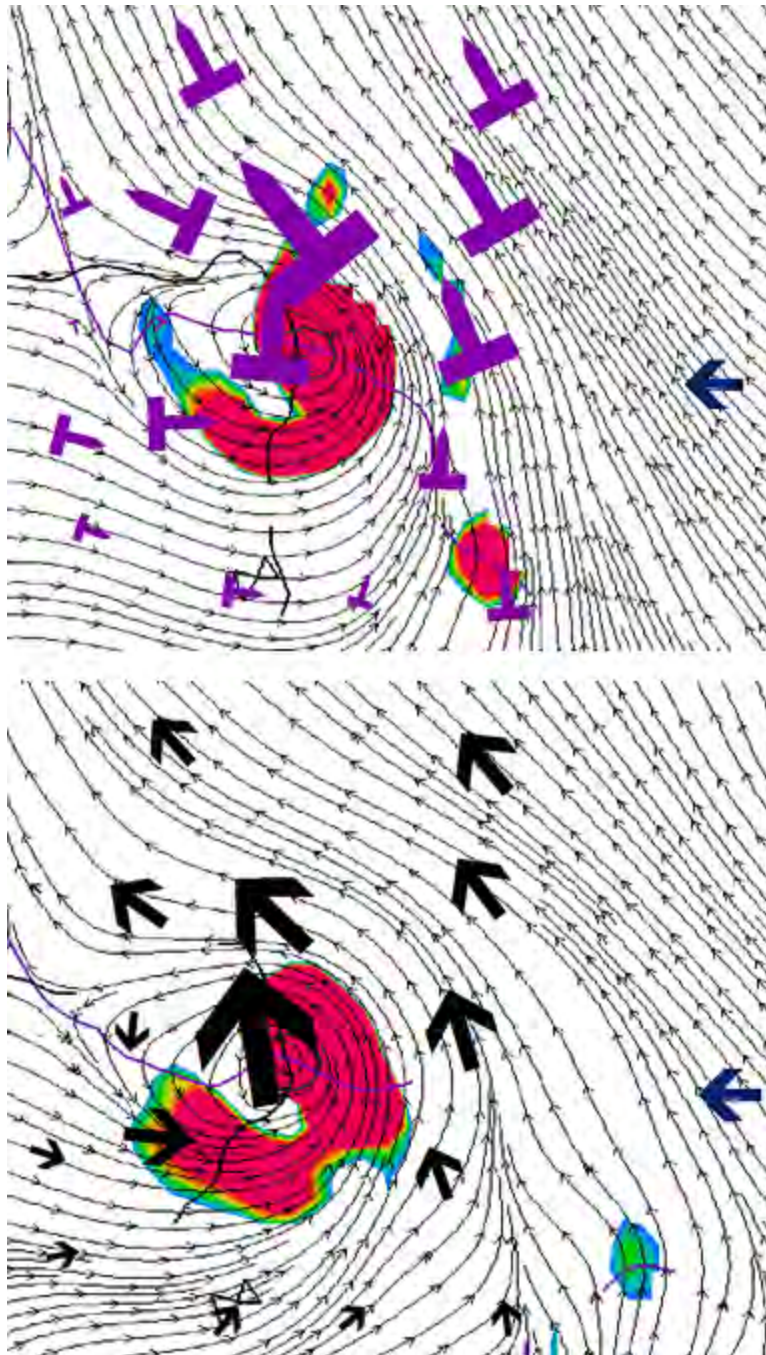
Figure 55.   RF08 700 mb (top) and 925 mb (bottom) co-moving NSF GV dropsonde winds overlaid on ECMWF co-moving streamlines valid 2010090112 (0 hour tau) (after Montgomery 2014a).

APPENDIX B. TANGENTIAL VELOCITY

Appendix B shows all of the vertical profiles for the area-averaged tangential velocity for the circulation paths chosen for all of the research flights.

A.   PGI27

Figure 56.   Vertical profile of area-averaged tangential velocity for Research Flight 02 (in PGI27) for the paths shown in Figure 14. Velocity plotted in units of $m \cdot s^{-1}$. The inner circulation path is shown using red circle, middle circulation path is shown using the diamond, and outer circulation path is shown using plus symbol. Image derived from NSF GV dropsondes.

Figure 57.   Vertical profile of area-averaged tangential velocity for Research Flight 03 (in PGI27) for the paths shown in Figure 16. Velocity plotted in units of $m \cdot s^{-1}$. The inner circulation path is shown with blue diamonds and the outer circulation path is shown with red circles. Image derived from NSF GV dropsondes.

B.   PGI30

Figure 58.   Vertical profile of area-averaged tangential velocity for
Research Flight 04 (in PGI30) for the path shown in Figure 28.
Velocity plotted in units of $m \cdot s^{-1}$. Image derived from NSF GV
dropsondes.

Figure 59.   Vertical profile of area-averaged tangential velocity for
Research Flight 05 (in PGI30) for the path shown in Figure 30.
Velocity plotted in units of $m \cdot s^{-1}$. Image derived from NSF GV
dropsondes.

Figure 60.   Vertical profile of area-averaged tangential velocity for Research Flight 06 (in PGI36) for the paths shown in Figure 38. Velocity plotted in units of $m \cdot s^{-1}$. The inner and outer circulation paths in Figure 39 are plotted using blue diamonds and red circles, respectively. Image derived from NSF GV dropsondes.

Figure 61.   Vertical profile of area-averaged tangential velocity for Research Flight 07 (in PGI36) for the paths shown in Figure 41. Velocity plotted in units of $m \cdot s^{-1}$. The inner and outer circulation paths for RF07 are depicted as blue diamonds and red circles, respectively. Image derived from NSF GV dropsondes.

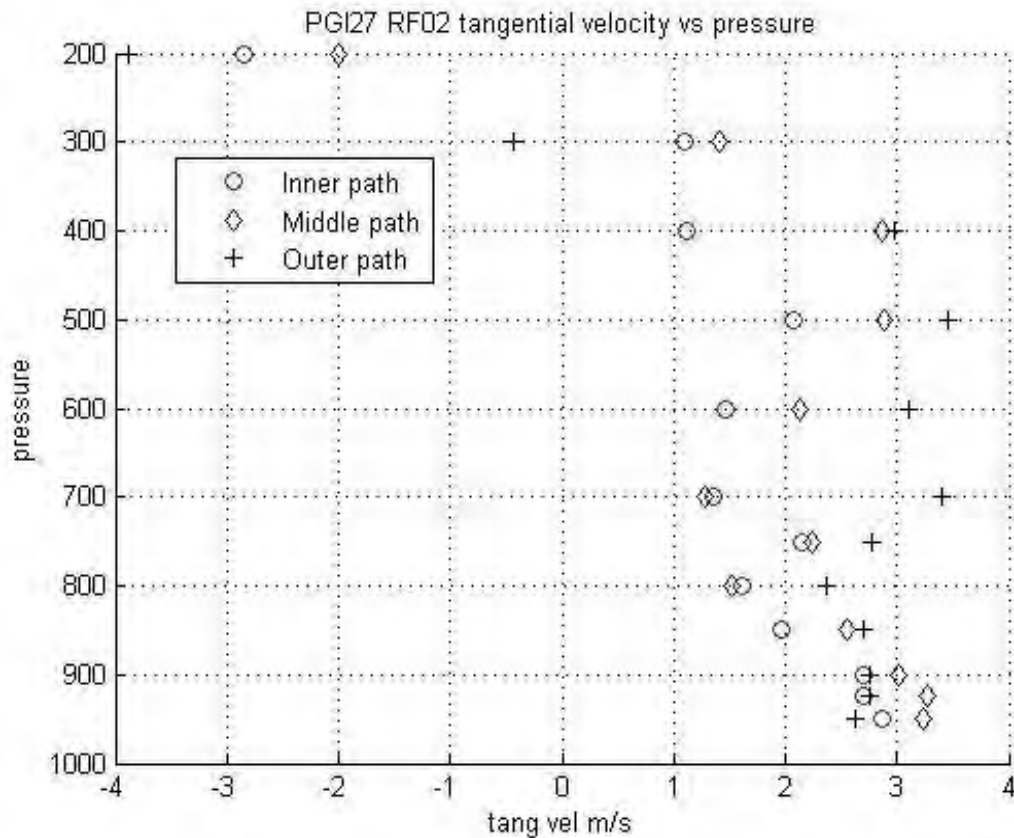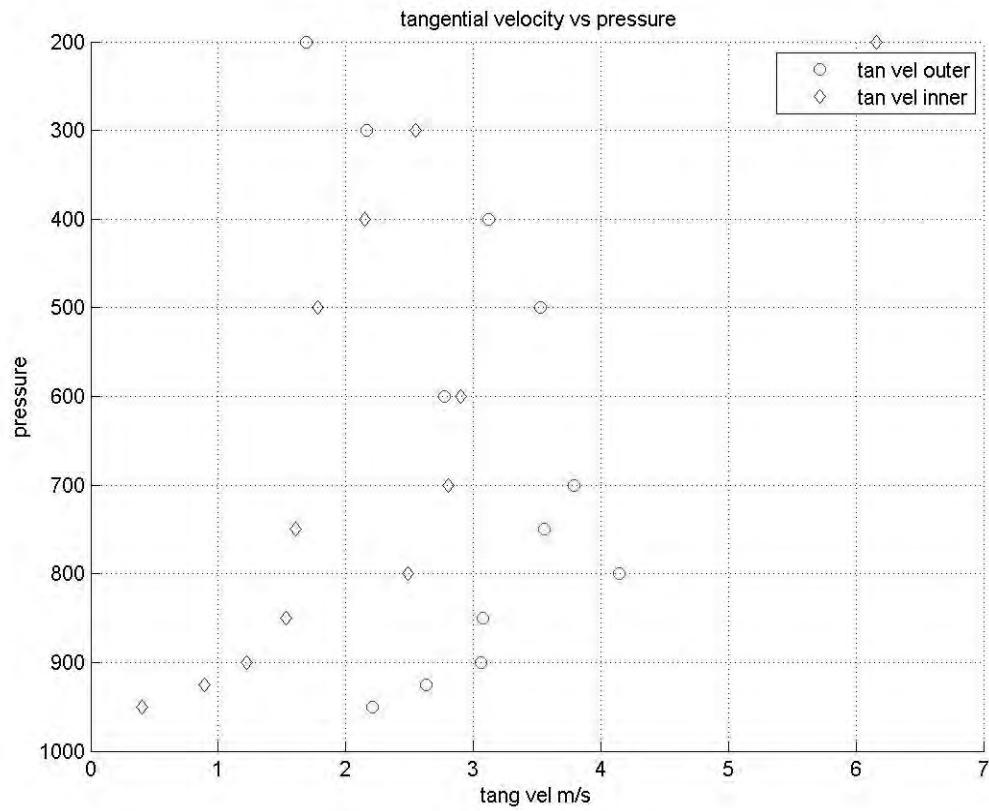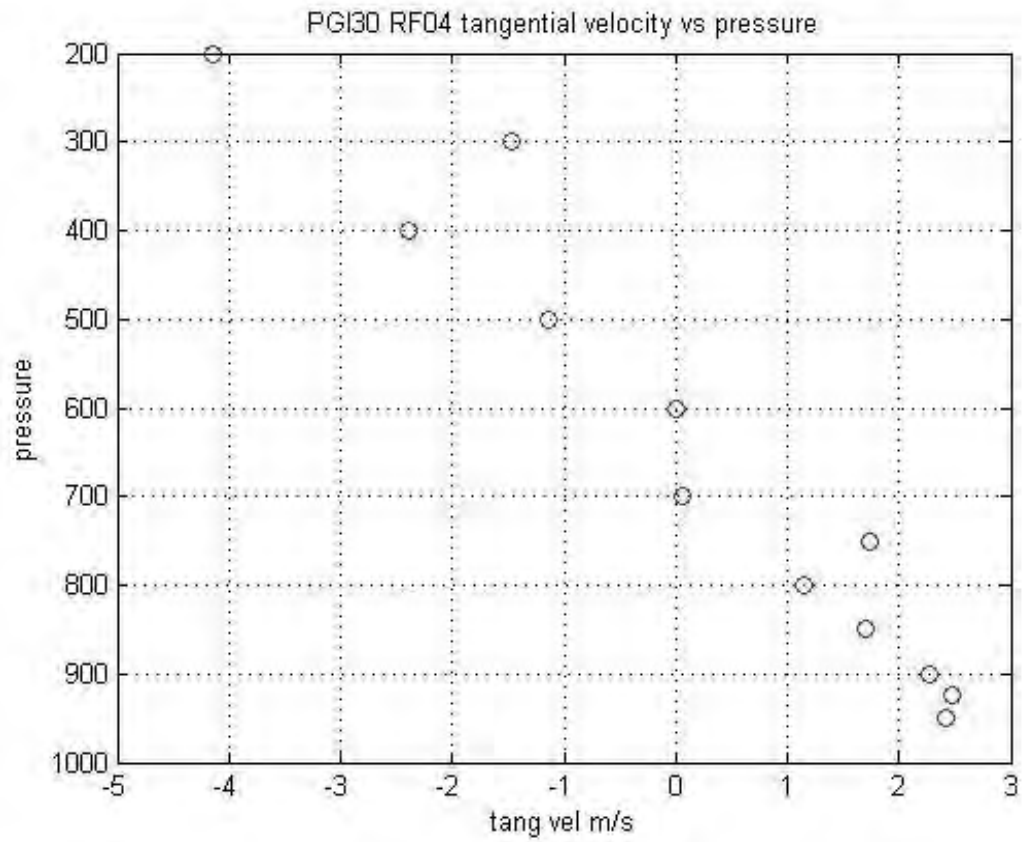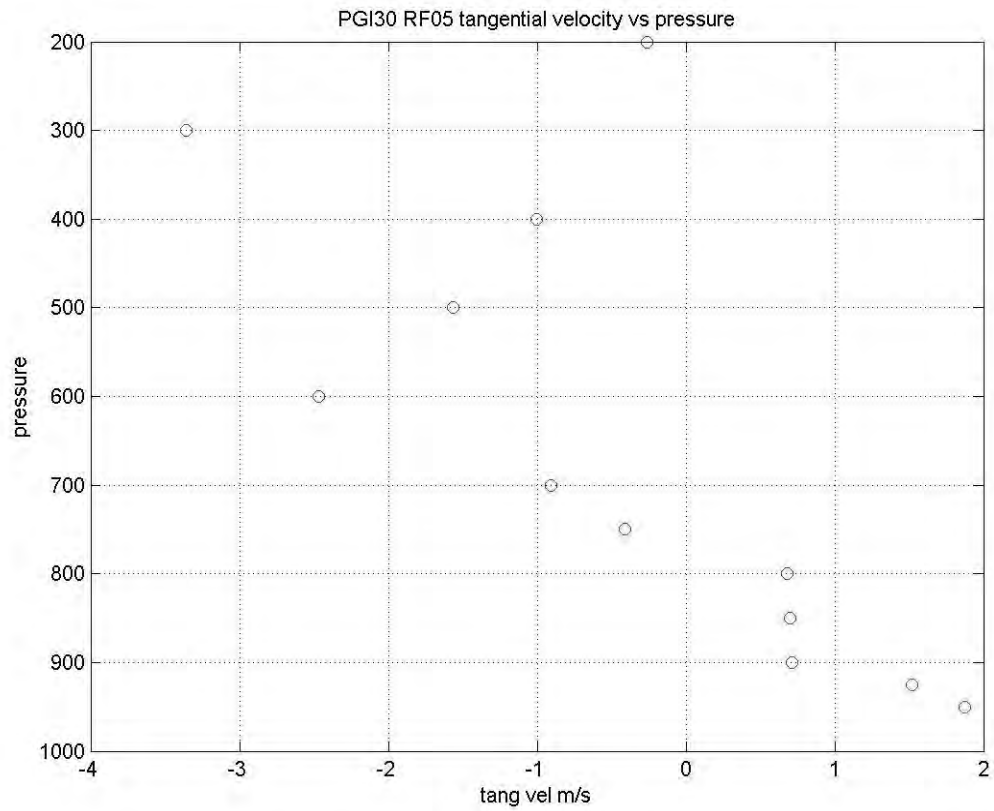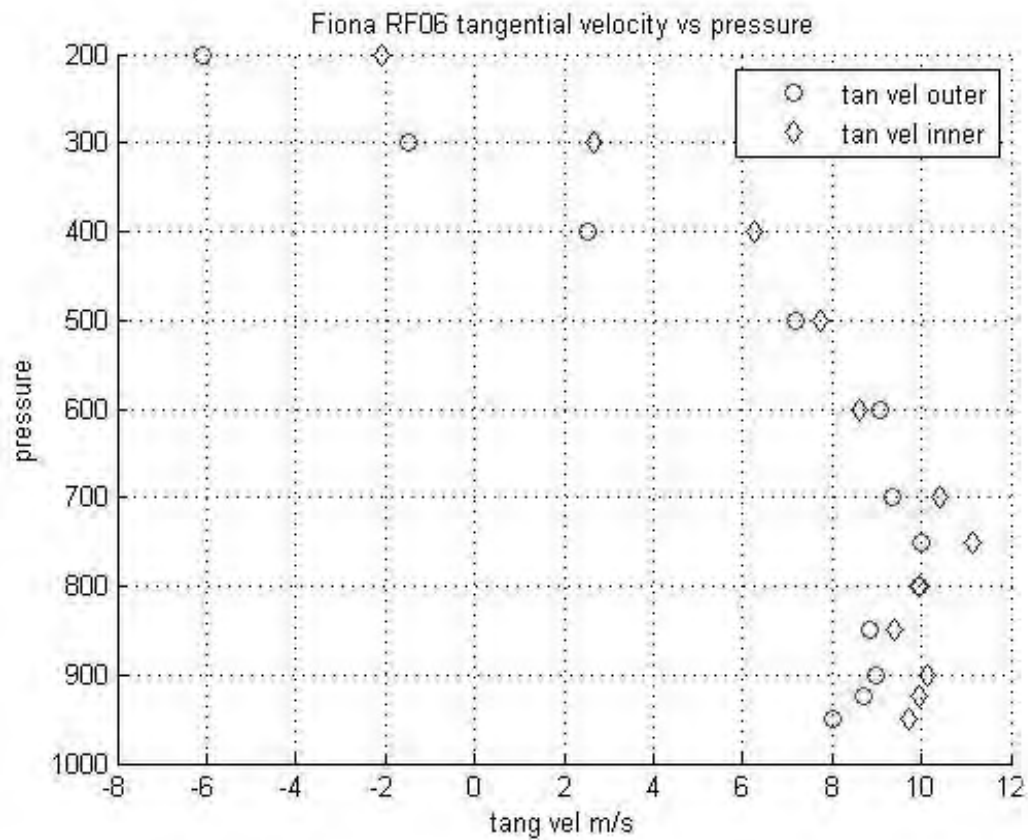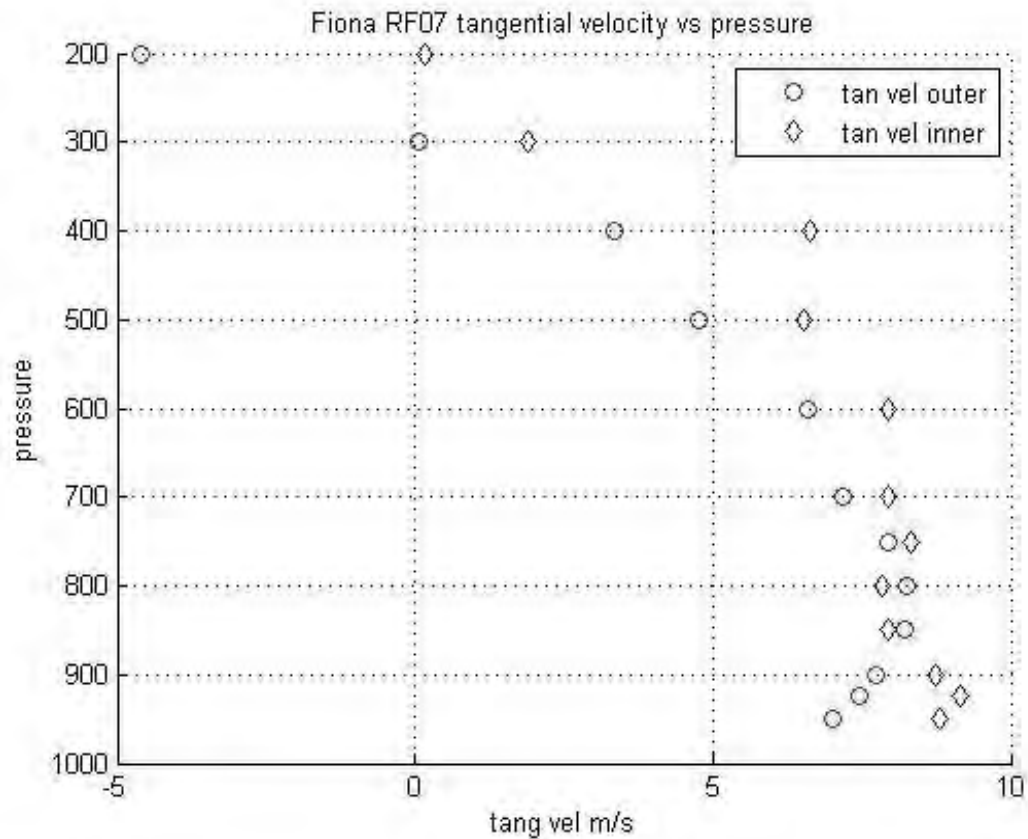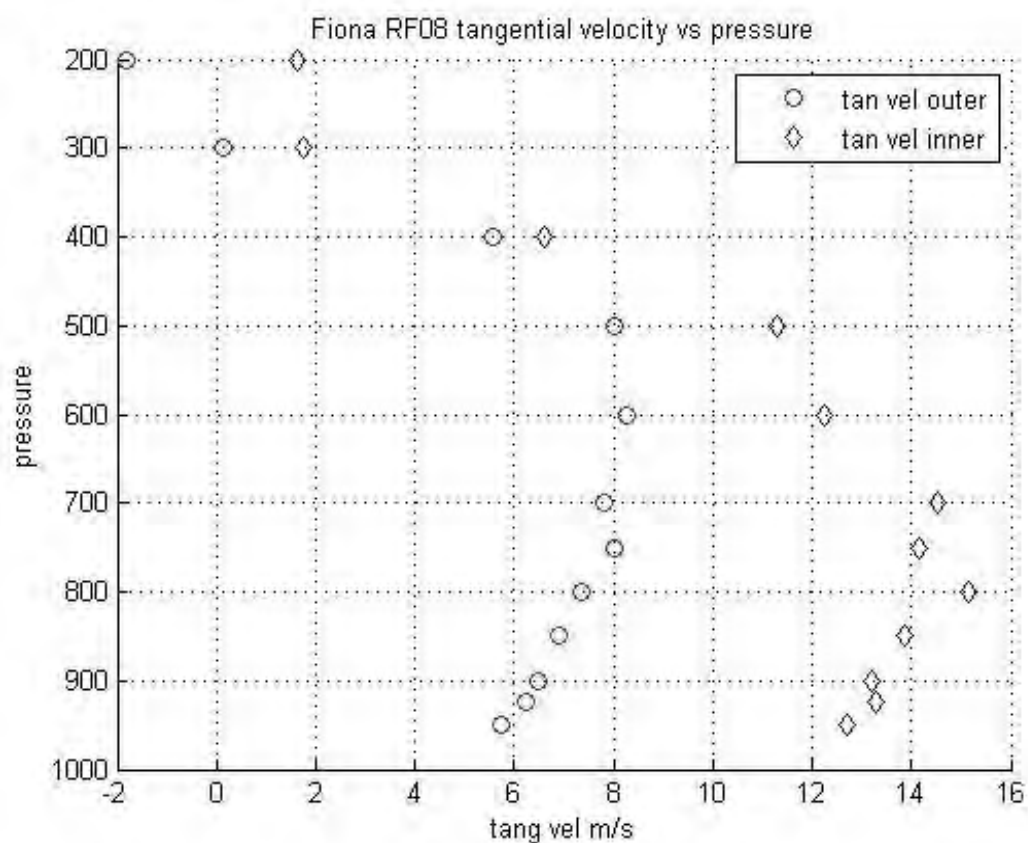Figure 62.   Vertical profile of area-averaged tangential velocity for Research Flight 08 (PGI36) for the paths shown in Figure 43. Velocity plotted in units of $m \cdot s^{-1}$. The inner circulation path is depicted by blue diamonds and the outer circulation path is depicted by red circles. Image derived from NSF GV dropsondes.

THIS PAGE INTENTIONALLY LEFT BLANK

APPENDIX C SUMMARY OF THE DATA RETRIEVAL AND PROCESSING FROM THE DROPSONDES

The dropsonde data used in this thesis is in an EOL format, which is an ascii text format containing a header and several columns of data. The relevant columns of data are time, latitude, longitude, pressure, u vector winds, v vector winds, magnitude of the winds, and direction of the winds. The data for each dropsonde was contained in its own text file. The data format is explained in detail in 'Pre-Depression investigation of cloud-systems in the Tropics (PREDICT) 2010 Quality Controlled Dropsonde Data Set' under the 'EOL file format' section found at http://data.eol.ucar.edu/datafile/nph-get/126.012/readme.PREDICT-2010.GV.dropsondes.pdf. In order to make use of the data, I created and executed several MATLAB codes. The purpose of this appendix is to summarize the four main MATLAB codes that pulled out the dropsonde wind data; calculated the values at various levels; geographically binned the CAPE and CIN values associated with each dropsonde calculated from a FORTRAN code already described in the methodology; and calculated and plotted θ_e, θ_{es}, θ_v profiles. These programs can be found on the Montgomery working group website. ArcGIS was the display tool used to geo-rectify and display satellite imagery, model output, and the output from the four previously mentioned MATLAB programs.

The first MATLAB program was written to extract the wind data at the desired pressure levels from each dropsonde and organize that data in an excel spreadsheet. The program was run for each research flight (RF), and a separate RF-specific excel spreadsheet was created. The newly created excel spreadsheet consisted of a column of object-ids, which correspond to a specific dropsonde released during the research flight. In this output spreadsheet, the numerical order of the object-ids descends in chronological order according to the time of the drop of each dropsonde. Each row of object-ids has the time, latitude, longitude, and wind data at all of the desired pressure levels. The

latitude and longitude of each object-id is a column average of the latitude and longitude for the corresponding dropsonde. The time is taken from the first few seconds of the drop for each dropsonde. The winds corresponding to each pressure level are an average of the recorded winds for plus and minus three mb of the analyzed pressure level.

The wind data are organized as follows. For each dropsonde, the winds for each pressure level are obtained by executing a find command along the pressure column of the dropsonde text file. The program then indexes that column, finds the winds corresponding to the applicable pressure index, and then vertically averages the corresponding winds. If there are no values of winds or pressures in the 6 mb pressure window for each analyzed pressure level, then blanks are inserted into the output excel spreadsheet. A common problem found while retrieving the wind data was that the dropsonde appeared to alternate between collecting pressure and wind data. This had the consequence of creating several rows of not-a-number (NAN) values for either pressure or winds. This would result in blank data entries in the output excel spreadsheet for that specific field. Since the MATLAB program assumes pressure and wind values in the same column, this requires the user to manually go through the dropsonde data, and enter the appropriate wind data. Approximately 5% of the collected wind data resulted from manual entry of wind data into the RF-specific excel spreadsheet. There were also some dropsondes that did not have wind data available, and these dropsondes had to be omitted from circulation calculations. The pressure levels for the applicable dropsondes that this occurred in are documented in the CAPE/CIN tables in the Results Chapter of this thesis.

The second MATLAB program I created uses the excel spreadsheet output from the first MATLAB program as an input, and is able to calculate circulation, as defined in the Methodology Chapter (Section C, Kinematic Analysis). This is done in several steps. ARCGIS is used to visually organize the dropsondes by inputting the excel spreadsheet into ARCMAP. Using co-moving streamlines, Okubo-Weiss values, and the assessed sweet spot, dropsonde

circulation paths were chosen as shown under the Methodology Chapter (Section C, Kinematic Analysis). The perimeter of the circulation was calculated directly from the MATLAB program. The area of the circulation was acquired from projecting the circulation onto ARCMAP. When comparing the perimeter from the MATLAB program to the perimeter from ARCMAP, a difference from one to five percent was noted. This is partially due to ARCMAP's projected coordinate system versus MATLAB's great circle calculation, and partly due to all of the circulation paths in ARCMAP having to be manually inserted using a polygon shape tool. The output of this MATLAB program was circulation, tangential velocity, and vorticity at the various levels analyzed throughout this thesis. Tangential velocity and vorticity were the two values utilized in this thesis as these values are normalized in the sense they are circulation divided by the perimeter and area of the circulation, respectively.

The third MATLAB program is able to spatially bin averaged CAPE and CIN values as a function of distance away from the sweet spot for each research flight. This program also uses the excel spreadsheet output from the first MATLAB program. However, the CAPE and CIN values for each dropsonde have already been calculated by a previously designed FORTRAN code. These values are manually entered as the last two columns for each RF specific excel spreadsheet. The third MATLAB code requires a user input of the latitude and longitude of the center of the sweet spot as well as the latitude and longitude of a point where the user desires the radius of the spatial binning to end. The MATLAB program will then take this input, and create four concentric circles around the sweet spot. Each concentric circle is a distance of 25% away from the adjacent concentric circle. The program will then use a 'find and index command' to organize the dropsonde locations belonging to a specific bin in the inner-most concentric circle or between two concentric circles. The CAPE and CIN values of the dropsondes in each bin are averaged arithmetically and then displayed as a bar graph for each bin.

111

The fourth MATLAB program plots θ_e, θ_{es}, and θ_v. This MATLAB program extracts parameters necessary to calculate θ_e, θ_{es}, and θ_v that correspond with height every fifty meters in a similar manner as with the first MATLAB program that extracts this data from the dropsonde text files. Once this data is extracted, θ_e, θ_{es}, and θ_v are calculated as described in the Methodology Chapter under part B, Thermodynamic Analysis. The values of θ_e for each dropsonde, area-averaged θ_e, area-averaged θ_{es}, and area-averaged θ_v are then plotted on one profile for each research mission.

LIST OF REFERENCES

Bell, M., cited 2010a: PREDICT mission scientist summary RF03. [Available online at http://catalog.eol.ucar.edu/cgi-bin/predict/htmlwrap?file_url=/predict/report/mission_scientist/20100818/report.mission_scientist.201008181020.summary.html.]

Bell, M., cited 2010b: PREDICT mission scientist summary RF05. [Available online at http://catalog.eol.ucar.edu/cgi-bin/predict/htmlwrap?file_url=/predict/report/mission_scientist/20100823/report.mission_scientist.201008231000.summary.html.]

Bell, M., cited 2010c: PREDICT mission scientist summary RF06. [Available online at http://catalog.eol.ucar.edu/cgi-bin/predict/htmlwrap?file_url=/predict/report/mission_scientist/20100830/report.mission_scientist.201008300907.summary.html.]

Bell, M., cited 2010d: PREDICT mission scientist summary RF07. [Available online at http://catalog.eol.ucar.edu/cgi-bin/predict/htmlwrap?file_url=/predict/report/mission_scientist/20100831/report.mission_scientist.201008311000.summary.html.]

Bell, M., cited 2010e: PREDICT mission scientist summary RF08. [Available online at http://catalog.eol.ucar.edu/cgi-bin/predict/htmlwrap?file_url=/predict/report/mission_scientist/20100901/report.mission_scientist.201009011200.summary.html.]

Berg, R., 2010: Tropical cyclone report Tropical Storm Fiona (ALS082010) 30 August– 3 September 2010. National Hurricane Center, 13 pp.

Boothe, M. A., and M. T. Montgomery, 2012: Basic kinematics in developing and non-developing tropical disturbances based upon dropwindsonde data during PREDICT. *30th Conference on Hurricanes and Tropical Meteorology,* Ponte Vedra Beach, FL, Amer. Meteor. Soc.. [Available online at https://ams.confex.com/ams/30Hurricane/webprogram/Paper205563.html]

Davis, C. A., and D. A. Ahijevych, 2012: Mesoscale structural evolution of three tropical weather systems observed during PREDICT. *J. Atmos. Sci.*, **69**, 1284–1305.

Davis, C., cited 2010a: PREDICT science director summary research. [Available online at http://catalog.eol.ucar.edu/cgi-bin/predict/htmlwrap?file_url=/predict/report/science_director/20100817/report.science_director.201008171840.summary.html.]

Davis, C., cited 2010b: PREDICT science director summary research. [Available online at http://catalog.eol.ucar.edu/cgi-bin/predict/htmlwrap?file_url=/predict/report/science_director/20100818/report.science_director.201008182134.summary.html]

Dunkerton, T. J., M. T. Montgomery, and Z. Wang, 2009: Tropical cyclogenesis in a tropical wave critical layer: easterly waves. *Atmos. Chem. Phys*, **9**, 5587–5646.

Emanuel, K. A., J. D. Neelin, and C. S. Bretherton, 1994: On large-scale circulations. *Q. J. R. Meteorol. Soc.*, **120**, 1111–1143.

Holton, J. R., 2004: *An Introduction to Dynamic Meteorology*. 4th ed. Academic Press, 535 pp.

Holton, J. R., 1979: *An Introduction to Dynamic Meteorology*. 2nd ed. Academic Press, 391 pp.

James RP, Markowski PM., 2009. A numerical investigation of the effects of dry air aloft on deep convection. *Mon. Weather Rev*. **137**: 140–161.

Kilroy, G., and R. K Smith, 2012: A numerical study of rotating convection during tropical cyclogenesis. *Quarterly Journal of the Royal Meteorological Society*, 15.

Komaromi, W. A., 2013: An investigation of composite dropsonde profiles for developing and non-developing tropical waves during the 2010 PREDICT field campaign. *American Meteorology Society*, **70**, 542–558.

McWilliams, J., 1984: The emergence of isolated coherent vortices in turbulent flow. *J. Fluid Mech*., **146**, 21–43.

Montgomery, M. T., 2010: PREDICT science director summary research. [Available online at http://catalog.eol.ucar.edu/cgi-bin/predict/htmlwrap?file_url=/predict/report/science_director/20100821/report.science_director.201008210900.summary.html.]

Montgomery, M. T., and Coauthors, 2012: The pre-depression investigation of cloud-systems in the tropics (PREDICT) experiment. *Bull American Meteorological Society*, **93**, 153–172.

Montgomery, M. T., cited 2014a: Naval postgraduate School Department of Meteorology Montgomery Research Group archived 2010 wave-pouches. [Available online at http://www.met.nps.edu/~mtmontgo/archive2010.html.]

Montgomery, M. T., cited 2014b: Naval Postgraduate School Department of Meteorology Montgomery Research Group MR3252: Tropical Meteorology/Laboratory. [Available online at http://met.nps.edu/~mtmontgo/mr3252.html.]

Smith, R. K., 1979: The Physics and Parameterization of Moist Atmospheric Convection. Ed. Springer Netherlands, 498 pp.

Smith, R. K., and M. T. Montgomery, 2012: Observations of the convective environment in developing and non-developing tropical disturbances. *Quarterly Journal of the Royal Meteorological Society*, **138**: 1721–1739.

Raymond, D., 2010a: PREDICT mission scientist summary. RF02 of G-V. [Available online at http://catalog.eol.ucar.edu/cgi-bin/predict/htmlwrap?file_url=/predict/report/mission_scientist/20100817/report.mission_scientist.201008171019.summary.html.]

Raymond, D., 2010b: PREDICT mission scientist summary. RF04 Mission into PGI30. [Available online at http://catalog.eol.ucar.edu/cgi-bin/predict/htmlwrap?file_url=/predict/report/mission_scientist/20100821/report.mission_scientist.201008210900.summary.html.]

Rutherford, B. and M. T. Montgomery, 2012: A Lagrangian analysis of a developing and non-developing disturbance observed during the PREDICT experiment. *Atmospheric Chemistry and Physics*, **12**, 11355–11381.

Tang, B., and E. Emanuel, 2012: A ventilation index for tropical cyclones. *Bull American Meteorological Society, **93**, 1901–1912.*

Veness, C., 2002: Calculate distance, bearing and more between latitude/longitude points. [Available online at http://www.movable-type.co.uk/scripts/latlong.html.]

Weiss, J., 1991: The dynamics of enstrophy transfer in two-dimensional hydrodynamics. *Physica D*, **48**, 273–294.

Xu, K., and K.A. Emanuel, 1989: Is the tropical atmosphere conditionally unstable?. *Mon. Wea. Rev*., **117**, 1471–1479.

Young, Kate *et al*., 2010: Pre-depression investigation of cloud-systems in the tropics (PREDICT) 2010 quality controlled dropsonde data set. [Available online at http://data.eol.ucar.edu/datafile/nph-get/126.012/readme.PREDICT-2010.GV.dropsondes.pdf.]

THIS PAGE INTENTIONALLY LEFT BLANK

INITIAL DISTRIBUTION LIST

1.   Defense Technical Information Center
        Ft. Belvoir, Virginia

2.   Dudley Knox Library
        Naval Postgraduate School
        Monterey, California